POLITECNICO DI MILANO
SCUOLA INTERPOLITECNICA DI DOTTORATO
Doctoral Program in Structural, Earthquake and Geotechnical Engineering

XXV Ciclo - Final Dissertation

FREQUENCY AND TIME DOMAIN ANALYSIS ON FIBER REINFORCED POROVISCOELASTIC TISSUE: STUDY ON ARTICULAR CARTILAGE THROUGH NANOINDENTATION TESTS AT MICROMETRIC CHARACTERISTIC LENGTHS

MATTEO TAFFETANI

Tutor
Prof. Ing. Pasquale Vena

Co-ordinator of the Research Doctorate Course
Prof. Ing. Roberto Paolucci

28/02/2013

A chi mi fa sorridere

– Two things fill the mind with ever new and increasing admiration and awe, the more often and steadily we reflect upon them: the starry heavens above me and the moral law within me. I do not seek or conjecture either of them as if they were veiled obscurities or extravagances beyond the horizon of my vision; I see them before me and connect them immediately with the consciousness of my existence. –

Immanuel Kant, Phylosopher (1724-1804)

– I can live with doubt, and uncertainty, and not knowing. I think it's much more interesting to live not knowing than to have answers which might be wrong. –

Richard Feynman, Physicist (1918-1988)

Acknowledgments

I'm writing these words as introduction to my PhD thesis because my family supports all my choices and understands my passion for this "world".

My advisor, tutor or supervisor (I will never understand what the proper title is) Professor Pasquale Vena played a fundamental role in everything that I learn in my PhD, helping me in any problem and teaching me the "secrets" of continuum mechanics in all its forms: I'll be always grateful for this.

I thank Professor Steve Klisch, from California Polytechnic State University, for the scientific support in my Californian months, with the wish to have the possibility to work again together; and, together with its family, for helping in my daily life. I also thank Dr. Ben Beake, from MicroMaterials, to have done the same in my Welsh months.

I do not mention singularly all the guys at LaBS: I hope I've been a good colleague (with all my defects) as you did for me. Even if this work and this world means "a lot!!!" for me, I'm not crazy now also because all of you and Piero, Patrizia, "L'Averno", Fabio, Claudio, Cesco, Antonio, Serena, Daria, Claudia, Leo, Alessio, "Gli amici Marchigiani", as real friends. Especially, I'm sure I will never forget the scary lasts months and the strong discussions with Elena!!!

A special though is for Kevin and Matt that welcomed and treated me as an old friend. I really hope to meet each other again, in a lab or during a vacation.

Now... enjoy ,

Matteo

Contents

List of Abbreviations

Here a list of the most common abbreviations used in the present work of thesis

ABBREVIATIONS	TERMS
AC	**Articular Cartilage**
PDMS	**Polydimethylsiloxane**
AFM	**Atomic Force Microscope**
NI	**Nanoindenter**
DMA	**Dynamic Mechanical Analysis**
COL	**Collagen**
PGs	**Proteoglycans**
GAGs	**Glycosaminoglycans**
MAT	**Matrix**
ECM	**Extracellular Matrix**
OA	**Osteoarthritis**
SLS	**Standard Linear Solid**

NB: The nomenclature used in a Chapter is independent from the one used in the others, except when explicit calls to Equations or quantities previously defined are done.

Introductory Chapter
Motivations and Aims of the Thesis

This introductory Chapter explains the purposes behind this work of thesis. Section I lists the motivations and the approaches chosen to answer the addressed questions. The global structure and the outline of the thesis is shown in detail.

Introductory Chapter
Motivations and Aims of the Thesis

The interest on discovering, describing and explaining the properties of materials, any kind of material, is a field of research that played a very important role in the story of science: the understanding *of how it works* and *how it is made* tempts the scientists from ancient time. Looking at the purposes of this research, the applications of the knowledge extracted from these studies span over a wide range: civil, environmental, military and biomedical are just few examples that can be suggested.

The properties of a material can be investigated by studying its response to an applied external stimulus; it is easy to realize how vast is the range of possible stimuli to apply, allowing different *physics* to investigate different aspects of the same phenomenon such as, for examples, fluidics, electromagnetism or solid mechanics.

Theories and experiments are two faces of the same medal: first, one has to set up a test with which some quantities (averaged on the volume under consideration) can be extracted and, second, a theoretical framework has to be proposed in order to explain how (and why) these quantities result from the structure of the material; of course, the vice versa holds, since a theory can be suggested and a test is consequently set up to verify it. In between this two aspects, in my opinion, is the numerical approach; in fact, a theory can be translated into the numerical alphabet and a virtual experiment can be run. The use of numerical testing signs an important improvement towards the understanding of material properties since some hidden quantities in *real world* can be easily manipulated in the *numerical one*: inverse analysis is a very powerful tool.

Among all the materials, biological tissues are certainly one of the most interesting: the possibility to apply the knowledge on them to cure or prevent pathologies and to assure better conditions of life can be considered as the main aim of scientific research; the possibility to use something that reproduces their specific features to build artificial devices is, also, a big motivation toward this kind of investigation. Difficulties in this field span from experimental issues -how to collect samples, how to preserve them, how to test them under the correct environment and proper boundary conditions- to theoretical one -which aspects have to be considered and which one can be neglected, what assumptions are the correct, how that phenomenon can be described-. Nowadays, a further interest that, in some sense, introduces complications, is raising: the more precise understanding on the hierarchical structure of this tissues makes the analysis at lower and lower scales essential to proceed towards a bottom up explanation of their overall properties. The analysis of the properties at small scales and the explanations about why and how they are linked each other through these characteristic lengths define fields full of open questions.

Indeed, it often happens that the measure of a particular parameter for a tissue can result in different numerical values depending on the characteristic length of the observation tool (experiment). To establish a unique structure - property relationship holding at all length scale is a big challenge. This is the reason why the explanation of the structure at microscale and nanoscale is so important: from the microstructure, indeed, the macrostructure is built.

I. OUTILINE OF THE THESIS

This work is centered on the study of articular cartilage making use of nanoindentation tests in both time and frequency domain, through experimental, numerical and analytical methods. Articular cartilage is a paradigmatic tissues with respect to the above mentioned considerations. Its principal functions of transferring loads between joints surfaces is performed by its specific microscopic structure. Even if articular cartilage has been studied from the sixties (the studies on the consolidation in geotechnics has been used as starting point to explain poroelasticity in cartilage), its characterization at nanoscale and microscale is, instead, something still not well understood and the actual works suggest interesting complexities that need deeper studies.

The motivations, from which the aims of this work arise, are listed below.

1. The superficial layers of articular cartilage play an important role in both the biomechanics of the whole tissue and the maintenance of its integrity.

Averaged properties can describe the overall mechanical behavior of the tissue but they cannot catch the specific aspects of the local organization. Since the overall behavior comes from the local mechanics and keeping the outstanding importance of the superficial layers, this study in focused on the upper $30\,\mu m$ of the whole thickness of the tissue, investigated through contact lengths from tens of nanometers to hundreds of micrometers. Nanoindentation test is chosen as suitable experimental methodology capable to help in this kind of investigation; the introduction of concepts as characteristic lengths and equivalent deformations allow to a better explanation of the results.

2. The approach described by the dynamic mechanical analysis is extensively used at macroscale, showing its advantage in investigating material properties with respect to time domain. Its application at microscale is, instead, an open field of research.

This approach is applied in conjunction to the nanoindentation technique with the purpose to highlight the behavior of the articular cartilage at different characteristic lengths as well as at different frequency (i.e. different strain rates). The different and

peculiar aspects of articular cartilage can, potentially, be discriminated each other, giving the possibility to suggest their relation with the specific microstructure solicited: the dichotomy between poroelasticity (extrinsic time dependency) and viscoelasticity (intrinsic time dependency) is investigated up to the role of the single bundle of fibers. The interest in investigating high frequency range is related to the importance of instantaneous response (limit to the undrained condition) of the tissue.

3. The first organization of articular cartilage, over the single constituents, is at micrometric scale: at this length, the knowledge is still not complete and further investigations are required. Nanoindentation tests in time domain appear suitable to extract constitutive parameters characteristic of this microstructure.

Indentation tests have shown its capability to probe mechanical properties of a material; nanoindentation tests is an already well - established technique in the field of hard biological tissue. In the present work, multiload nanoindentation creep tests are considered and they are used to investigate the poroelastic properties of articular cartilage, varying contact lengths and equivalent strains. By adapting the consolidation theory of a poroelastic material under confined compression test, a fast analytical tool for structural parameters identification is obtained.

4. Even if the dynamic mechanical analysis appears a promising methodology to investigate material properties, no optimized and dedicated numerical tools capable to simulate a dynamic problem directly in frequency domain are present commercially.

An homemade code, written within a Matlab environment, is developed to simulate the dynamic tests. Once this code is validated, it can be used in an inverse process for parameters identification.

5. A wide range of constitutive models are described in literature, investigating single aspects of this biological tissue. Its physical complexity requires numerical models capable to take into account for all the single components and their mutual interactions, especially if a micrometrical characterization is the objective.

A numerical model based on the three classes of constituents (matrix, collagen and proteoglycans) is developed; collagen fibrils distribution plays a key role in this model. The particular situation of nanoindentation test is considered; with respect to simulate macroscale tests, this testing procedure introduces further numerical complexities due to the strong geometrical nonlinearities that characterize this problem.

6. In order to achieve a complete understanding of the tissue, the different experimental methodologies have to be compared and coupled each other. Besides, the proposed numerical tools have to show their capabilities to explain experimental results, toward an insight understanding of the tissue.

All the investigation proposed in this work are carried out on native articular

cartilage. A long term objective that can start from the present work of thesis is the possibility to apply robust and reliable experimental and numerical tools to the investigation of engineered tissues or pathological conditions. Then, attempts to perform a comparison among experimental results or to couple the different numerical methodologies have to be suggested.
According to the stated objectives, Figure I explains a scheme of the thesis.

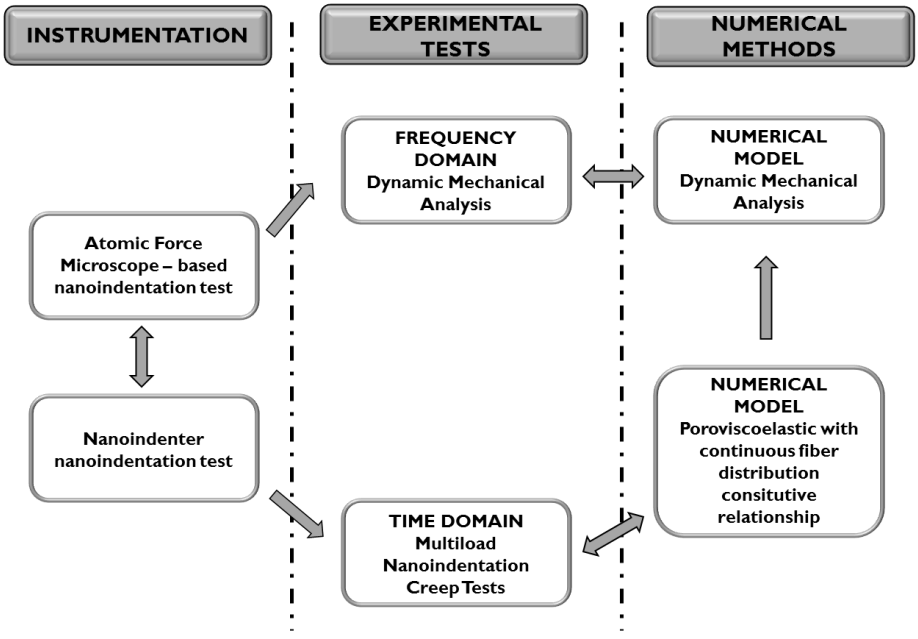

Figure I: Flow diagram describing thesis contents.

Two instrumentations are considered, an Atomic Force Microscope and a Nanoindenter: for the purpose of this thesis, the instruments differ each other for the characteristic lengths analyzable and for the domain in which the experiments are carried out. Atomic Force Microscope allows an investigation in frequency domain at lower scales (up to few micrometers) and Nanoindenter permits an investigation in time domain at higher ones (up to hundreds of micrometers). Two numerical methods are proposed: a novel tool for the simulation of harmonic tests and a poroviscoelastic constitutive relation that account for a continuous fiber distribution. At the first stage, the model for dynamic tests is used to a parameter identification process based on the relative experimental data. Then, the constitutive relation is used to suggest explanations for time domain experimental evidences and to improve the dynamic model.

Chapter 1 provides a general description of the structure of articular cartilage, showing its characteristic components and highlighting the length and time scales investigated in this work; pathological conditions and engineered tissues are also briefly described. Chapter 2 contains a general presentation on both theoretical and experimental approaches that can be found in literature with their application is characterizing articular cartilage; results from these references will be used as a starting point to explain the ones obtained in this work. A precise description of the experimental setups is shown in Chapter 3: both the two instrumentations are presented as well as the consolidated theoretical approaches to analyze a nanoindentation test. The specific theoretical background, related to the particular application investigated, is presented in each specific Chapter. All the experiments are presented in Chapter 4, devoting a single Section for each of the three different situations: dynamic tests on bovine native cartilage, multiload nanoindentation creep tests on bovine native cartilage and multiload nanoindentation creep tests on engineered porcine cartilage. Chapter 5 is focused on the presentation of the homemade code that simulate the harmonic test: all the details relative to the theoretical background, its numerical implementation with a sensitivity analysis and the application on nanoindentation test are shown. In Chapter 6 the poroviscoelastic model with continuous fiber distribution is described and preliminary applications to time domain nanoindentation test are shown. For each subject, detailed discussions are provided singularly: in Chapter 7, moreover, a global discussion that try to connect the results described separately is performed; furthermore, both the conclusions and the suggested improvements of the present work are proposed in this last Chapter.

This work is inserted in a project founded by the Italian Ministry of University and Research, through the PRoject of National Interests program (PRIN2008), developed in collaboration with the Electronic and Biophysical Department of University of Genova. In particular, dynamic experiments are carried out in this department and I thank for the possibility to analyze those data and for the continuous feedbacks to improve experimental setup and to explain results. It is also my will to thank Istituto Ortopedico Galeazzi for the possibility to apply the developed methodology based on creep test on engineered articular cartilage tissue, providing a promising applicative example coming from the presented thesis. The novel constitutive relationship has been developed in collaboration with Professor Stephen Klisch at Mechanical Department of California Polytechnic State University: I thank him for his fundamental role and the whole scientific support of his laboratory.

Chapter I.

Introduction: Articular Cartilage

In this Chapter, an overview on the structure, from micro to macro, of articular cartilage is provided in detail. Section 1.1 shows an anatomical description of the tissue. Section 1.2 highlights the importance of both dimensional aspects and interconnections among the components and justifies the importance of the superficial layers on the overall function of articular cartilage. In Section 1.3, the pathological condition and engineered constructs are briefly presented. Section 1.4 introduces a material used in the present work as a viscoelastic reference, the polydimethylsiloxane.

Chapter I.
Introduction: Articular Cartilage

Biological materials are the main constituents in plant and animal bodies and cover a diversity of functions. They can offer mechanical functions, providing protection and support for the body, serving as ion reservoirs (bone is typical example), chemical barriers (like cell membranes), transfer for chemicals into kinetic energy (as in muscles) or have catalytic functions (such as the enzymes) (Fratzl & Weinkamer, 2007).

Materiomics is defined as the study of the properties of natural and synthetic materials by examining fundamental links between processes, structures and properties at multiple scales, from nano to macro, by the use of experimental, theoretical or computational methods (Espinosa, Rim, Barthelat, & Buehler, 2009).

From the idea suggested by the *universality - diversity paradigm*, the analysis of biological materials has to take into account for the presence of universality and diversity in both fundamental structural elements and functional mechanisms (Buehler & Ackbarow, 2008). The elementary building blocks are the same in a wide variety of biological materials where they create extremely robust and multifunctional materials by *self - organized* structures over many length scales; this means those structures are highly conserved, as alpha-helices or beta-sheets in the definition of collagenous structures. In contrast, other features are highly specific to the single tissue. This coexistence of universality and diversity is an overarching feature in biological materials and a crucial aspect in materomics.

A systematic analysis of biological materials in the context of linking chemical and physical aspects with structural and mechanical properties is of primary importance. A rigorous understanding about how the matter that makes life *works* is needed in order to explain the fundamental principles of these structures like, for example, the assembly procedures or the deformation processes (Buehler & Ackbarow, 2008).

Biological structured tissues, as well as any artificial device, is based on optimization processes among function, form and material; these three aspects are strictly related and overlap each other (see Table 1.1). In natural materials, shape and microstructure are intimately related due to their common origin, which is the growth of the organ (Jeronimidis, 2000). Growth implies that form and microstructure are created in the same process: *self - assembly* allows biological structure to remodel and to adapt to the changing environmental conditions during their whole lifetime (Thompson, 1992). Hence, the final result derives from a dynamic evolution and it is not *a priori* design: the microstructure at each position of the tissue is adapted to the local needs, leading to high flexibility at all the levels. The basic organization is at nanometer length scale. Built blocks at higher levels are obtained through a self-assembly process: the simple rules of mixing the bulk properties of the single constituents do not work since the properties themself do not scale linearly (Siegel, 1993).

Table 1.1: Biological and engineered materials are governed by a wide choice of base elements and by different modes of fabrication. [Adapted from (Fratzl & Weinkamer, 2007)].

BIOLOGICAL MATERIAL	ENGINEERED MATERIAL
LIGHT ELEMENT dominate: C, N, O, H, Ca, P, S, Si	LARGE VARIETY of element: Fe, Cr, Ni, Al, Si, C, N, O
GROWTH by biological controlled self-assembly (approximate design)	FABRICATION (exact design)
HIERARCHICAL STRUCTURING at all size levels	FORMING of the part and MICRO-STRUCTURING of the material
ADAPTATION of form and structure to the function	SELECTION of material according to function
MODELING and REMODELING: capability of adaptation to changing environmental condition	SECURE DESIGN
HEALING: capability of self-repair	

Mechanical properties of biological materials insert in the following ranges: i) the density is low and rarely exceeds $3\frac{kg}{m^3}$; ii) Young's moduli vary from $1\ MPa$ to $100\ GPa$; (iii) strength is almost as broad as the Young moduli, varying over four orders of magnitude ($0.1 - 1000\ MPa$).
According to these properties, biological materials can be classified as follow (Fratzl & Weinkamer, 2007): i) ceramic and ceramic composites (teeth or bones, where the mineral component is high); ii) polymer and polymer composites (ligaments and tendons); iii) elastomers (skin, muscles or blood vessels that undergo large deformation); iv) cellular material.

1.1 ARTICULAR CARTILAGE

Articular cartilage (AC) is a specialized connective tissue that covers the surfaces of diarthrodial joints, such as the knee and the hip. Its principal function is to provide a lubricated surface for articulation and to facilitate the transmission of loads between joints with low friction coefficient (Pearle, Warren, & Rodeo, 2005) (Raviv, et al., 2003). Structurally, AC is a porous solid matrix saturated by physiological fluid. The single components that build the structure, and the ways with which they are mutually arranged, give the AC peculiar properties.

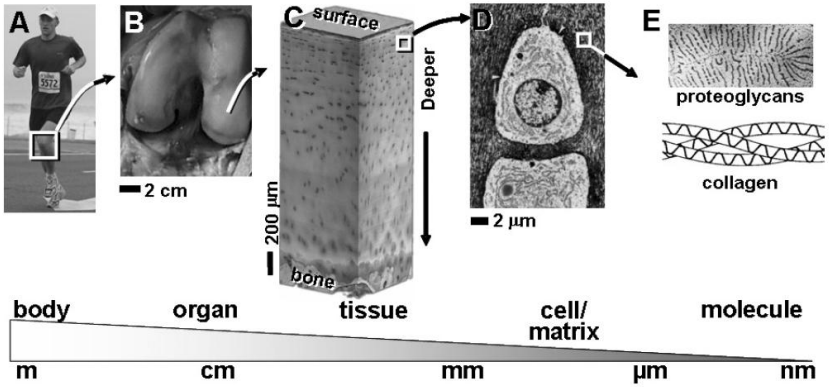

Figure 1.1: Articular cartilage at different length scale. (A) Human knee joints are covered with (B and C) articular cartilage containing (D) chondrocytes sparsely embedded in extracellular matrix, largely consisting of (E) proteoglycans, collagen and hydrated in synovial fluid (Bae & Sah, 2008).

From the point of view of materomics, AC is an awesome tissue. As suggested in Figure 1.1, AC is a complex material since its macroscopic role in the biomechanics of joints can be analyzed by subsequent steps starting from the constitutive blocks at nanometric length. AC is an inhomogeneous, anisotropic, non-linear, depth and time dependent tissue. Inhomogeneity means that its properties vary with the position and the location under analysis; the properties of an anisotropic material change looking at different tissue orientation; a non-linear behavior is typical of materials that undergo to large deformations; time and depth dependent aspects can not be neglected when this tissue is evaluated, since the optimized way with which AC responds to the stimuli arises from them.

Therefore, AC is a paradigm of complex tissue with mechanical function and a great example to motivate the use of the concepts of dependencies, in length and time, and of assembly of constitutive blocks. Recent works (Chandran & Barocas, 2006) (Tang, Buehler, & Moran, 2009) (Maceri, Marino, & Vairo, 2010), in fact, has shown that the macro-scale mechanics of cartilage does not follow directly from the particular mechanics of the individual fibrils at microscale, but that the tissue strength strongly depends on their arrangement at higher levels: as a consequence, the macroscopic behavior of AC is correlated with the microscopic structure, from which its investigation must begin.

Actual studies on AC highlight the importance of considering the interactions across the scales; but challenges in developing theories and models that predict and explain the three dimensional macroscale mechanical performance from microscale structure define a wide, and still opened, field of research.

1.2 STRUCTURE, ORGANIZATION AND CONSTITUENTS OF ARTICULAR CARTILAGE: EFFECTS ON TIME AND LENGTH SCALES

AC is a connective tissue that covers the surface of articular joints in a range of thickness varying from 0.5 mm to 5 mm: for example, larger thickness is typical of joints in the lower limbs in human (Ateshian, Soslowsky, & Mow, 1991). Its macroscopic properties, just outlined in the previous Section, come from the hierarchy of its elaborated and highly ordered organization (Mow, Ratcliffe, & Poole, 1992).

At microscale level ($10^{-7} - 10^{-6}\ m$), the biochemistry and the organization of cartilage are maintained by the chondrocytes, the sole type of cell existent in AC tissue; the chondrocytes and the surrounding pericellullar matrix define a single unit called chondron (Figure 1.2).

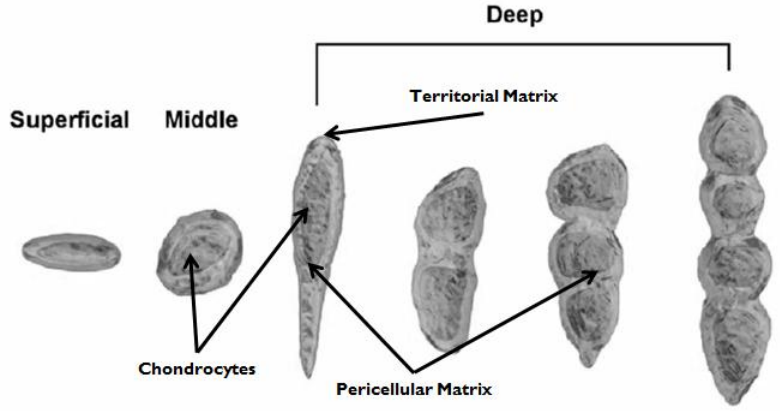

Figure 1.2: Chondron structure throughout cartilage thickness. Reprinted from Osteoarthritis and Cartilage, 14, Youn, Choi, Cao, Setton, Guilak, Zonal variation in the three-dimensional morphology of the chondron measured in situ using confocal microscopy, Pages 889-897, Copyright (2006), with permission from Elsevier [OR APPLICABLE SOCIETY COPYRIGHT OWNER].

The whole mass of chondrocytes define only the 1% of the overall volume: they do not play a direct role in the mechanical properties of AC but they are biologically active, providing the organization of the structure as a response to the external stimuli (Silver, Bradica, & Tria Jr., 2003). Chondrocytes are present throughout the thickness of the tissue, differentiating from zone to zone in terms of size and shape, but maintaining the ability of producing, degrading and remodeling the extracellular matrix (ECM): they are responsible for the creation of the nanoscale networks.

The extracellular matrix is composed by a network of macromolecules (it can be referred to a lengths scale of $10^{-8} - 10^{-6}\ m$), that defines the porous skeleton of

the tissue. At this scale, the significant mechano-electro-chemical transductions, that modulate cellular anabolic and catabolic activities, occur. Basically, the structural macromolecules of the matrix are collagen (COL) and proteoglycans (PGs).

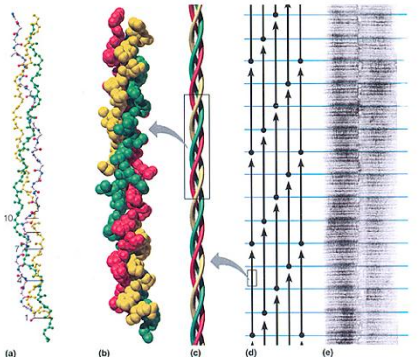

Figure 1.3: Scheme of collagen structure from atoms (a) to fiber (e) (from http://www2.mcdaniel.edu/Chemistry/CH3321JPGs/Proteins).

Collagen (Figure 1.3) contributes up to 80% of dry weight (10 - 20% of the wet weight) and it is almost uniformly distributed throughout the tissue, except for the superficial layers in which it is highly packed. Different types of collagen are present in AC: type II, type VI, type IX, type X and type XI. Type II is the most abundant (95%). The basic structure of collagen is the triple helix of three 1D proteic chains, each of which is 300 nm in length; a single monomer of triple helix connects to the others giving the molecule of tropocollagen. Tropocollagen can self-aggregate in a quarter stagger manner through covalent crosslinks of characteristic banding of $64 - 100\ nm$. (Abbot, Levine, & Mow, 2003). The 3D assembly gives the fibril of collagen that, in the case of type II collagen, has a diameter ranging from $20\ nm$ to $70 - 120\ nm$, depending on the position, and it is arranged with an interfibrillar spacing of $\sim 100\ nm$ (Han, Grodzinsky, & Ortiz, 2011). The large slenderness ratio (ratio between the length and the diameter) explains how collagen has no resistance in compression but it is very strong in tension; this function is magnified by the fact that this molecule is highly packed with chondrocytes and the other ECM macromolecules (Mow, Zhu, & Ratcliffe, 1991).

PGs are produced by the chondrocytes in the pericellular matrix, but they are built in their final form only in the interritorial space. Proteoglycans consist of a protein core and one or more glycosaminoglycans (GAGs) chains. GAGs are long unbranched polysaccharide chains consisting of repeating disaccharides that contain an amino sugar: they are negatively charged with an interspace of $10 - 20\ \dot{A}$. Typical GAGs in AC are the hyaluronic acid (HA), the chondroitin sulfate and the keratin sulfate.

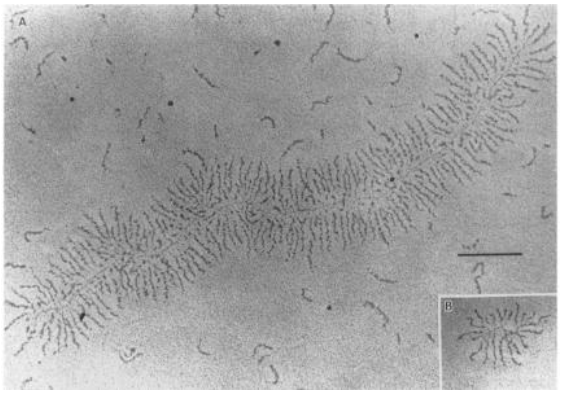

Figure 1.4: PGs aggregates of a calf (A) and steer (B) from electron micrograph. The bar indicates 500 nm. [Adapted from (Buckwalter, Mankin, & Grodzinsky, 2005)].

The most important class of PGs is constituted by large aggregates called aggrecans (90% of all PGs) that fill the interspaces in between the collagen network; moreover, aggrecans can covalently bind each other through the long HA molecules ($1 - 7\mu m$) to create larger macromolecules that keep anchored the smaller PGs in their positions (Figure 1.4): the consequent effects are the stabilization of the structure and the possibility to absorb impulsive solicitations, by storing energy (Mow, Ratcliffe, & Poole, 1992). HA has also a major role in lubrication and frictional interactions. Aggrecans have a core protein backbone of about $400\ nm$ in length whereas the connected GAGs have a length of $40\ nm$; the interspace defined by HA molecules is about $20 - 50\ nm$.

Thus, ECM (Figure 1.5) can be considered a porous and permeable fiber reinforced matrix, resulting of a mechanical interaction of two macromolecular networks: a permanent network of insoluble collagen fibers, characterized by a low turnover rate (Eyre, 1980), and a soluble one of large proteoglycans, characterized by an high turnover rate (Hardingham, Muir, Kwan, Lai, & Mow, 1987).

Water contributes up to 80% of the wet weight of AC, with its percentage varying with the depth (Marondas, Wachtel, Grushko, Katz, & Weimberg, 1991). It contains gasses, small proteins, metabolites and, important, positive charged ions as Na^+, K^+ and Ca^+ (Wilson, van Donkelaar, & Huyghe, 2005). It is free to move through the solid network; its movement is regulated by the physical porosity and, more important, by the hydrophilic attraction of the negatively charged PGs that rises the interstitial pressure. This phenomenon is called swelling effect and has the consequence to generate a non-zero strain in the cartilage solid matrix in absence of externally applied load (Narmoneva, Wang, & Setton, 1990); this phenomenon maximizes the volume occupied by the tissue.

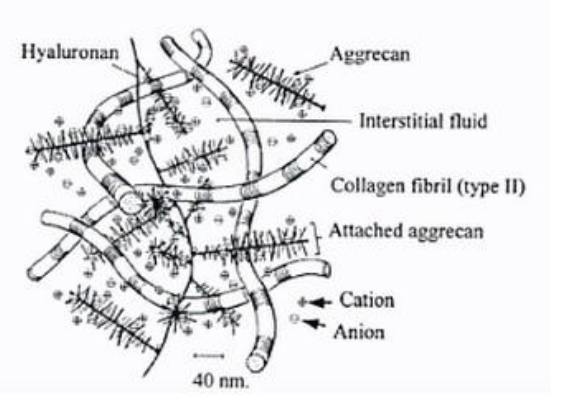

Figure 1.5: Cartoon of the network that defines the extracellular matrix; the net of collagen fibers and PGs is highlighted [Adapted from (Mow, Zhu, & Ratcliffe, 1991)].

The interaction between water and solid matrix (manly, PGs) takes place at nanoscale levels ($[10^{-10} - 10^{-9}\ m]$) and, other than swelling, it is responsible also for the hydraulic permeability and the compressive and shear strengths. The hydraulic permeability has also a mechanical nature: adult human cartilage has a porosity ranging from 68 and 75% (Ateshian & Hung, 2006) and a typical pore size estimated between 3 nm and 6.5 nm (Mow, Holmes, & Lai, 1984). Water has also the functions to lubricate the joint and to transport nutrients and catabolites, passing from the ECM to the synovial cavity, the space in between the two cartilagineous surfaces that compose an articulation.

The study of how the macroscopic behavior follows from such a complex microscopic structure is an interesting task: a couple of examples can help to better sense this statement. i) AC tissue shows hysteresis at the macroscale whereas this behavior is not evident in isolated fibril mechanics: this is indicative of the presence of a friction-like sliding motion among the tissue components. ii) AC has structures intrinsically designed to sustain tension (COL) and compression (PGs and water): in terms of response, instead, the differences between tension and compression (the so called *tension - compression bimodularity*) reduce to the conclusion that AC is optimized to sustain basically compressive loads; nevertheless, it is worth to be noted that any kind of solicitation is converted in a complex field of tensile, compressive and shear stresses, due to microstructure and anatomy of the tissues.

Looking at how the components are spatially distributed, a classification can be made based on morphologic aspects, as proposed by Buckwalter (Buckwalter, Mankin, & Grodzinsky, 2005). Four zones can be identified: the superficial zone, the transitional zone, the middle zone and the calcified zone as shown in Figure 1.6.

The superficial zone is the thinnest AC zone and it is composed by two layers. A sheet of fine fibrils with little polysaccharide and no cell covers the layers composed by flattened ellipsoid-shaped chondrocytes arranged parallel to the surface. Chondrocytes density is very high as well as collagen; PGs has a low concentration, instead. Collagen fibrils are preferably aligned parallel to the surface, defining an interwoven network that determines AC peculiar mechanical properties and limits the movements of the macromolecules. This zone is also characterized by the highest water content, almost the 80% of the wet weight.
In the transitional zone the cells assume an ovoidal shape and produce collagen with larger diameter; the PGs concentration is increasing, the water concentration remains constant and the collagen concentration is decreasing.
In the middle zone, the collagen fibers have the largest diameters, the PGs concentration is the highest, gaining its maximum at almost the 33% of the whole thickness whereas the concentration of water starts to decrease (from almost the 25% of the whole thickness to the bottom). Chondrocytes arrange themselves in columns perpendicular to the joint surface; collagen fibers are randomly distributed.
The calcified zone defines the transition to the cancellous bone; cells are small and spherical; their metabolic activity is low. Collagen fibers are preferably arranged perpendicularly to the bone surface.

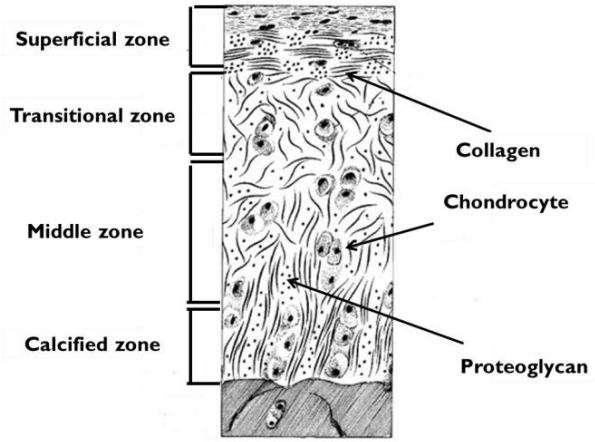

Figure 1.6: Full thickness scheme of AC; the different layers are separated and the distribution of the single components is presented (http://www.cvmbs.colostate.edu/ns/departments/clinsci/equineortho/orthopaedic_topics/equine_joints.asas).

The division proposed above makes clear the variability of the tissue along the thickness. Works as the one presented by Appleyard (Appleyard, et al., 2003),

moreover, shows that noticeable differences in constituents concentration and, as a consequence, in mechanical response, can be found among different sites across the surface of the AC.
Mechanical properties of cartilage are also time and history dependent, that is, the observed strain will be different when the rate at which stress is applied changes and when different stress paths are followed to arrive at the same final load. Both viscoelastic and poroelastic properties, the mechanical aspects and modeling of which will be described later on, can be explainable looking at the microstructure of AC. Viscoelasticity is an intrinsic property that depends on the structure of the macromolecules and their evolution under stress; a secondary reason is the so called flow-induced viscoelasticity that is due to the diffusive drag resulting from the flow of fluid within the ECM matrix (Ateshian & Hung, 2006). Poroelasticity, instead, is an extrinsic property depending on the dynamic with which the fluid flows through the solid matrix. According to the dimensional description, then, it can be interesting to understand how these two properties take part in the tissue mechanics: indeed, they mix themselves through different time and lengths scales without a completely understood balance, especially at micrometric lengths. In the following Chapters more considerations can be done and explanations suggested, analyzing the results of this thesis.

1.2.1 The superficial layers

Since superficial layers of the articular cartilage are crucial for both mechanical functions of healthy tissue and for damage initiation in pathological one, there is a major interest in investigating the properties of the top 20% of the overall surface.
Superficial layers interface AC with the surface of the opposite joint: it has lubrication and wear functions. During joint movements, it supports any kind of stress. In fact, it acts as a *drumhead*: any compressive solicitation, localized in a precise zone, is immediately redistributed all over the whole surface, preventing dangerous peak of stress (Silver, Bradica, & Tria Jr., 2003). The work of Setton (Setton, Zhu, & Mow, 1993) evaluates the importance of this layer on the compressive behavior of all the AC: its removal increases the permeability and the amount of load directly sustained by the network of macromolecules. Early effects of osteoarthritic degeneration can be referred to the damage of the cartilagineous network in the superficial layer; then, the pathological condition extends towards the whole AC thickness. The densely packed framework of the surface limits the ingress of the large macromolecules of synovial fluid and the egress of the large cartilage molecules, acting as a barrier to protect the whole AC.
Thereafter, for its large and important role on the mechanical properties and the biochemical maintenance of AC, this work is basically focused on the superficial

layers investigation.

1.3 OSTHEOARTHRITIC (DIGESTED) CARTILAGE AND ENGINEERED TISSUES

Ostheoarthritis (OA) is a joint disease characterized by cartilage degeneration, a thickening of the subchondral bone and formation of marginal osthophytes. As well as the structural modifications of the structure of the tissue, pain and limitation of the movements are the macroscopic effects of this pathology.

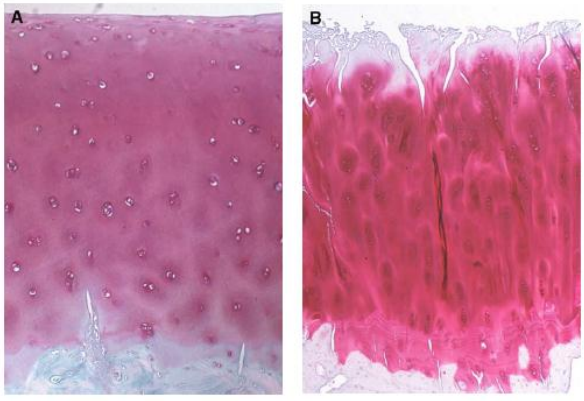

Figure 1.7 Full thickness comparison of healthy human cartilage (A) and OA cartilage (B); the effect on PGs is highlighted. Reprinted from Clinics in Sports Medicine, 24, Pearle, Warren, Rodeo, Basic science of articular cartilage and osteoarthritis, Pages 1-12, Copyright (2005), with permission from Elsevier [OR APPLICABLE SOCIETY COPYRIGHT OWNER].

The OA process is directly linked to the loss of PGs content and composition (Pearle, Warren, & Rodeo, 2005): in particular, at the earliest stage, PGs appear shorter and unbound to hyaluronate, resulting to a coarser extracellular network. The content in collagen remains initially constant and, in a second stage, it starts to decrease itself. Qualitatively speaking, the permeability increases, decreasing the pressurization of the tissue, whereas the stiffness decreases as a consequence of the previously described change in microstructure. Phenomena of delamination of the superficial membrane can be seen at the early stage, driving towards the exposition of chondrocyte directly the synovial cavity (Wu, Kirk, & Zheng, 2008). The key point is that AC has a very limited capability of self-healing (Poole, et al., 2001).
Aging effects follow the same path just hint above in the case of OA.
Ostheartritic samples can be produced *in vitro* by the use of enzymatic treatments that want to simulate the conditions at different grade of pathology.

The unique mechanical properties of AC do not derive only from the concentrations of the single components; more important is how they interact and they are organized. The growth itself governs the properties of the final tissue that, however, continuously renews its structure as an answer to the external stimuli. The developing of engineered AC is a difficult task for the proposed reason: mixing together the right components in the right proportions does not mean to obtain AC tissue (Buckwalter, Mankin, & Grodzinsky, 2005). In this sense, the ideal scaffold should mimic the architectural and structural properties in order to permit the correct differentiation and metabolism of the cells; it has also to be biocompatible and mechanically stable. There are several types of scaffold and several techniques to use them, adding or deleting (with different timing) specific cell sources and active biomolecules (Lopa, Colombini, de Girolamo, Sansone, & Moretti, 2011). This wide range of possibilities, merged to the promising results obtained in the field of repairing damage tissues, shows the importance of suitable mechanical tests and proper models to evaluate the properties of engineered tissues with relation to the native ones. The scaffold in which the engineered tissues analyzed in this work is cultivated is here presented, as example: according to the work of Dadsetan (Dadsetan, Szatkowski, Yaszemski, & Lu, 2007), this scaffold provides a tuning compressive stiffness regulated by the polymer concentration and, in general, the mechanical properties can be varied changing the ratio among the components; it is degradable and the degradation rate depends on its composition, giving the possibility to adjust it to the particular situation with the objective to provide an initial support that decreases with the growth of the tissue; this material allows the cells to be attached and to growth.

1.4 POLYDIMETHYLSILOXANE

Polydimethylsiloxane (PDMS) is a silicone elastomer. The chemical formula of a single chain is $CH_3[Si(CH_3)_2O]_vSi(CH_3)_3$ where v is the number of the repeating monomers $[Si(CH_3)_2]$. Network of PDMS polymer is composed by crosslinking the chains. PDMS is very attractive in the field of biological application as testing material and component for devices. It is chemically inert, thermally stable, permeable to gases, simple to handle and it has a low cost production (Mata, Fleischman, & Roy, 2005).

For its preparation, two agents are required: a base agent and a curing agent. The ratio with which they are mixed can be varied according to the particular needs to obtain tunable properties: the number v of monomers and the crosslinks depend on this ratio (McDonald & Whitesides, 2002). The higher is the ratio between base agent and curing agent, the softer is the material; the higher is this ratio, the lower is

the number of crosslinks and the material is less viscous.
The characteristic structure of this polymer allows to use it as reference material in a wide range of applications: in this sense, its big advantage is to be isotropic and homogeneous. If the sample is tested in dry conditions (or submerged in a non-organic solvent), its structure is impermeable: this means that it acts as a viscoelastic material; this aspect avoids any size dependencies of its properties, reducing its behavior to be only time dependent. If the sample is submerged in non-polar organic solvents, instead, it shows a poroelastic or poroviscoelastic behavior, depending on the grade of diffusivity of the chosen solvent (Hu, Chen, Whitesides, Vlassak, & Suo, 2011).

REFERENCES

Abbot, A., Levine, W., & Mow, V. (2003). Biomechanics of articular cartilage and menisci of the adult knee. In J. Callaghan, A. Rosemberg, H. Rubarh, P. Simonian, & T. Wickiewicz, *The adult knee Vol. I* (pp. 81-102). Philadelphia: Lippincott Williams & Wilkins.

Appleyard, R., Burkhardt, D., Ghosh, P., Read, R., Cake, M., Swain, M., & Murrel, G. (2003). Topographical analysis of the structural, biochemical and dynamical biomechanical properties of cartilage in an ovine model of osteoarthritis. *Osteoarthritis and Cartilage, 11*, 65-77.

Ateshian, G., & Hung, C. (2006). The natural synovial joint: properties of cartilage. *Journal of Engineering Tribology, 220*, 657-670.

Ateshian, G., Soslowsky, L., & Mow, V. (1991). Quantitation of articular surface topography and cartilage thickness in knee joints using stereophotogrammetry. *Journal o Biomechanics, 24*(8), 761-776.

Bae, W., & Sah, R. (2008). Multi-scale biomechanics of articular cartilage. In S. Chien, P. Chen, & Y. Fung, *Introduction to Bioengineering 2nd Edition* (pp. 243-260). World Scientific Publishing.

Buckwalter, J., Mankin, H., & Grodzinsky, A. (2005). Articular cartilage and osteoarthritis. *AAOS Instructional Course Lectures, 54*, 465-480.

Buehler, M., & Ackbarow, T. (2008). Nanomechanical strength mechanisms of hierarchical biological materials and tissues. *Computer Methods in Biomechanics and Biomedical Engineering, 11*(6), 595-607.

Chandran, P., & Barocas, V. (2006). Affine versus non-affine fibril kinematics in collagen networks: theoretical studies of network behavior. *ASME Journal of Biomechanic Engineering*, 259-270.

Dadsetan, M., Szatkowski, J., Yaszemski, M., & Lu, L. (2007). Characterization of photo-cross-linked oligo[poly(ethyleneglycol) fumarate] hydrogels for cartilage tissue engineering. *Biomacromolecules, 8*, 1702-1709.

Espinosa, H., Rim, J., Barthelat, F., & Buehler, M. (2009). Merger of structure and material in nacre and bone - Perspectives on de novo biomimetic materials. *Progress in Material Science*, 1059-1100.

Eyre, D. (1980). Collagen: molecular diversity in the body's protein scaffold. *Science, 207*, 1315-1332.

Fratzl, P., & Weinkamer, R. (2007). Nature's hierarchical materials. *Progress in Material Science*, 1263-1334.

Han, L., Grodzinsky, A., & Ortiz, C. (2011). Nanomechanics of the cartilage extracellular matrix. *Annual Review of Material Research, 41*, 133-168.

Hardingham, T., Muir, H., Kwan, M., Lai, W., & Mow, V. (1987). Viscoelastic properties of proteoglycans solutions with varying proportions present as aggregates. *Journal of Orthopaedic Research, 5*, 36-46.

Hu, Y., Chen, X., Whitesides, G., Vlassak, J., & Suo, Z. (2011). Indentation of polydimethylsiloxane submerged in organic solvents. *Journal of Material Research, 26*, 785-795.

Jeronimidis, G. (2000). In *Structural biological materials, design and structure-property relationships* (pp. 3-29). Amsterdam: Pergamon.

Lopa, S., Colombini, A., de Girolamo, L., Sansone, V., & Moretti, M. (2011). New strategies in cartilage tissue enginnering for osteoarthirtic patiens: infrapatellar fat pad as an alternative source of progenitor cells. *Journal of Biomaterials and Tissue Engineering, 1*, 40-48.

Maceri, F., Marino, M., & Vairo, G. (2010). A unified multiscale mechanical model for soft collagenous tissues with regular fiber arrangement. *Journal of Biomechanics, 43*, 355-363.

Marondas, A., Wachtel, E., Grushko, G., Katz, E., & Weimberg, P. (1991). The effect of osmotic and mechanical pressures on water partitioning in articular cartilage. *Biochimica and Biophysica Acta, 1073*(2), 285-292.

Mata, A., Fleischman, A., & Roy, S. (2005). Characterization of polydimethyilsiloxane (PDMS) properties for biomedical micro/nanosystems. *Biomedical Microdevices, 7*(4), 281-293.

McDonald, J., & Whitesides, G. (2002). Poly(dimethylsiloxane) as a material for fabricatin micrfluidc devices. *Accounts of Chemical Research, 35*(7), 491-499.

Mow, V., Holmes, M., & Lai, W. (1984). Fluid transport and mechanical properties of articular cartilage. *Journal of Biomechanics, 17*, 377-394.

Mow, V., Ratcliffe, A., & Poole, A. (1992). Cartilage and diarthroidal joints as paradigms for hierarchical material and structure. *Biomaterials, 13*(2), 67-97.

Mow, V., Zhu, W., & Ratcliffe, A. (1991). Structure and function of articular cartilage and meniscus. In V. Mow, & W. Hayes, *Basic Orthopaedic Biomechanics* (pp. 143-198). New York: Raven Press.

Narmoneva, D., Wang, J., & Setton, L. (1990). Nonuniform swelling-induced residual strains in articular cartilage. *Journal of Biomechanics, 32*, 401-408.

Pearle, A., Warren, R., & Rodeo, S. (2005). Basic science of articular cartlage and osteoarthritis. *Clinics in Sports Medicine, 24*(1), 1-12.

Poole, A., Kojima, T., Yasuda, T., Mwale, F., Kobayashi, M., & Laverty, S. (2001). Composition and structure of articular cartilage: a template for tissue repair. *391 suppl.*, S26-33.

Raviv, U., Giasson, S., Kampf, N., Gohy, J., Jerome, R., & Klein, J. (2003). Lubrication by charged polymers. *Nature, 425*, 163-165.

Setton, L., Zhu, W., & Mow, V. (1993). The biphasic poroviscoelastic behaviour of articular cartilage: role of the surface zone in governing the compressive behavior. *Journal of Biomechanics, 26*(4), 581-592.

Siegel, R. (1993). Exploring mesoscopia - the bold new-world of nanosctructure. *Physics today*, 64-68.

Silver, F., Bradica, G., & Tria Jr., A. (2003). Structure and biomechanics of articular cartilage. In J. Callaghan, A. Rosenberg, H. Rubarh, P. Simonian, & T. Winckiewicz, *The adult knee Vol. I* (pp. 105 - 122). Philadelphia: Lippincott Williams & Wilkins.

Tang, H., Buehler, M., & Moran, B. (2009). A constitutive model of soft tissues: from nanoscale collagen to tissue continuum. *Annals of Biomedical Engineering, 37*, 1117-1130.

Thompson, A. (1992). *On the growth and form - the complete revisited edition.* Cambridge: Dover Publications.

Wilson, W., van Donkelaar, C., & Huyghe, J. (2005). A comparison between mechano, electrochemical and biphasic swelling theories for soft hydrated tissues. *Journal of Biomechanical Engineering, 127*, 158-165.

Wu, J., Kirk, T., & Zheng, M. (2008). Study of the collagen structure in the superficial zone and physiological state of articular cartilage using a 3D confocal imaging technique. *Journal of Orthopaedic Surgery and Research, 3*(29).

Youn, I., Choi, J., Cao, L., Setton, L., & Guilak, F. (2006). Zonal variations in the three-dimensional morphology of the chondron measured in situ using confocal microscopy. *Osteoarthritis and Cartilage, 14*, 889-897.

Chapter 2.

Models and Experiments in Literature

In this Chapter, relevant literature results on modeling aspects and experimental procedures for analyzing tissue mechanics are presented. In Section 2.1, general ideas on constitutive modeling are shown whereas in Section 2.2 common and innovative experimental approaches are described. Section 2.3 presents their application in analyzing articular cartilage and the state of art in this particular field, providing quantitative values for the mechanical properties at the available different length scales.

The macroscopic properties of AC likely depend on various microscopic histological and cellular features (Bao & Suresh, 2003) that cover a wide range of spatial scales, from nanoscopic over microscopic to macroscopic. This means that the material properties computed at macroscale are parameters that contain not only the physics of the phenomenon under investigation but also the effect of microstructure. Hence, finding the relationship between the macroscopic properties and the microscopic features is one of the most important challenge in the field of constitutive modeling and experimental testing.

There exists a large number of different methods for modeling materials, each optimal for addressing a different length or time scale. A main division is between phenomenological and microstructural/nanostructural approaches (Wu, 2011): the first one means that the constitutive laws are extracted by empirical observations of a phenomenon in a way consistent with fundamental theory, but not directly derived from theory; a great disadvantage is that the constitutive laws introduce many abstract parameters, which are often difficult to interpret and to identify. The other, instead, is based on the develop of structural model of single parts of the system under investigation to extract the overall behavior through the *summation* of single parts' behaviors.

2.1 GENERAL ASPECTS ON CONSTITUTIVE MODELING

One dimensional description of material is the simplest way to model it.

Using the terminology proposed by Fung (Fung, 1965), an elastic solid can be modeled using the Hooke law. Consider x the displacement applied; hence, the force F registered is $F = Ex$ where $E = f(x)$ defines the elastic properties of the material. If $E = const$, then the material is elastic linear.

A viscous material is a material such that the recorded force is $F = \mu\dot{x}$ where $\dot{x} = \frac{dx}{dt}$ is the first time derivative of the displacement and $\mu = g(x)$ defines the viscous properties of the material. If $\mu = const$, then the material is newtonian.

In Figure 2.1, the classical representation in the framework of lumped parameters of an elastic element and a viscous element is shown.

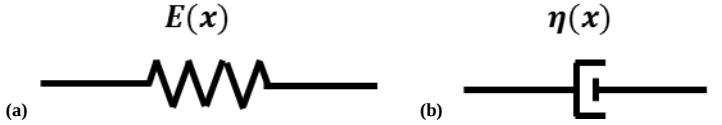

Figure 2.1: (a) Elastic element and (b) viscous element.

Viscoelasticity is the properties of materials that exhibit both viscous and elastic

behaviors when subject to a deformation; this means that, when a deformation is applied, the variation in stress is not instantaneous but the material needs a certain amount of time to dissipate the viscous aspect and to reach the elastic response.
A viscoelastic material can be obtained by combining the two presented behaviors. In the Maxwell model, the two elements are in series:

$$\dot{x} = \frac{1}{E}\frac{dF}{dt} + \frac{F}{\eta} \tag{2.1}$$

whereas in the Voigt model, the two elements are in parallel:

$$F = Ex + \mu\dot{x} \tag{2.2}$$

In the Standard Linear Solid model, the elements are combined in a more complex way: details on the configuration used in this work will be provided in Chapter 6.
Introducing the concept of hereditary law (Vito Volterra, 1860-1940), the general relation of a linear viscoelastic material can be derived as

$$x(t) = \int_0^t c_{creep}(t-\tau)\frac{dF}{dt}(\tau)d\tau \tag{2.3}$$

$$F(t) = \int_0^t k_{relax}(t-\tau)\frac{dx}{dt}(\tau)d\tau \tag{2.4}$$

where $c_{creep}(t)$ is the creep function and $k_{relax}(t)$ is the relaxation function. The above integrals stated that the behavior of the material depends on the present time and past history. Comparing Equations (2.3) and (2.4) with (2.1) and (2.2) respectively, the extraction of the creep and relaxation function for the specific case of one dimensional model is trivial.
The one dimensional relationship can be generalized by the use of tensors: the stress – strain relationship for an elastic material can be written as

$$\boldsymbol{S}_{\boldsymbol{stress}} = \mathbb{C}\boldsymbol{S}_{\boldsymbol{strain}} \tag{2.5}$$

where $\boldsymbol{S}_{\boldsymbol{stress}}$ and $\boldsymbol{S}_{\boldsymbol{strain}}$ are two rank two tensors describing, respectively, a measure of stress and a measure of strain, and $\mathbb{C}$ is a rank four tensor describing the elastic properties of the material, the stiffness tensor; inverting Equation (2.5), the compliance tensor $\mathbb{S}$ can be introduced:

$$\boldsymbol{S}_{\boldsymbol{strain}} = \mathbb{S}\boldsymbol{S}_{\boldsymbol{stress}} \tag{2.6}$$

In finite deformation, the measure of stress and the measure of strain have to be conjugate: several pairs can be found within the continuum theory but, for the purpose of this work, only two pairs are presented.
In reference configuration, the pair used is composed by the Euler Lagrange strain tensor $\boldsymbol{E}$ and 2nd Piola Kirchhoff stress tensor $\boldsymbol{S}$; in spatial configuration, instead, the Almansi strain tensor $\boldsymbol{e}$ and the Cauchy stress tensor $\boldsymbol{\sigma}$ are considered. In Voigt

notation, and introducing the measures described, Equation (2.5) and (2.6) become

$$S_{IJ} = \mathbb{C}_{IJHK} E_{HK} \tag{2.7}$$

$$E_{HK} = \mathbb{S}_{HKIJ} S_{IJ} \tag{2.8}$$

$$\sigma_{ij} = \mathbb{C}_{ijhk} e_{hk} \tag{2.9}$$

$$e_{hk} = \mathbb{S}_{hkij} \sigma_{ij} \tag{2.10}$$

where capital indices refer to reference configuration and small indices to spatial one. Using the push - forward operation, measures in spatial configuration can be derived from the measures in reference configuration, according with the following relations:

$$\boldsymbol{\sigma} = \frac{1}{J} \boldsymbol{F S F^T} \tag{2.11}$$

$$\boldsymbol{e} = \boldsymbol{F^{-T} E F^{-1}} \tag{2.12}$$

where J is the Jacobian of the transformation and $\boldsymbol{F}$ is the deformation gradient tensor. Equivalently, the opposite relation of pull - back operation is valid. From the strain measures, the right Cauchy Green deformation tensor $\boldsymbol{C}$ and the left Cauchy Green deformation tensor $\boldsymbol{b}$ can be derived

$$\boldsymbol{C} = 2\boldsymbol{E} - \boldsymbol{I} \tag{2.13}$$

$$\boldsymbol{b} = \boldsymbol{I} - 2\boldsymbol{e} \tag{2.14}$$

where $\boldsymbol{I}$ is the identity tensor.

Regarding Equations (2.5) and (2.6), symmetries can be found: without describing the theoretical bases, an elastic material can be described up to a maximum of 36 independent constants. However, it is general accepted that the most general form of anisotropy can be composed using 21 constants (when the further hypothesis of the existence of a strain energy function is considered). An orthotropic material is a material with three planes of symmetry and it is described by 9 constants; a transversely isotropic material is described using 5 constants and an isotropic material by 2. The hypothesis of transversely isotropy assumes a material with an axial symmetry: it is isotropic in a plane whereas the behavior is different in the perpendicular direction.

Recalling back the one dimensional description of viscoelasticity, instead, the generalizations of Equations (2.3) and (2.4) in spatial configuration are derived by the use of convolution integrals as follow

$$\sigma_{ij}(x,t) = \int_{-\infty}^{t} G_{ijhk}(x, t-\tau) \frac{\partial e_{hk}}{\partial \tau}(x,\tau) d\tau \tag{2.15}$$

$$e_{ij}(x,t) = \int_{-\infty}^{t} J_{ijhk}(x, t-\tau) \frac{\partial \sigma_{hk}}{\partial \tau}(x,\tau) d\tau \tag{2.16}$$

where the function G_{ijhk} is the tensorial relaxation function and J_{ijhk} is the tensorial creep function. It is worth to be noted that Equations (2.15) and (2.16) are within the framework of linear viscoelasticity modeling.

A further improvements on viscoelasticity is the so - called *quasi linear viscoelasticity*, in which the relaxation (or creep) function is also dependent by the loading rate but not by the time constants (Provenzano, Lakes, Keenan, & Vanderby, 2001). It is worth to be noted that no spatial derivatives are present in the viscoelastic theory: thus, no spatial dependences are taken into account.

Poroelasticity is the properties of a material composed by a porous elastic skeleton in which the pores are filled by a viscous fluid that can flow as response of an applied pressure gradient. Mathematically, gradient introduces spatial dependence.

Two different approaches can be used for the analysis of a soft hydrated tissue: the mixture model and the poroelastic model. According to the description of Cowin (Cowin & Cardoso, 2012) a mixture is a material with two or more ingredients, the particles of which are separable, independent and uncompounded with each other; if the distinct phases of a mixture retain their identity, the mixture is immiscible. In a poroelastic approach, instead, the tissue is considered as a composite material in which the solid and the fluid phases interact to define an homogeneous material with properties that are a weight average of the particular properties of the single phases: the deformation of the medium influences the flow of the fluid and vice versa.

Finally, a poroviscoelastic material can be described as a material in which a porous viscoelastic matrix is filled by a viscous fluid.

2.2 GENERAL ASPECTS ON EXPERIMENTAL TESTING

For the sake of clarity, the brief description of the possible experimental approaches that can fit the needs requested in testing the AC are presented through the suggested classification: experiments at macroscale, experiments at microscale, experiments at nanoscale, imaging and histology. In particular, the last group identifies all the approaches with which the information about the structure and the composition can be extracted, whereas the first three groups collect the approaches addressed to the extraction of mechanical parameters.

2.2.1 Macroscale

In a *confined compression test*, a cylindrical sample is inserted into a rigid confined chamber; the load (or, vice versa, the displacement) is applied along the axial direction by the movement of the upper surface of the chamber, whereas the radial displacement is forbidden. Alternatively, the upper or the lower surfaces are permeable: the permeability of the filter is orders of magnitude higher than the

tissue's one to not affect the measure. One of the most critical aspect of a confined test is to ensure the proper connection between the piston and the wall: it should be enough close to avoid fluid flow but the effect of the friction should be minimal. The setup for an *unconfined compression test* looks similar to the one for confined compression test except for the fact that the sample is not constrained in radial direction, avoiding the problems related to the proper sizing of the chamber. In Figure 2.2 both the presented setups are sketched. The work of Armstrong (Armstrong, Lai, & Mow, 1984) first proposes this two types of test for AC.

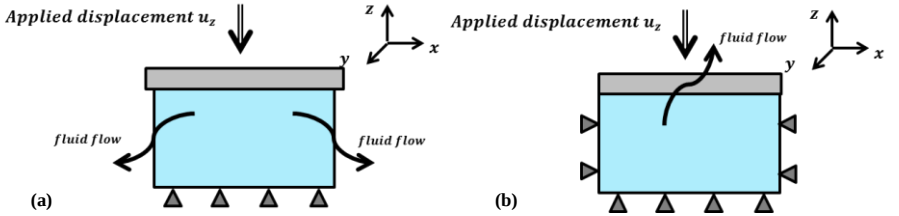

Figure 2.2: Sketches for the experimental setups in (a) unconfined compression test and (b) confined compression test.

In the case of *indentation test*, an indenter of a particular shape (typically a flat punch indenter or a spherical indenter at macroscale) is pressed into the sample to reach a prescribed indentation depth. The contact area is, in this case, smaller than the top surface of the sample: hence, the pattern of the fluid flow can be more complex as well as the solicitation is no more uniaxial. The choice of the geometrical parameters (shape and dimensions of the tip or indentation depth) allows to investigate the tissue under different lengths. In particular, when both the dimensions of the tip and the depths investigated decrease up to hundreds of micrometer and lower, this technique acquires the name of *nanoindentation*: since this methodology is the core of this work, it will be deeply discussed in the next Chapter.

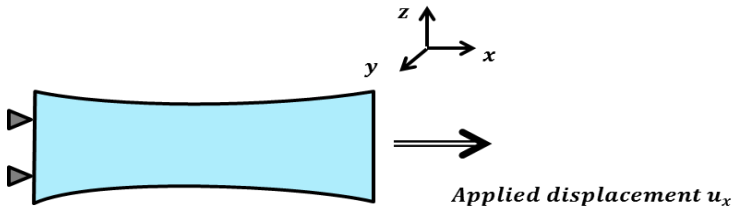

Figure 2.3: Sketch for the experimental setup in a tensile test.

Even if cartilage is optimized to sustain compressive load, *tension tests* (Figure 2.3) are mainly used to investigate the behavior of collagen network; the idea is to extract

samples with the shape of a strip and to apply a tensile load. Due to the anisotropic pattern of AC and its depth dependent organization, the testing direction and the site of extraction are important in interpreting the results.
Shear properties can be investigated through *simple shear tests* or *torsion tests* (Figure 2.4). In a simple shear test, the sample is confined in between two plates whereas the lateral surface is kept free. To ensure the friction between plate and surface a certain amount of pre-compression is applied: then, the plates are moved along the same direction but in opposite ways. In a torsion test, instead, the same configuration is used but a torque (or, vice versa, an angular displacement) is applied.

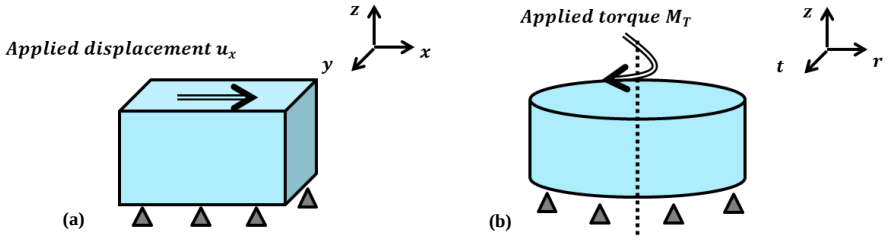

Figure 2.4 Sketch for the experimental setup in (a) shear test and (b) torsion test.

The main disadvantage of the tests at macroscale is that the experimental setup can significantly affect the results through misalignments, non - ideal contact conditions and boundary effects which can result in a underestimation or overestimation of the tissue properties (Korhonen, et al., 2002). However, they are capable to describe the global behavior of the tissue.

2.2.2 Microscale and Nanoscale

Tests at microscale or nanoscale, indeed, have two advantages than tests at macroscale: first, they are not sensitive to the specimen preparation since the conditions far from the site of probing do not affect the measure; second, the geometrical dimensions of the experiments can be of the same order of the microstructures or the macromolecules themselves, allowing their investigation. Low scales refer not only to a spatial condition, i.e. the displacements applied, but also to the range of forces applied: Han (Han, Grodzinsky, & Ortiz, 2011) suggests $[1\ nm - 100\mu m]$ for spatial lengths and $[tens\ of\ pN - N]$ for forces in these kinds of tests. Nanoindentation is the preferred technique used at these scales but also microtensile tests have now a growing interest.
One more interesting test is the indentation with the use of a functionalized tip that can stress selected single fibrils or macromolecules and their *in situ* resistance to

tension or compression can be studied (Han, Grodzinsky, & Ortiz, 2011).
Creep tests and stress relaxation tests in time domain and dynamic mechanical tests in frequency domain are possible upgrades of all the previously described quasi - static tests: indeed, they allow to study the time dependent properties. As one of the key points of this thesis, they will be discussed in Chapter 3.

2.2.3 Imaging and Histology

The techniques present under this Section do not provide the identification of any mechanical parameter. Nevertheless, since the increasing interest on the characterization of specific areas in AC, they can be used to obtain accurate spatial compositional description of the zone under investigation, looking for positive correlations among mechanical parameters and structures.
Imaging processes are used to recreated a bidimensional or tridmensional image of a slice or a volume of tissue. Several methods have been already presented and applied on articular cartilage, both destructive and non - destructive: quantitative polarized light microscopy (Massoumian, Juskaitis, Neil, & Wilson, 2003), multiphoton microscopy (Lilledahl, Pierce, Ricken, Holzapfel, & de Lange Davies, 2011), magnetic resonance imaging (Jazrawi, Alaia, Chang, Fitzgerald, & Recht, 2011), X-ray diffraction (Mollenhauer, et al., 2002) and ultrasounds (Nieminen, et al., 2002).
An histology, instead, is the study of microscopic anatomy of the tissue. By the use of specific chemical reagents, it is possible to deprive the tissue of particular constituents and to infer on the maintained characteristics; the modified Mankin score (Bobinac, Spanjol, Zoricic, & Maric, 2003) is one of the preferred methods to conduct an histology: a sample is treated in different ways and its consequent aspect is judged by a selection of blind observers; the results from each observer is averaged to obtain the global response, giving a subjective point of view of the situation. Doing this process locally, it is possible to have an accurate tissue mapping.

2.3 APPLICATIONS ON ARTICULAR CARTILAGE MODELING AND EXPERIMENTAL TESTING

Once the elastic, the viscous and the porous aspects are presented in a very general framework as well as the possible experimental approaches for the extraction of material properties, a brief explanation on how these general models are applied or, at least, are suitable for the description of AC is now presented and the results in literature are shown. AC properties have an high variability even when the experimental conditions are the same; the specie of animal from which the sample is

extracted is an information not to be neglected. Moreover, independently of the length scale under analysis, the parameters looked for are the same: elastic properties, viscous properties, permeability and friction properties are the most important. One of the most interesting aspect is, indeed, that these parameters have to be discussed within the particular scale under investigation: a comparison among scales has to be proposed and discussed very carefully because of the complex organization described in Chapter 1.

The first attempt to model AC is done assuming a monophasic, linear elastic, isotropic and homogeneous material; the work of Elmore (Elmore, Skoloff, Norris, & Carmeci, 1963) first suggests the concept of *imperfect elasticity* in behavior of AC when submerged in saline solution: AC can recover its thickness after the removal of compressive load. Hayes and Mockros (Hayes & Mockros, 1971) introduce the viscoelasticity through a generalized Kelvin model (a series of Kelvin models), without accounting for the role of fluid phase: they analyze the shear and bulk creep compliances of human articular cartilage under torsion and axial strain.
From its initial application in the field of geotechnics, the poroelastic behavior has been described in different ways, considering the pioneering work of Biot (Biot, 1941) till more advanced ones as, for example, the use of Green's function shown by Karpfinger (Karpfinger, Muller, & Gurevich, 2009). Terzaghi (Terzaghi, 1943) introduces the poroelastic model for soils, assuming that both the solid and fluid phases fill homogeneously the volume and Biot (Biot, 1955) extends it to a tridimensional anisotropic case; moreover, Rice and Clary (Rice & Cleary, 1976) provide analytical solution for linearized homogeneous poroelastic material with compressible solid and fluid phases, highlighting two limit conditions. The drained condition is the one in which the pressure is uniform throughout the sample and the load is completely sustained by the solid matrix. An undrained condition is, in general, a condition in which a pressure gradient is present but, the most important (the one that this work refers to), is the situation that describes the response to the limit of an instantaneous load. Higginson (Higginson, Litchfield, & Snaith, 1976) studies the effect of interstitial flow and concludes that instantaneous response in creep tests is purely elastic.
In the study of AC, two main poroelastic approaches can be found. The original work of Biot (Biot, 1941) accounts for the solid phase displacement, u, and the relative displacement between solid and fluid phases, w, ('$u-w$' model) as primary variables; improvements are suggested later as, for example, the work of Dazel (Dazel, Brouard, Depollier, & Griffiths, 2007) in which generalized coordinate are chosen in order to simplifying the derivation of the strain energy function. The mixed formulation is the one in which the primary variables are the solid phase

displacement, u, and the pore pressure, π ('$u-\pi$' model). Other recent general works on poroelasticity, suitable to be adapted in the description of AC, take into consideration finite strain and nonlinearity (Simon, 1992) or full dynamic formulations (Karpfinger, Muller, & Gurevich, 2009).

In a mixture model, the number and the type of primary variables are related to the real different species that compose the tissue and that one wants to consider. In the work of Mow (Mow, Kuei, Lai, & Armstrong, 1980) the biphasic mixture model considers the solid phase displacement, u, and the fluid phase displacement, U, ('$u-U$' model) as variables: the solid matrix is assumed intrinsically incompressible, linearly elastic and nondissipative and the fluid phase is intrinsically incompressible and nondissipative; viscous aspects are confined to the frictional drag between phases. Permeability is assumed constant. In the work of Lu (Lu, Wan, Guo, & Mow, 2010) the triphasic mixture model introduces also the effect of negative charged proteoglycans on fluid pressure: the governing equations are linearized and the proposed numerical implementation is valid for axisymmetric problems. Within the biphasic theory, a more realistic model for the solid phase is proposed by Almeida (Almeida & Spilker, 1998), where a transversely isotropy material is considered in a finite element framework.

As already stated by Rice (Rice & Cleary, 1976) in 1976, numerical approaches are required when inhomogeneities and complex geometries become inavoidable; indeed, analytical solutions are limited to few areas. Regarding viscoelasticity, for example, Vandamme (Vandamme & Ulm, 2006) proposes the solutions for axisymmetric indentations of isotropic, transversely isotropic and orthotropic viscoelastic material. Regarding poroelasticity, instead, the solution of confined compression test on isotropic poroelastic materials can be found in the work of Biot (Biot, 1941) and revisited by Cowin (Cowin & Doty, 2006). The problem of compression of disks with anisotropic poroelasticity is solved analytically by Cowin (Cowin & Mehrabadi, 2007).

A wide range of numerical models are present in literature, considering poroelasticity, viscoelasticity, anisotropy, non - linearity, fibers distribution and biochemical interactions. The emphasis on the constituent - based models is recently considered, introducing explicitly the contributions of the collagen network to the AC mechanics, through distribution functions for collagen fibrils orientations as in Shirazi (Shirazi, Vena, Sah, & Klisch, 2011), or the effect of the large deformations on parameters, as proposed by Ateshian (Ateshian & Weiss, 2010) for permeability. In his recent work, Seifzadeh (Seifzadeh, Wang, Ouguamanam, & Papini, 2011) presents porohyperviscoelastic model for articular cartilage that considers fibers reorientation, validated through a comparison with the indentation data presented by DiSilvestro (DiSilvestro & Suh, 2001). In this model, the matrix is modeled using

three terms in the Prony series, whereas the fibers distribution, in which the collagen fibers are able to sustain only tensile load, is borrowed by the works of Holzapfel (Holzapfel, Gasser, & Ogden, 2006), the numerical implementation of which is already embedded into the commercial finite element code Abaqus (Simulia, Providence, RI, USA). The permeability is modeled as strain dependent, but no contribution of PGs is considered. In the work of Ateshian (Ateshian, Rajan, Chahine, Canal, & Hung, 2009) the focus is on the modeling of a continuous fibers distribution: this approach appears more powerful than the use of a discrete fibers distribution. Moreover, he introduces the effect due to the swelling of PGs and its link with the biochemical composition of the environment in which AC is submerged. Nor permeability neither viscous aspects are considered.

An interesting fibril reinforced model is proposed by Li (Li, Soulhat, Buschmann, & Shirazi-Adl, 1999): in this model, an incompressible elastic isotropic porous matrix is filled by incompressible fluid; the fibrillar part is distributed along the three principal directions of a cylindrical reference system. The stress - strain relation of the fibrillar network is modeled linear (and null in compression), whereas the permeability is exponentially decreasing with the deformation. No effect of PGs is taken into account. A theoretical analysis of a suitable fiber distribution is recently proposed by Federico (Federico & Gasser, 2010): the final expression of the probability density function is obtained by the superposition of a continuous infinity of fibers families; this approach is numerically evaluated looking at the consequent stress - deformation behavior. The approach proposed by Wilson (Wilson, van Donkelaar, van Rietbergen, & Cohen, 2005) appears more complete: it describes, indeed, a biphasic model in which the solid matrix consists of a swelling non-fibrillar part and a fibrillar part representing the collagen network. A total of 9 viscoelastic fibrils within each material point is modeled. Pierce (Pierce, Trobin, Trattnig, Bischf, & Holzapfel, 2009) adapts the model proposed by Holzapfel (Holzapfel, Gasser, & Ogden, 2006) using a discrete real fiber distribution extracted from the imaging method proposed by Lilledahl (Lilledahl, Pierce, Ricken, Holzapfel, & de Lange Davies, 2011). Details about the proposed discrete fibers distribution can also be found in a more recent work by Pierce (Pierce, et al., 2010).

The dichotomy between viscoelasticity and poroelasticity is a more recent topic. In 1963, Elmore (Elmore, Skoloff, Norris, & Carmeci, 1963) states that the response, in case of macroscopic indentation test, is primary due to the fluid exudation. Actually, it is accepted that the balance among the constitutive aspects and the geometrical parameters of the experiment affects articular cartilage behavior in different ways: in case of viscoelasticity, Huang (Huang, Mow, & Ateshian, 2001) shows that the response is independent from the characteristic length scale analyzed whereas, in case of poroelasticity, Hu (Hu, Zhao, Vlassak, & Suo, 2010) states that it is strictly

related to both the scale of the experiments and the properties of the sample and he proposes dimensionless relaxation functions for different geometries of indenter tip, extracted from experiments on elastomeric gels. Galli (Galli, Comley, Shean, & Oyen, 2009) uses the nanoindentation and microindentation techniques to characterize hydrogels in time domain as well as in frequency domain. In his paper, the time dependence induced by the extrinsic fluid flow mechanisms is discussed in view of the length scale effects found in indentation experiments carried out using different probe sizes. The effect of geometrical aspect ratios is investigated in the work of Lu (Lu, Wan, Guo, & Mow, 2010) using creep tests.

Confined compression stress relaxation tests are performed in the work of Schinagl (Schinagl, Gurskis, Chen, & Sah, 1997): 9 layers, $125\,\mu m$ thick each, plus the superficial ($1.125\,\mu m$) and the deepest ($250\,\mu m$) ones, are extracted from a cartilage sample and the stress relaxation test is performed over four subsequent levels of compression. By the use of a numerical best fit process, the results show that the equilibrium compressive modulus increases with the depth from $0.079 \pm 0.039\,MPa$ of the superficial to $1.14 \pm 0.44\,MPa$ of the deepest one, suggesting heterogeneous elastic properties. The *homogeneous modulus*, namely the equilibrium modulus computed with a full thickness sample is $0.38 \pm 0.12\,MPa$: hence, the lower modulus found in the superficial layer could be related to its peculiar function. An analogous work is proposed by Chen (Chen, Bae, Schinagl, & Sah, 2001) that performs oscillatory confined compression tests on both full - thickness ($\sim 2.5\,mm$) samples and sliced samples (three slices for each full - thickness one) of adult bovine AC. An homogeneous and a layered model is used to extract the zero strain equilibrium modulus, H_{A0}, and the strain dependent permeability, where k_{p0} is the zero strain permeability and k_{p1} is the deformation dependence constant. Results show that H_{A0} increases with the layers from $0.27\,MPa$ to $0.71\,MPa$ whereas the homogenous value is equal to $0.47\,MPa$, in between these two limits; k_{p0} decreases from $4.6x10^{-15}\frac{m^4}{Ns}$ to $0.5x10^{-15}\frac{m^4}{Ns}$, in both cases lower than the homogenous value, $7.3x10^{-15}\frac{m^4}{Ns}$; k_{p1} increases from 5.5 to 7.4, similar to the homogenous parameter, 8.4. The properties of the newborn bovine patellofemoral groove AC are studied by Flickling (Ficklin, et al., 2007) using confined compression, unconfined compression and torsional shear tests in order to evaluate the effect of the *in vitro* growth. Three groups of samples are extracted: medial - lateral, antero - posterior and axial, extracted at mean depth of $2\,mm$ from the surface and of an averaged thickness of $1\,mm$. Equilibrium modulus, both in confined and unconfined conditions, is independent from the direction of loading and the strain level with a value $\sim 0.5\,MPa$; it depends on the

Poisson's ratio, as expected due to anisotropy. Moreover, mechanical properties are found positively correlated with the GAGs concentration throughout the strain levels ($15\% - 30\% - 45\%$) and with COL only at the highest one.

A wide study on AC, from tension to compression, is given in the work of Chahine (Chahine, Wang, Hung, & Ateshian, 2004): he analyzes specimens extracted from the surface (strips, parallel and perpendicular to the split-line, and cylinders) or the deep zone by using unconfined compression tests, up to 20% of strain, and tensile tests, up to 7% of strain, in different bath conditions (hypotonic, isotonic, hypertonic). The compressive modulus is found nearly constant with the strain, independent by the direction in superficial specimens and increasing with the depth: $0.18 \pm 0.07\ MPa$ superficially and $0.35 \pm 0.11\ MPa$ for the deep zone. The tensile modulus, instead, is strongly strain dependent: it is found higher superficially and in samples extracted parallel to the split lines ($\sim 7\ MPa$). Both the parameters decrease with increasing ionic bath concentration. The results indicate that there is a smooth transition between tension and compression regimes and that AC shows a orthotropic symmetry within a tension - compression nonlinear behavior. In all the studies presented above, the specimens analyzed have a characteristic size of few millimeters (macroscale).

A comparison between compression tests, confined and unconfined, and indentation tests (in which both the pistons and the indenter tip are porous) can be found in the work of Korhonen (Korhonen, et al., 2002): the specimens are extracted from bovine AC. Spherical indenters tips have diameters of $1\ mm$ and $3\ mm$; in the confined compression the piston has a diameter of $3.7\ mm$ whereas the unconfined test are conducted with pistons of $3.7\ mm$ and $2.7\ mm$ in diameter. In terms of equilibrium modulus, slight differences can be found among the different sites analyzed on the same joint surface. The most interesting aspect is, however, that no differences are noted between confined and unconfined approaches whereas the modulus measured from indentation is higher and independent from tip size: as an example, in the humerus, $0.80 \pm 0.33\ MPa$ in unconfined test and using the large piston; $0.78 \pm 0.35\ MPa$ in unconfined test and using the small piston; $0.81 \pm 0.34\ MPa$ in confined; $1.15 \pm 0.44\ MPa$ in indentation. An averaged Poisson's ratio, measured optically ~ 0.17, is, instead, better approximated using compression tests than indentation tests.

The experimental results extracted by DiSilvestro (DiSilvestro & Suh, 2001) are interesting since the experimental protocol is such that the analyzed response falls into a linear region of the AC behavior. Therefore, these results can be used to validate linear models. From the patella of mature bovine joint he extracts plugs to be tested through confined compression, unconfined compression and indentation tests. The plugs are about $3\ mm$ in diameter; the indentation are performed using

flat punch tips of radii $1\,mm$ for the porous indenter and $1.5\,mm$ for the non-porous. In all the cases, the samples are pre-compressed of a 10% and loaded up to a further 5% at constant strain rate of $0.001\ 1/s$. A biphasic poroviscoelstic model is used to fit the data and the overall elastic response is found in terms of an elastic modulus $E = 0.63 \pm 0.18\,MPa$, a Poisson's ratio $\nu = 0.10 \pm 0.05$ and a permeability $k = 1.72 \pm 1.61x10^{-15}\frac{m^4}{Ns}$. Two main time constants are also proposed, describing a short term behavior, $\sim 0.60\,s$, and a long term one, $\sim 85\,s$.

The effect of geometrical aspects in material response has been emphasized by several authors, especially in time domain. Simha (Simha, Jin, Hall, Chiravarambath, & Lewis, 2007) performs indentation tests on bovine patellar cartilage using flat - ended conical or cylindrical tips with end diameters ranging from $5\,\mu m$ to $4\,mm$. Results show that the elastic modulus remains constant, around $0.8\,MPa$ if the tip size is greater than $2\,mm$ and increases when the tip size is smaller and smaller, up to the $2.5\,MPa$ in the case of the smallest tip analyzed. A similar trend is not found using an elastomer (urethane), justifying that this behavior is not an artifact of the instrumented test but a peculiar aspect of AC. Even if Simha suggests that the explanation can be found looking at the structure of AC, no precise reasons are proposed. Jin (Jin & Lewis, 2004) proposes a methods to extract elastic properties of AC by the use of stress relaxation spherical indentation tests with two different radii (of the order of mm): then, he suggests averaged values for the instantaneous Young's modulus and Poisson's ratio, $E_{t=0} \sim 2\,MPa$ and $\nu_{t=0} \sim 0.46$, and for the equilibrium condition, $E_{t=\infty} \sim 0.5\,MPa$ and $\nu_{t=0} \sim 0.33$.

Nanoindentation can be used to characterize *in situ* AC properties at tissues scale; this statement is justified, for example, by the work of Li (Li, Pruitt, & King, 2006) where the technique is applied to normal rabbit metacharpophalangeal joint: the resistance of penetration and the volumetric creep strain are chosen as mechanical parameters to be compared with the morphological quantities like thickness and cell density. The investigation is performed using a conospherical diamond tip of $100\,\mu m$ radius of curvature and up to a load of $200\,\mu N$. Loparic (Loparic, et al., 2010) uses microindentation and nanoindentation tests to probe different structures on femoral head of porcine hip. Two tips are used: a spherical one with radius $10\,\mu m$ and a pyramidal one with nominal tip radius $< 20\,nm$; the maximum load is, respectively, $\sim 2\,\mu N$ and $\sim 1.8\,nN$. Results show how the averaged stiffness measured with the larger tip is almost constant through the surface and equal to $1.3 \pm 0.4\,MPa$, whereas two different values can be found with the smaller, $\sim 22.3\,kPa$ related to PGs and $\sim 384\,kPa$ related to COL. In the work of Stolz (Stolz, et al., 2009), the procedure presented above is used to investigate the effect of the aging process in mice articular cartilage.

An overview of the application of dynamical mechanical analysis (DMA) to biological samples is reported in the work of Franke (Franke, Goken, & Hodge, 2008). Fulcher (Fulcher, Hukins, & Shepherd, 2009) analyzes specimens from medial and lateral tibial plateau of adult bovine knee by the use of a flat punch indenter of $5.3\,mm$ in diameter; the samples are solicited with a sinuosoidal stimulus between $16\,N$ and $32\,N$ in the frequency range $[1-92]\,Hz$. The measured storage modulus increases with frequency till a plateau of about $60-90\,MPa$ at the highest frequencies. Loss modulus appears fairly constant whereas the phase shift is in the range $[3.4^o-5.7^o]$. Authors suggest viscoelasticity as explanation of this behavior. Huang (Huang, Wang, & Lu, 2005) proposes solution for viscoelastic behavior of polymers under dynamic spherical indentation tests.

The application of nanoindentation technique coupled with dynamic mechanical tests on the analysis of AC is shown in Han (Han, Grodzinsky, & Ortiz, 2011): fluid flow induced poroelasticity is shown to primarily govern the frequency dependent energy dissipation, while longer time scale relaxation mainly reflects viscoelasticity. At microscale, indeed, dynamic modulus is linear with the square of the frequency, consistent with a poroelastic phenomenon. Native and PG - depleted AC from young bovine is tested using both classical and dynamic (up to $316\,Hz$) AFM - based nanoindentation test; two tips are used: a pyramidal one with end radius $\sim 50\,nm$ and half angle 35^o and a spherical one of radius $\sim 2.5\,\mu m$. In the classical indentation, the maximum displacement applied is $2\,\mu m$ corresponding to a maximum load of $8.5\,nN$; the dynamic tests on native cartilage are performed at an offset depth of $0.43\pm0.04\,\mu m$ for the spherical tip and $1.01\pm0.06\,\mu m$ for the pyramidal while, on PG - depleted samples, the offset depths are $0.77\pm0.04\,\mu m$ and $1.37\pm0.12\,\mu m$, respectively. Results evidence no differences between tips: the characteristic lengths investigated are, in fact, equal. Indentation modulus is $0.10\pm0.01\,MPa$ for the native AC and decreases of 70% for the treated one. Storage modulus and dissipative modulus increase with the frequency: the magnitude of complex modulus increases from $0.22\pm0.02\,MPa$ at $1\,Hz$ to $0.77\pm0.10\,MPa$ at $316\,Hz$; PG - depleted AC shows lower dynamic and storage moduli whereas the dissipative behavior is comparable with the native one. A numerical model for the proposed experiments is shown by Nia (Nia, Han, Li, Ortiz, & Grodzinsky, 2011); the tissue is modeled as a fiber reinforced poroelastic material and the problem is solved in time domain. The storage modulus at zero frequency, the storage modulus at high frequency and the frequency of the peak are investigated; a sensitivity analysis is performed over the indentation depth parameter, using the isotropic case as reference.

In Table 2.1, representative results of the references presented above are summarized; they all refer to bovine articular cartilage. When required in the single Chapters, other references will be provided to directly address their specific questions.

Table 2.1: Relevant literature data on bovine AC.

REFERENCE	EXPERIMENT	LENGTH	RESULT
(Schinagl, Gurskis, Chen, & Sah, 1997)	Confined compression	mm	Young Bovine AC Elastic modulus from $0.079 \pm 0.039\ MPa$ to $1.14 \pm 0.44\ MPa$, from surface to deepest layer
(Chen, Bae, Schinagl, & Sah, 2001)	Oscillatory confined compression	mm	Young Bovine AC Superficial layer. Elastic modulus $0.27\ MPa$ and strain dependent permeability $k(\varepsilon) = 4.6x10^{=15} e^{-5.5\varepsilon}$
(Ficklin, et al., 2007)	Confined compression Unconfined compression Torsional test	mm	Newborn Bovine AC Equilibrium modulus of $0.5\ MPa$ independent by the zone; Poisson's ratios equals to 0.25 out of plane and 0.15 in plane
(Chahine, Wang, Hung, & Ateshian, 2004)	Unconfined compression Tensile	mm	Young Bovine AC Compressive modulus of surface $0.18 \pm 0.07\ MPa$; Tensile modulus $\sim 7MPa$
(Korhonen, et al., 2002)	Confined compression Unconfined compression Indentation	mm	Young Bovine AC No differences between confined and unconfined tests whereas modulus from indentation is higher and independent from tip size
(DiSilvestro & Suh, 2001)	Confined compression Unconfined compression Indentation	mm	Mature Bovine AC From identification based on a biphasic model, elastic modulus $0.63 \pm 0.18\ MPa$, Poisson ratio 0.10 ± 0.05, permeability $k = 1.72 \pm 1.61x10^{-15} \frac{m^4}{Ns}$
(Simha, et al. 2007)	Indentation	$5\ \mu m$ to $4\ mm$ in diameter	Bovine AC Elastic modulus constant, $\sim 0.8\ MPa$ for tip diameter greater than $2\ mm$; it increases up to the $2.5\ MPa$ in the case of the smallest tip
(Jin & Lewis, 2004)	Stress relaxation Indentation	mm (different sizes)	Mature Bovine AC Instantaneous Young's modulus $\sim 2\ MPa$ and Poisson's ratio ~ 0.4;equilibrium Young's modulus $\sim 0.5\ MPa$ and Poisson's ratio ~ 0.33

REFERENCE	EXPERIMENT	LENGTH	RESULT
(Fulcher, Hukins, & Shepherd, 2009)	Dynamic Indentation	mm	Mature Bovine AC Storage modulus increases up to $60 - 90\ MPa$ in the range $[1 - 92]\ Hz$. Fairly constant dissipative modulus Viscoelasticity
(Han, et al., 2011)	Dynamic Nanoindentation	$\sim 1.5\ \mu m$	Young Bovine AC Magnitude of complex modulus increases from $0.22 \pm 0.02\ MPa$ at $1\ Hz$ to $0.77 \pm 0.10\ MPa$ at $316\ Hz$. PGs depleted samples shows lower (up to 70%) values Poroelasticity

To relate the response of experimental tests, indentation in particular, to mechanical properties still remain a challenge for fluid filled tissues or materials; under these circumstances, indeed, the response is both time dependent and size dependent. The investigation of micrometric and nanometric scales as well as the application of dynamic tests or time domain tests with different probing tips appear unexplored possibilities. These considerations highlight also the need for models to interpret the experimental results of instrumented indentation on soft tissues exhibiting a poroelastic or poroviscoelastic mechanical response.

REFERENCES

Almeida, E., & Spilker, R. (1998). Finite element formulations for hyperelastic transversely isotropic biphasic soft tissues. *Computer Methods in Applied Mechanics and Engineering, 151*, 513-538.

Armstrong, C., Lai, V., & Mow, V. (1984). An analysis of the unconfined compression of articular cartilage. *Journal of Biomedical Engineering, 106*, 165-173.

Ateshian, G., & Weiss, J. (2010). Anisotropic hydraulic permeability under finite deformation. *Journal of Biomechanical Engineering, 132*.

Ateshian, G., Rajan, V., Chahine, N., Canal, C., & Hung, C. (2009). Modeling the matrix of articular cartilage using a continuous fiber angular distribution predicts many observed phenomena. *Journal of Biomechanical Engineering, 131*, 061003-1:10.

Bao, G., & Suresh, S. (2003). Cell and molecular mechanics of biological materials. *Nature Materials*, 715-725.

Biot, M. (1941). General theory of three dimensional consolidation. *Journal of Applied Physics, 12*, 155-164.

Biot, M. (1955). Theory of elasticity and consolidation for a porous anisotropic solid. *Journal of Applied Physics, 26*(2), 182-185.

Bobinac, D., Spanjol, J., Zoricic, S., & Maric, I. (2003). Changes in articular cartilage and subchondral bone histomorphometry in osteoarthritic knee joints in humans. *Bone, 32*, 284-290.

Chahine, N., Wang, C., Hung, C., & Ateshian, G. (2004). Anisotropic strain-dependent material properties of bovine articular cartilage in the transitional range from tension to compression. *Journal of Biomechanics, 37*(8), 1251-61.

Chen, A., Bae, W., Schinagl, R., & Sah, R. (2001). Depth- and strain-dependendent mechanical and electromechanical properties of full-thickness bovine articular cartilage in confined compression. *Journal of Biomechanics, 34*(1), 1-12.

Cowin, S., & Cardoso, L. (2012). Mixture theory-based poroelasticity as a model of interstitial tissue growth. *Mechanics of Materials, 44*, 47-57.

Cowin, S., & Doty, S. (2006). *Tissue Mechanics.* New York: Springer Verlag.

Cowin, S., & Mehrabadi, M. (2007). Compressible and incompressible constituents in anisotropic poroelasticity: The problem of unconfined compression of a disk. *Journal of the Mechanical and Physics of Solids, 55*(1), 161-193.

Dazel, O., Brouard, B., Depollier, C., & Griffiths, S. (2007). An alternative Biot's displacement formulation for porous materials. *Acustical Society of America, 121*(6), 3509-3516.

DiSilvestro, M., & Suh, J. (2001). A cross-validation of the biphasic poroviscoelastic model of articular cartilage in unconfined compression, indentation and confined compression. *Journal of Biomechanics, 34*, 519-525.

Elmore, S., Skoloff, L., Norris, G., & Carmeci, P. (1963). Nature of "imperfect" elasticity of articular cartialge. *Journal of Applied Physiology, 18*(2), 393-396.

Federico, S., & Gasser, T. (2010). Nonlinear elasticity of biological tissues wth statistical fibre orientation. *Journal of the Royal Society Interface, 7*, 955-966.

Ficklin, T., Thomas, G., Barthel, J., Thonar, E., Masuda, K., Asanbaeva, A., . . . Klish, S. (2007). Articular cartilage mechanical and biochemical property relations before and after in vitro growth. *Journal of Biomechanics*, 3607-3614.

Franke, O., Goken, M., & Hodge, A. (2008). The nanoindentation of soft tissue: current and developing approaches. *Journal of the Minerals Metals & Materials Society, 60*, 49-53.

Fulcher, G., Hukins, D., & Shepherd, D. (2009). Viscoelastic properties of bovine articular cartilage attached to subchondral bone at high frequency. *BMC Musculoskeletal Disorders, 7*, 1-7.

Fung, Y. (1965). *Foundations of Solid Mechanics.* Englewood Cliffs, New Jersey: Prentice-Hall Inc.

Galli, M., Comley, K., Shean, T., & Oyen, M. (2009). Viscoelastic and poroelastic mechanical characterization of hydrated gels. *Journal of Materials Research, 24*(3), 973-979.

Han, L., Frank, E., Greene, J., Lee, H., Hung, H., Grodzinsky, A., & Ortiz, C. (2011). Time-Dependent Nanomechanics of Cartilage. *Biophysical Journal, 100*, 1846-1854.

Han, L., Grodzinsky, A., & Ortiz, C. (2011). Nanomechanics of the cartilage extracellular matrix. *Annual Review of Material Research, 41*, 133-168.

Hayes, W., & Mockros, L. (1971). Viscoelastic properties of human articular cartilage. *Journal of Applied Physiology, 31*(4), 562-568.

Higginson, G., Litchfield, M., & Snaith, J. (1976). Load-displacement-time characteristics of articularr cartilage. *International Journal of Mechanical Sciences, 18*(9), 481-486.

Holzapfel, G., Gasser, T., & Ogden, R. (2006). A new constitutive framework for arterial wall mechanics and a comparative study of material models. *Journal of Elasticity, 61*, 1-48.

Hu, Y., Zhao, X., Vlassak, J., & Suo, Z. (2010). Using indentation to characterize the poroelasticity of gels. *Applied Physics and Letters, 96*, 121904-1:3.

Huang, C., Mow, V., & Ateshian, G. (2001). The role of flow independent viscoelasticity in the biphasic tensile and compressive responses of articula cartilage. *Journal of Biomechanical Engineering, 123*(5), 410-418.

Huang, G., Wang, B., & Lu, H. (2005). Measurements of viscoelastic functions of polymers in the frequency domain using nanoindentation. *Mechanics of Time-Dependent Materials, 8*, 345-364.

Jazrawi, L., Alaia, M., Chang, G., Fitzgerald, E., & Recht, M. (2011). Advances in magnetic resonance imaging of articular cartilage. *Journal of American Academy of Orthopaedic and Surgery, 19*(7), 420-429.

Jin, H., & Lewis, J. (2004). Determination of Poisson's ratio of articular cartilgae by indentation using different-sized indenters. *Journal of Biomechanical Engineering, 126*(2), 138-145.

Karpfinger, F., Muller, T., & Gurevich, B. (2009). Green's functions and radiation patterns in poroelastic solid revisited. *Geophysical Journal Internaitional, 178*, 327-337.

Karpfinger, F., Muller, T., & Gurevich, B. (2009). Green's functions and radiation patterns in poroelastic solids revisited. *Geophysical Journal International, 178*, 327-337.

Korhonen, R., Laasanen, M., Toyras, J., Rieppo, J., Hirvonen, J., Helminen, H., & Jurvelin, J. (2002). Comparison of the equilibrium response of articular cartilage in unconfined compression, confined compression and indentation. *Journal of Biomechanics, 35*, 903-909.

Li, C., Pruitt, L., & King, K. (2006). Nanoindentation differentiates tissue-scale fuctional properties of native articular cartilage. *Journal of Biomedical Material Research Part A, 78A*(4), 729-758.

Li, L., Soulhat, J., Buschmann, M., & Shirazi-Adl, A. (1999). Nonlinear analysis of cartilage in unconfined ramp compression using a fibril reinforced poroelastic model. *Clinical Biomechanics, 14*, 673-682.

Lilledahl, M., Pierce, D., Ricken, T., Holzapfel, G., & de Lange Davies, C. (2011). Structural analysis of articular cartilage using multiphoton microscopy: input for biomechanical modeling. *IEEE Transactions on Medical Imaging, 30*(9), 1635-1648.

Loparic, M., Wirtz, D., Daniels, A., Raiteri, R., vanLandingham, M., Guex, G., . . . Stolz, M. (2010). Micro- and nanomechanical analysis of articular cartilage by indentation-type atomic force microscopy: validation with a gel-microfiber composite. *Biophysical Journal, 98*, 2731-2740.

Lu, X., Wan, L., Guo, X., & Mow, V. (2010). A linearized formulation of triphasic mixture theory for articular cartilage and its application to indentation analysis. *Journal of Biomechanics, 43*(4), 673-679.

Massoumian, F., Juskaitis, R., Neil, M., & Wilson, T. (2003). Quantitative polarized light microscopy. *Journal of Microscopy, 209*, 12-22.

Mollenhauer, J., Aurich, M., Zhong, Z., Muehleman, C., Cole, A., Hasnah, M., . . . Chapman, L. (2002). Diffraction-enhanced X-ray imaging of articular cartilage. *Osteoarthritis and Cartilage, 10*(3), 163-171.

Mow, V., Kuei, S., Lai, W., & Armstrong, C. (1980). Biphasic creep and stress relaxation of articular cartilage in compression - theory and experiment. *Journal of Biomechanical Engineering, 102*, 73-84.

Nia, H., Han, L., Li, Y., Ortiz, C., & Grodzinsky, A. (2011). Poroelasticity of cartilage at the nanoscale. *Biophysical Journal, 101*, 2304-2313.

Nieminen, H., Toyras, J., Rieppo, J., Neiminen, M., Hirvonen, J., Korhonen, R., & Jurvelin, J. (2002). Real-time ultrasound analysis of articular cartilage degradation in vitro. *Ultrasound in Medicine & Biology, 28*(4), 519-525.

Pierce, D., Trobin, W., Raya, J., Trattnig, S., Bischof, H., Glaser, C., & Holzapfel, G. (2010). DT-MRI based computation of collagen fiber deformation in human articular cartilage: a feasibility study. *Annals of Biomedical Engineering*, 2447-2463.

Pierce, D., Trobin, W., Trattnig, S., Bischf, H., & Holzapfel, G. (2009). A phenomenological approach toward patient-specific computational modeling of articular cartilage including collagen fiber tracking. *Journal of Biomechanical Engineering, 131*, 091006-1:12.

Provenzano, P., Lakes, R., Keenan, T., & Vanderby, R. (2001). Nonlinear ligament viscoelasticity. *Annals of Biomedical Engineering, 29*(10), 908-914.

Rice, J., & Cleary, M. (1976). Some basic stress diffusion solution for fluid-saturated elastic porous media with compressible constituents. *Review on Geophysics and Space Physics, 14*, 227-241.

Schinagl, R., Gurskis, D., Chen, A., & Sah, R. (1997). Depth-dependent confined compression modulus of full thickness bovine articular cartilage. *Journal of Orthopaedic Research, 15*(4), 499-506.

Seifzadeh, A., Wang, J., Ouguamanam, D., & Papini, M. (2011). A nonlinear biphasic fiber-reinforced porohyperviscoelastic model of articular cartilage incorporating fiber reorientation and dispersion. *Journal of Biomechanical Engineering, 133*, 081004-1:8.

Shirazi, R., Vena, P., Sah, R., & Klisch, S. (2011). Modeling the collagen fibril network of biological tissues as a nonlinear elastic material using a continuous volume fraction distribution function. *Mathematics and Mechanics of Solids, 16*, 706-715.

Simha, N., Jin, H., Hall, M., Chiravarambath, S., & Lewis, J. (2007). Effect of indenter size on elastic modulus of cartilage measured by indentation. *Journal of Biomechanical Engineering, 129*, 767-775.

Simon, B. (1992). Multiphase poroelastic finite element models for soft tissue structures. *Applied Mechanics Reviews, 45*, 191-218.

Stolz, M., Gottardi, R., Raiteri, R., Miot, S., Martin, I., Imer, R., . . . Aebi, U. (2009). Early detection of aging cartilage and osteoarthritis in mice and patient samples using atomic force microscopy. *Nature Nanotechnology, 4*, 186-192.

Vandamme, M., & Ulm, F. (2006). Viscoelastic solution for conical indentation. *International journal of Solid and Structures, 43*, 3142-3165.

Wilson, W., van Donkelaar, C., van Rietbergen, B., & Cohen, I. (2005). A fibril reinforced porovisceolastic swelling model for articular cartilage. *Journal of Biomechanics, 1195-1204*, 38.

Wu, M. (2011). Strategies and challenges for the mechanical modeling of biological and bio-inspired materials. *Materials Science and Engineering: C, 31*(6), 1209-1220.

Chapter 2. Models and Experimental Tests in Literature

Chapter 3. Methods: Nanoindentation Test

In this Chapter the relevant aspects of the procedures based on the nanoindentation technique are shown. In Section 3.1, the theoretical basis of contact mechanics applied to nanoindentation tests are presented. In Section 3.2, two particular instruments, the Atomic Force Microscope and the Nanoindenter, are described. Section 3.3 describes the experiments used to investigate time dependent properties: creep tests and stress relaxation tests in time domain and dynamic tests in frequency domain. In Section 3.4, experimental problems addressed in this thesis are cleared up as well as the solutions adopted. Section 3.5 contains a brief description of samples preparation.

Chapter 3.
Methods: Nanoindentation Test

An indentation test consists on the penetration of a tip, which can have different shapes and different sizes, into the surface of a sample until a prescribed depth or overall load is achieved; during the whole procedure, indentation depth and reaction force are recorded.
Varying the geometry of the tip and the indentation depth reached, this technique allows to study a material at different characteristic lengths. Then, if the class of indentation tests covers a wide range of dimensions, each of them related to the particular application, nanoindentation is particularly focused to the investigation at lengths ranging from hundreds of micrometers to nanometers. Comparing this technique with the classical experimental tests at macroscale (as briefly discussed in Chapter 2), nanoindentation has shown its capability to be non-destructive and insensitive to the boundary conditions of the sample: this means that the properties recorded are not affected by the preparation of the sample and its possible, consequent, damage. This experimental technique represents an effective tool which is capable of probing local gradients and heterogeneities, as well as to drive diverse deformation modes by changing indenter tip geometry, loading conditions and experimental time scales (Oyen & Cook, 2009).

3.1 CONTACT MECHANICS AND THEORY OF INDENTATION

In order to investigate the properties of a material using the indentation technique, the initial step is the understanding the basis of contact mechanics.
Contact mechanics is the study of the deformation of solids that are in contact in one or more points (Johnson, 1985). The starting approach is presented in the paper of Hertz (Hertz, 1882), in which he explains the behavior of two purely elastic spheres in contact (but the theory can be easily generalized to the contact between an elastic sphere and an infinite elastic half - plane). Two *conforming surfaces* belong to bodies that *fit* closely together without deformations; otherwise, the surfaces are *non - conforming* and the contact is limited to a smaller area where the stress field is highly concentrated and independent by the conditions (geometry and boundary) far from the contact point. Mathematically, this last condition directly derives from the simplification suggested by Hertz, for which the two bodies can be considered as purely elastic and their contact describes an elliptical region of plane surface: as a consequence, the significant dimension of contact area is small compared to both the dimensions of each body and their radii of curvature. If far field conditions do not affect the contact behavior, the stress – strain field around contact falls in the theory of linear elasticity.

3.1.1 Contact between two spheres within the Herzian framework

Let us consider two elastic spheres of radii R_1 and R_2 and let us define a as the characteristic contact size (in the following, a will be regarded as contact radius);

the relative radius of curvature R is such that $\frac{1}{R} = \frac{1}{R_1} + \frac{1}{R_2}$ The problem is solved under the following hypothesis: (i) surfaces continuous and non - conforming, $a \ll R$; (ii) small strains, $a \ll R$; (iii) each solid is considered as an elastic half - space, $a \ll R_{1,2}, a \ll l$; (iv) frictionless surfaces. Parameter l is a measure of the macroscopic characteristic length of the bodies.

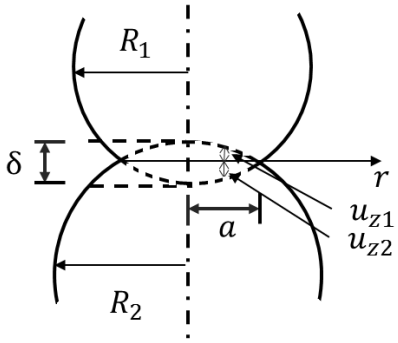

Figure 3.1: Contact between two spheres; the quantities used in this Section are presented.

When two isotropic bodies are brought in contact, the contact area is circular and its radius is $a = \frac{1}{2}\left(\frac{1}{R_1} + \frac{1}{R_2}\right)$. Omitting the whole mathematical formulation of the problem, the Hertzian solution computes the pressure distribution p and the normal displacement of the surface of the i - *th* body $u_{z,i}$ ($i \in [1,2]$) as a function of the radial coordinate r

$$p(r) = p_0 \left[1 - \left(\frac{r}{a}\right)^2\right]^{1/2} \tag{3.1}$$

$$u_{z,i}(r) = \frac{1-\nu_i^2}{E_i}\frac{\pi p_0}{4a}(2a^2 - r^2) \tag{3.2}$$

where p_0 is the maximum pressure applied and the pair (E_i, ν_i) defines the elastic properties of the i - *th* body, Young's modulus and Poisson's ratio, respectively. It can be established that the pressure distribution proposed in Equation (3.1) is the unique solution of the problem and does not allow any interaction between the two bodies outside the contact area. The expression of the mutual approach δ is

$$u_{z,1} + u_{z,2} = \delta - \frac{1}{2R}r^2 \tag{3.3}$$

Substituting the expressions of both the normal displacements $u_{z,1}$ and $u_{z,2}$ into Equation (3.3), it is possible to obtain

$$\frac{\pi p_0}{4aE^*}(2a^2 - r^2) = \delta - \frac{1}{2R}r^2 \tag{3.4}$$

from which the radius of the contact circle a and the mutual approach δ are derived

$$a = \frac{\pi p_0 R}{2E^*} \tag{3.5}$$

$$\delta = \frac{\pi p_0 a}{2E^*} \tag{3.6}$$

The total load F acting on the bodies is the integral of the pressure distribution over the whole contact area as

$$F = \int_0^a p(r)\, 2\pi r\, dr = \frac{2}{3} p_0 \pi a^2 \tag{3.7}$$

Introducing the expression of the total load F and rearranging the previous results, the force in function of the contact radius and in function of the mutual approach can be extracted

$$F = \frac{4}{3}\frac{M}{R} a^3 \tag{3.8}$$

$$F = \frac{4}{3} M \sqrt[2]{R} \delta^{3/2} \tag{3.9}$$

where the trigonometric relation $\delta = \frac{a^2}{R}$ is used. The concept of reduced modulus M is introduced as

$$\frac{1}{M} = \frac{1-{\nu_1}^2}{E_1} + \frac{1-{\nu_2}^2}{E_2} \tag{3.10}$$

3.1.2 Contact between an axisymmetric indenter and a flat surface

The framework proposed in the Section 3.1.1 can be directly translated into the problem of contact between a rigid spherical indenter (indenter) and a flat isotropic elastic surface (sample). In this case, the reduced modulus is regarded as indentation modulus.

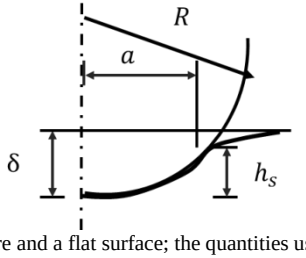

Figure 3.2: Contact between a sphere and a flat surface; the quantities used in the description of spherical indentation are presented.

The hypothesis of rigid indenter means that the expression of reduced modulus can be simplified as

$$\frac{1}{M} = \frac{1-{\nu_{sample}}^2}{E_{sample}} + \frac{1-{\nu_{indenter}}^2}{E_{indenter}} \sim \frac{1-{\nu_{sample}}^2}{E_{sample}} \tag{3.11}$$

According to Figure 3.2, the mutual approach δ introduced in Equation (3.6) can be recalled indentation depth h_s and the force can be derived

$$F = \frac{4}{3} M \sqrt[2]{R} {h_s}^{3/2} \tag{3.12}$$

The mean contact pressure p_m, expressed as $p_m = \frac{p_0}{\pi a^2}$, can be written as

$$p_m = \frac{4E^* a}{3\pi R} \tag{3.13}$$

whereas the contact area, A_{sphere}, is

$$A_{sphere} = \pi(2Rh_s - h_s^2) \tag{3.14}$$

that, under the hypothesis of Hertzian contact, reduces to

$$A_{sphere} \sim 2\pi R h_s \tag{3.15}$$

Similar Equations can be developed for the case of elastic contact between a rigid conical indenter and an elastic flat surface as proposed by Sneddon (Sneddon, 1965).

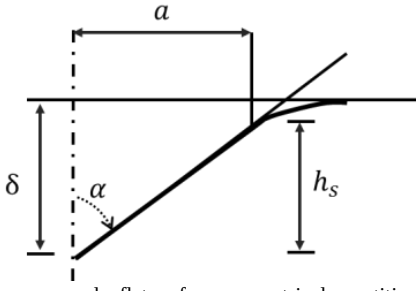

Figure 3.3: Contact between a cone and a flat surface; geometrical quantities used in the description of the conical indentation are presented.

Total load F and indentation depth h_s are related as

$$F = \frac{2}{\pi} M h_s^2 \cot \alpha \tag{3.16}$$

where α is the half angle of the cone. The expression for the contact area A_{cone} is

$$A_{cone} = \pi h_s^2 tan^2 \alpha \tag{3.17}$$

Once the contact area is computed, the concept of characteristic contact length can be introduced with the same meaning of the contact radius; hence, $l_{c,s}$ for a spherical indenter and $l_{c,c}$ for a conical one are defined, respectively, as

$$l_{c,s} = \sqrt[2]{2Rh_s - h_s^2} \tag{3.18}$$

$$l_{c,c} = h_s tan\alpha \tag{3.19}$$

The approach of Tabor (Tabor, 1951) permits to extract an estimation of the stress - strain relationship from a load - indentation curve: starting his study from the plasticity of metals, in his work, he proposes the following Equations; recalling σ_{eq} the stress (for both conical and spherical indenters), $\varepsilon_{eq,s}$ the strain for spherical indentation and $\varepsilon_{eq,c}$ the strain for conical indentation, it results that

$$\sigma_{eq} = \frac{F}{A_i} \tag{3.20}$$

$$\varepsilon_{eq.s} = K_\varepsilon \frac{l_{c,s}}{R} \tag{3.21}$$

$$\varepsilon_{eq,c} = cot\ \alpha \tag{3.22}$$

where A_i is the contact area in one of the two cases. K_ε is an empirical constant: Tabor suggests $K_\varepsilon = 0.2$ for metals. The application of Equation (3.21) to AFM-based indentation tests can be found in Lin (Lin, Dimitriadis , & Horkay, 2007) for the case of non-linear elastic materials under large deformations, in Iwashita (Iwashita, Swain, Field, Ohta, & Bitoh, 2011) in the case of viscoelastoplastic behavior and in the work of Briscoe (Briscoe, Fiori, & Pelillo, 1998) for polymers. In all these cases, the assumption of $K_\varepsilon = 1$ is used. In a second work of Lin (Lin, Shreiber, Dimitriadis, & Horkay, 2009) dealing with the indentation of soft tissues, instead, $K_\varepsilon = 0.2$ is proposed. The first solution is accepted in this work.

3.1.3 Extraction of parameters from an indentation test

A generic loading – unloading indentation curve of a poroviscoelastoplastic material is presented in Figure 3.4.

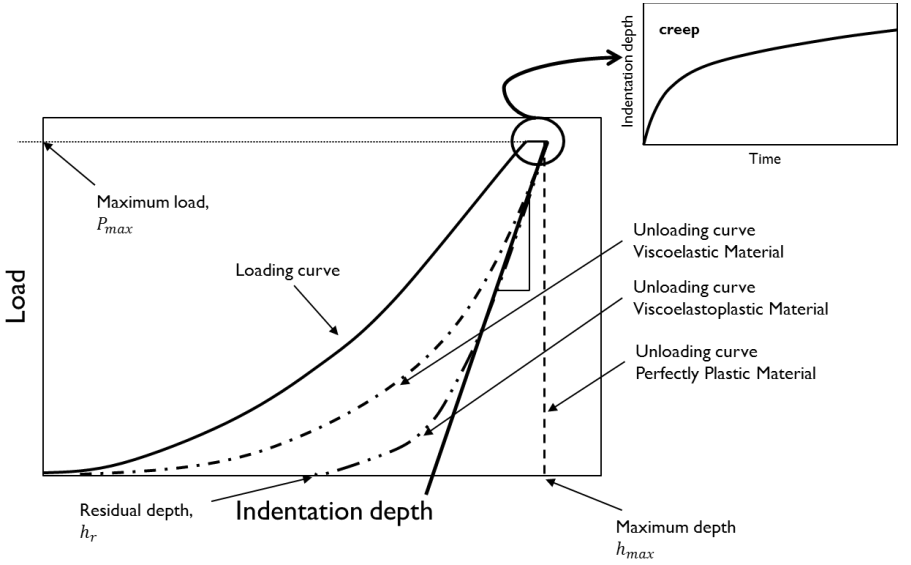

Figure 3.4: Typical loading – unloading indentation curve. Key feature are shown as well as the different behaviors of the unloading curve due to the different material responses. In the box, an example of creep, measured at maximum load, is highlighted.

Traditionally, the information contained into an indentation curve can be summarized in two quantities: the indentation stiffness S and the hardness H,

defined as (Vlassak & Nix, 1993)

$$S = \frac{dF}{dh}|_{h=h_{max}} = \frac{2}{\sqrt[2]{\pi}} M \sqrt[2]{A} \tag{3.23}$$

$$H = \frac{F_{max}}{A} \tag{3.24}$$

where the subscript max indicates the largest force or indentation depth reached.
The indentation stiffness S is related to the elastic properties of the material through the value of the indentation modulus. The hardness H is a measure of the resistance of a material to suffer permanent plastic deformations; it is related to the imprint left by the indenter after the unloading phase (depending on h_r in Figure 3.4).
Several techniques have been developed in order to extract these quantities from an indentation test: for example, in the Oliver and Pharr method the computations are based on the tangent of the unloading phase at maximum load and on the derivative of the elastic contact of an equivalent conical indenter; the Field and Swain method is, instead, based directly on the analysis of the unloading phase by using the elastic framework proposed in the previous Sections (Fischer-Cripps, 2005) of this Chapter. In this work, the quantities are extracted applying the theory of indentation of spherical or conical tips onto an elastic half - space directly to the loading curves and, more important, studying the behavior during the creep phases.
The indentation modulus is the principal parameter extracted from an indentation test. Equation (3.11) holds in case of elastic isotropic material. Introducing the forth order stiffness tensor of the half space $\mathbb{C}$, the same Equation can be written as (Delafargue & Ulm, 2004)

$$M_{iso} = \frac{E_s}{1-{\nu_s}^2} = \frac{C_{1111}^2 - C_{1122}^2}{C_{1111}} \tag{3.25}$$

where the subscript 's' replaces '*sample*' and C_{1111} and C_{1122} are coefficients of $\mathbb{C}$**.**
According to the work of Delafargue (Delafargue & Ulm, 2004), it is also possible to extract an explicit formulation that links the indentation modulus to the elastic properties of a transversely isotropic elastic material solicited by a conical indenter along the axis of symmetry (direction 3 in the following Equations). The other two cases, the indentation of a transversely isotropic material along the direction normal to the axis of symmetry and the indentation of an orthotropic material are not presented here since they are not used in this work.
The problem of indentation of a transversely isotropic material in direction 3 is axisymmetric and it gives a circular contact area; the Elliot-Hanson solution states

$$F = \frac{2}{\pi^2 \mathrm{Z}} h^2 \tan(\alpha) \tag{3.26}$$

where Z is a constant that depends only on four of the five material stiffness coefficients:

$$\mathrm{Z} = \frac{1}{2\pi} \sqrt[2]{\frac{C_{1111}}{C_{1111}C_{3333} - {C_{1133}}^2} \left(\frac{1}{C_{2323}} + \frac{2}{\sqrt[2]{C_{1111}C_{3333}} + C_{1133}} \right)} \tag{3.27}$$

Using Equations (3.17) and (3.26) in (3.23), the indentation modulus for a transversely isotropic material becomes

$$M_{tras,\parallel} = \frac{1}{\pi H} = 2\sqrt{\frac{C_{1111}C_{3333} - {C_{1133}}^2}{C_{1111}}\left(\frac{1}{C_{2323}} + \frac{2}{\sqrt[2]{C_{1111}C_{3333}} + C_{1133}}\right)^{-1}} \tag{3.28}$$

where Equation (3.27) is used in the second equality.
A further interesting result is presented by Vlassak (Vlassak, Ciavarella, Barber, & Wang, 2003): he reports that both conical and spherical indentation theories extract the same value for the indentation modulus $M_{tras,\parallel}$ and, therefore, Equation (3.28) can be used also in the case of spherical indentation.
For a poroelastic material, the information on the drained state is contained in the elastic stiffness tensor computed in drained condition $\mathbb{C}^{\boldsymbol{d}}$; calling $\mathbb{S}^{\boldsymbol{d}} = \mathbb{C}^{\boldsymbol{d^{-1}}}$ the elastic compliance tensor in the drained state, it is possible to derive the compliance tensors in the undrained condition, as proposed by Cowin (Cowin & Doty, 2006)

$$\mathbb{S}^{\boldsymbol{u}} = \mathbb{S}^{\boldsymbol{d}} - K\left(\mathbb{S}^{\boldsymbol{d}}\boldsymbol{m} \otimes \mathbb{S}^{\boldsymbol{d}}\boldsymbol{m}\right) \tag{3.29}$$

where $K = \left(\boldsymbol{m}^{\boldsymbol{T}}\mathbb{D}^{\boldsymbol{d}}\boldsymbol{m}\right)^{-1}$ and $\boldsymbol{m} = [1\ 1\ 1\ 0\ 0\ 0]$.
Then, if one applies Equations (3.25) or (3.28) using, alternatively, $\mathbb{C}^{\boldsymbol{d}}$ and $\mathbb{C}^{\boldsymbol{u}}$, where the elastic stiffness tensor in undrained condition is $\mathbb{C}^{\boldsymbol{u}} = \mathbb{S}^{\boldsymbol{u}^{-1}}$, it is possible to obtain analytically the values of the indentation modulus M in both drained and undrained conditions.

3.2 ATOMIC FORCE MICROSCOPE AND NANOINDENTER

All the experimental data presented in this work are collected using two instruments that differ each other in terms of the technologies they are based on and the working procedures as well as for the characteristic sizes that can be investigated (nanometric vs micrometric) and the domain in which they can work (frequency vs time): an Atomic Force Microscope (AFM), used to test AC samples with DMA tests at characteristic lengths from hundreds of nanometers to micrometers; a Nanoindenter (NI) used to test AC samples with creep tests at characteristic lengths from micrometers to hundreds of micrometers. Both of them are able to put a tip in contact with the surface of a sample and to record the load – indentation curve, varying experimental parameters as the geometry of the problem (tip size and indentation depth), loading and unloading rates, environmental conditions and timing. In general, they are able to probe the local properties of a material at less than millimetric size.

3.2.1 Atomic Force Microscope

In Figure 3.5, a scheme of a modern AFM setup is briefly described. A cantilever is

controlled at one end whereas a tip is mounted on the free one; the deflection of the cantilever is recorded through the reflection of a laser beam on the reflecting edge of the cantilever (Mayer & Amer, 1988).

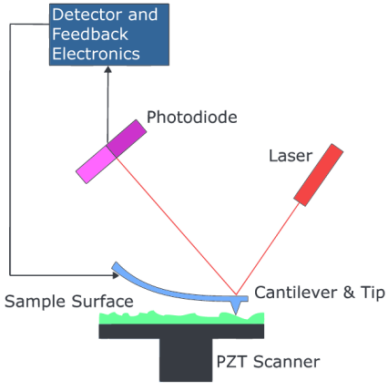

Figure 3.5: AFM-based nanoindentation setup.

The AFM used in this work is a commercial one (Agilent Technologies 5500, Agilent Technologies, Santa Clara, CA, USA) equipped with a closed - loop scanner. Both the cantilevers and the tips can be customized for the particular needs. The cantilevers are commercial silicon nitride, tip - less, rectangular devices and their spring constants are determined by the thermal noise method (Hutter & Bechhoefer, 1993) which allows a level of accuracy of $5-10\%$; the tips are customized and glued with epoxy resin (Epicote 1004, Shell Chemicals, London, UK) onto the free end of the cantilever using the translational stage of an optical microscope as described in details by Raiteri (Raiteri, Preuss, Grattarola, & Butt, 1998). The typical sizes of the tip range at the nanometric scale.
An AFM instrument can be used in different way, depending on the needs. The one used to collect data for this work is the contact mode: the tip is put in contact with the surface and a displacement is applied to the controlled end of the cantilever by the use of a piezo stage. The reaction force can be directly computed from the consequent reflected light.

3.2.2 Nanoindenter

Two configurations define the basis of nanoindenters actually commercialized: i) the sample is positioned horizontally and the tip movement is vertical; ii) the sample is positioned vertically and the tip movement is horizontal. Two also are the technologies used to apply the load and to record the displacement (or vice versa): i) it is inductive if the tip is driven by the current that flows into a coil; ii) it is capacitive if the tip is driven by the tension applied to a capacitor.
The NI used in this work is a NanoTest Indenter with the Platform 3 software installed (Micro-Materials Ltd., Wrexham, UK); it can be also equipped with a

liquid cell able to keep samples in a hydrated and fully saturated state as used in this work. The sketch of the setup is shown in Figure 3.6.

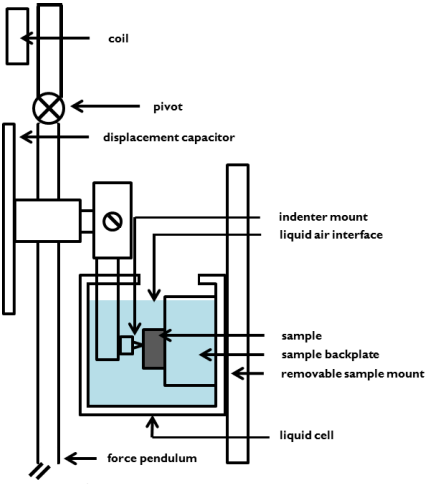

Figure 3.6: Setup of a nanoindentation test in liquid environment.

In this case, the interaction between tip and sample occurs horizontally. The load is generated by an electric current through a coil (inductive system) and applied to one end of the pendulum. By means of a lever system, the force is transferred to the tip that is pressed into the sample. The relative displacement of the tip, measure of the indentation depth, is recorded through a capacitive sensor mounted on the back of the tip: changing the distance of the plates results in a change of tension measured and, through deterministic correlations, in change of depth. The whole setup is placed into an environment at controlled temperature and humidity.

3.3 TIME DOMAIN AND FREQUENCY DOMAIN

With reference to Figure 3.4, AC shows peculiar aspects from the point of view of nanoindentation results. First, no residual depth can be found since no plasticity occurs and the effects of time dependent properties are relevant: hence, some preliminary considerations can be suggested.

1. AC is a soft tissue. Even with large deformations, no plasticity neither damage occur; the same consideration can be done for PDMS, at least within the range of indentation depths analyzed. These tissues recover completely after the removal of the load so no residual depths are present.
2. AC and PDMS have time dependent properties. Important information about their properties are condensed into the creep phase, depending on the loading rate with which the load path is covered.

According to the dichotomy between viscoelasticity and poroelasticity shown in

Chapter 2, PDMS is used in this thesis as a reference viscoelastic material.
Time dependencies can be studied, in time domain, using creep and stress relaxation tests and, in frequency domain, using the procedure of Dynamic Mechanical Analysis.

3.3.1 Time domain: creep tests and stress relaxation tests

Creep test is a well - known procedure to measure the time dependent properties of material, both poroelastic or viscoelastic. It consists on applying a load until a certain value is reached; then, this value is kept constant and the consequent displacement of the actuator is measured. This displacement varies with time in dependence on the material properties.
The dual experiment is the stress relaxation test in which a prescribed displacement of the actuator is reached and kept fixed, whereas the reaction force is continuously measured. In Figure 3.7 a representation of both the force and the displacement of the actuator in the cases of creep and stress relaxation test is presented.

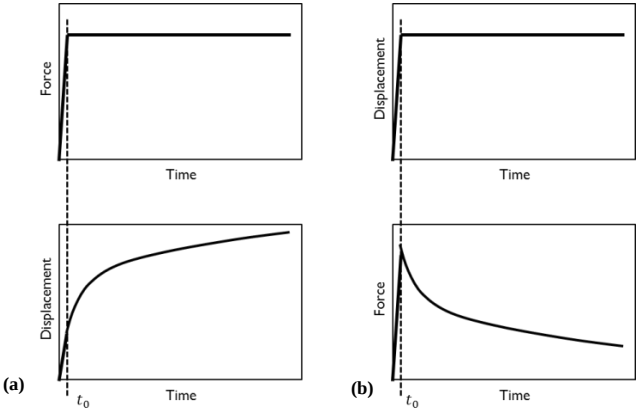

Figure 3.7: Force vs Time and Displacement vs Time in case of (a) creep test and (b) stress relaxation test. Force (creep) and displacement (relax) increase till the prescribed value obtained a $t = t_0$ and, then, they are kept constant. As a consequence, displacement (creep) and force (relax) increase till $t = t_0$ and, after that, their variations depend on the material properties.

The relations between the measure itself and the properties of the material can be extracted by the use of proper models; in literature, several approaches are described in the field of soft hydrated material, proposing both exact solutions and approximated ones. No closed form solutions are available for spherical poroelastic nanoindentation problems; Mak (Mak, Lai, & Mow, 1987) proposes a numerical solution for flat punch indentation which has been obtained by using double Laplace and Hankel transforms.
The one dimensional consolidation problem of the confined compression of poroelastic medium has, instead, a closed form solution for the time history displacement of sample top surface. The solution for isotropic tissue properties is

easily obtained (Biot, 1941) whereas the solution for transversely isotropic tissue and unconfined compression has been derived by Cowin and Mehrabadi (Cowin & Mehrabadi, 2007). In the following, the one dimensional consolidation problem is presented using the framework introduced by Cowin (Cowin & Doty, 2006). Let us consider a sample of thickness *L* and denote the vertical direction by the subscript 3.

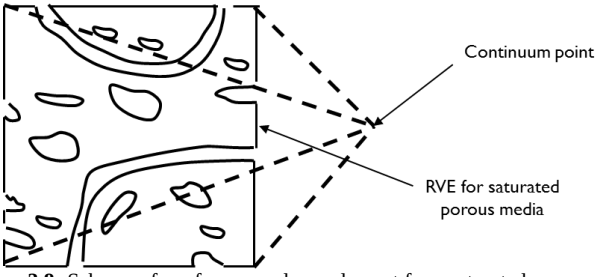

Figure 3.8: Scheme of a reference volume element for a saturated porous media.

Consider a representative volume element (RVE) of saturated porous medium: its strain-stress-pore pressure relationship can be written as

$$\widehat{\boldsymbol{E}} = \widehat{\boldsymbol{S}}_d \cdot \widehat{\boldsymbol{T}} + \widehat{\boldsymbol{S}}_d \cdot \widehat{\boldsymbol{A}} p \tag{3.30}$$

where $\widehat{\boldsymbol{S}}_d$ is the overall drained elastic anisotropic compliance matrix, $\widehat{\boldsymbol{E}}$ is the strain, $\widehat{\boldsymbol{T}}$ the stress, p the pressure and $\widehat{\boldsymbol{A}}$ the Biot effective stress tensor. The latter is related to the mismatch between the overall elastic properties $\widehat{\boldsymbol{S}}_d$ and the solid matrix elastic properties $\widehat{\boldsymbol{S}}_m$:

$$\widehat{\boldsymbol{A}} = \left(\widehat{\boldsymbol{1}} - \widehat{\boldsymbol{S}}_d{}^{-1}\widehat{\boldsymbol{S}}_m\right) \cdot \widehat{\boldsymbol{U}} \tag{3.31}$$

with $\widehat{\boldsymbol{U}} = [1,1,1,0,0,0]^T$. The hat "^" indicates averaging on a RVE.
Consider $P_{33} = -P_0 H(t)$ the load applied to the surface, where P_0 is a constant and $H(t)$ is the Heaviside function; two boundary conditions are applied on pore pressure field, $p = 0|_{x_3=0}$ and $\frac{\partial p}{\partial x} = 0|_{x_3=L}$ (permeable top surface and impermeable bottom surface). Under geometrical considerations, the only non-zero strain component is E_{33}. Applying Equation (3.30) and the compatibility Equations, the consequent displacement field $u_3(x,t)$, dependent on both position x and time t, can be derived. Since the behavior of the material is time dependent, the displacement u_3 of the surface (indicated by the vertical coordinate $x_3 = 0$) is the sum of two contributions: the initial displacement at $t = 0$ due to the loading, $u_3^i(0,0)$, and the transient displacement due to the creep effect, $u_3^t(0,t)$.

$$u_3(0,t) = u_3^i(0,0) + u_3^t(0,t) \tag{3.32}$$

The behavior of a poroelastic medium is dependent on both the geometrical parameters of the experiment and the constitutive parameters of the material; hence, a dimensionless time parameter τ can be introduced. For confined compression

tests, Galli (Galli & Oyen, 2009) uses $\tau = \frac{ct}{4L^2}$ where t is the physical time and c is a diffusivity parameter which is proportional to the tissue permeability and tissue stiffness; its physical unit is $\frac{L^2}{T}$.
Equation (3.32) becomes (Biot, 1941)

$$u_3(0,\tau) = u_3^i(0,0) + u_3^t(0,\tau) = \frac{\alpha(1+\nu_d)WLP_0}{3K_d(1-\nu_d)}[1 + g(\tau)] \qquad (3.33)$$

with

$$g(\tau) = \sum_{m=0}^{\infty} \frac{8}{(1+2m)^2\pi^2}\left[1 - e^{-(1+2m)^2\pi^2\tau}\right] \qquad (3.34)$$

where K_d and ν_d are bulk modulus and Poisson's ratio in drained condition and $W = \frac{SC_d(1+\nu_d)}{[3\Lambda(1-\nu_d)+\alpha SC_d(1+\nu_d)]}$; $\alpha = 1 - \left(\frac{K_d}{K_m}\right)$ is the isotropic effective stress coefficient, S the Skempton parameter, $C_d = \widehat{\boldsymbol{U}}^T\widehat{\boldsymbol{S_d}}\widehat{\boldsymbol{U}}$ and Λ is a scalar function of the drained elastic properties of the porous matrix.

3.3.2 Dynamic mechanical analysis

An AFM - based DMA nanoindentation test consists in two phases. First, a prescribed mean indentation depth h_s is reached applying the correct load F; second, over the deformed configuration obtained, an harmonic load is imposed through a sinusoidal signal of a given amplitude and a given frequency: a displacement signal of magnitude Δh_0 is applied on the cantilever end connected to the piezo stage. The correspondent quantity, a reaction force, is computed by measuring the cantilever deflection Δh_c: it is a sinusoidal signal at the same given frequency but characterized by an amplitude and a phase shift depending on the material properties. In Figure 3.9, the scheme of the procedure for an AFM - based nanoindentation dynamic test is presented: Δh_0 defines the amplitude of the signal in input; Δh_c defines the amplitude of the signal in output; $\emptyset(f)$ defines the phase shift. To rely into the proposed analytical framework, $\Delta h_0 \ll h_s$: in particular, in all the experiments proposed in Section 4.1, $\Delta h_0 = 10\ nm$.
In the first step of the procedure described above, the mean indentation depth is reached imposing a load. In order to collect the information on h_s over which the dynamic test is performed, preliminary classical loading – unloading nanoindentation tests are performed at each load used in the DMA analysis: analyzing these data within the framework of the Hertzian contact, the corresponding indentation depths are found for any of the load investigated.
In a static condition, the linearity in the elastic response of the cantilever results in a direct relation between the measured cantilever deflection h_c and the reaction force F through the cantilever stiffness

$$F = k_c h_c \qquad (3.35)$$

More generally, Equation (3.35) holds also for the amplitude of the harmonic

reaction force when the system is solicited at a generic frequency f

$$\Delta F(f) = \Delta h_c(f) k_c \tag{3.36}$$

where Δ indicates that the amplitude and not the signal itself.

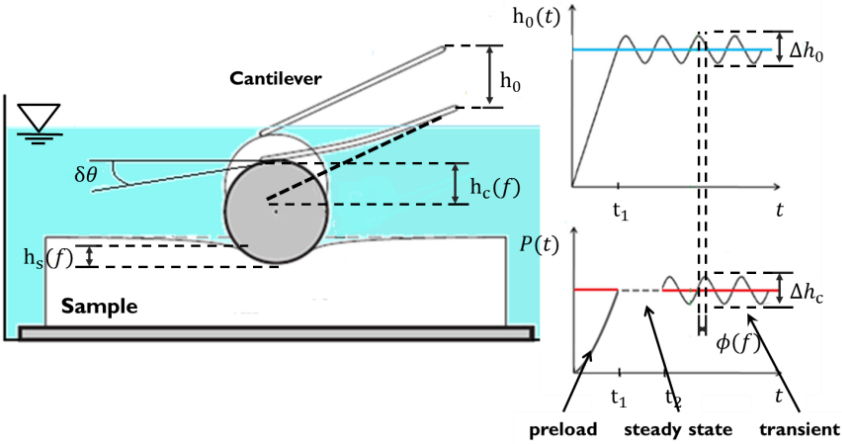

Figure 3.9: Scheme and examples of data recorded for an AFM-based nanoindentation dynamic test.

The upper end of the cantilever is driven in displacement. If prescribed displacement $\overline{h_0}$ is imposed, the tip penetrates into the sample of an amount $\overline{h_s}$ and the cantilever deflects of an amount $\overline{h_c}$ according to the following additive relation

$$\overline{h_0} = \overline{h_s} + \overline{h_c} \tag{3.37}$$

Then, the harmonic displacement of amplitude Δh_0 and frequency f is applied over this deformed configuration. Additive decomposition for the displacements holds also for the signal amplitudes:

$$\Delta h_0 = \Delta h_s + \Delta h_c \tag{3.38}$$

The outputs are the amplitude ratio, $R^{i/o}(f) = \frac{\Delta h_c}{\Delta h_0}$, and the phase lag, $\emptyset(f)$, between the input (Δh_0) and the output (Δh_c) signals.
Combining Equations (3.36) and (3.38) the following relationship can be derived

$$\frac{\Delta F}{\Delta h_s} = \frac{k_c \Delta h_c}{\Delta h_0 - \Delta h_c} = \frac{k_c R^{i/o}}{1 - R^{i/o}} \tag{3.39}$$

where Δh_s is the amplitude of the harmonic indentation depth signal.
From the work of Cheng (Cheng, Ni, & Cheng, 2006), the reduced storage modulus $E'^{*}(f)$ and the reduced loss modulus $E''^{*}(f)$ can be calculated, in case of spherical tip as

$$E'^{*}(f) = \frac{1}{2} \frac{1}{\sqrt[2]{R h_s}} \left| \frac{\Delta F(f)}{\Delta h_s} \right| \cos(\phi_f) \tag{3.40}$$

$$E''^{*}(f) = \frac{1}{2}\frac{1}{\frac{2}{\sqrt{Rh_s}}}\left|\frac{\Delta F(f)}{\Delta h_s}\right|\sin(\phi_f) \tag{3.41}$$

Indeed, for the case of conical tip holds

$$E'^{*}(f) = \frac{\pi}{4\tan(\theta)}\frac{\Delta F}{\Delta h}\cos(\emptyset_f) \tag{3.42}$$

$$E''^{*}(f) = \frac{\pi}{4\tan(\theta)}\frac{\Delta F}{\Delta h}\sin(\emptyset_f) \tag{3.43}$$

3.4 EXPERIMENTAL PROBLEMS AND SUGGESTED SOLUTIONS

Nanoindentation is a widely used experimental technique for the analysis of biological tissues (Ebenstein, et al., 2006): its application on hard materials (i.e, bone tissue) is already well established as well as the theoretical and the numerical methods provide reliable results (Carnelli, Lucchini, Ponzoni, Contro, & Vena, 2011). From the experimental point of view, indeed, it has a relatively simple experimental setup (Gouldstone, et al., 2007) that can be upgraded quite easily: the application in liquid environment is central in this work and presented in literature, for example, by Li (Li, Korhonen, Iivarinen, Jurvelin, & Herzog, 2008).

No special procedures for sample preparation are required and, even more important, the technique is able to probe small amount of material with respect to the sample size: therefore, material properties of intact tissue can be obtained since the test is performed in a zone far from the boundaries. In the work of Korhonen (Korhonen, et al., 2002), a comparison of results obtained from confined compression, unconfined compression and indentation can be found, suggesting the differences can be due to the experimental techniques; in his PhD thesis, Wilson (Wilson, 2005) says that a part of the differences found in literature about the measured swelling strain in AC can be explained looking at the procedures used to extract the samples.

The field of soft hydrated tissues and materials, like AC or PDMS, presents a wide range of open questions regarding both experiments and models, indeed. Some of the experimental issues addressed to this work, followed by the solutions suggested, are reported here.

Adhesion is a phenomenon related to the presence of molecular forces, attractive or repulsive, between sample and tip, causing artifacts in the detection of the force if the dimension of the tip (or, better, the dimension of the contact length) is of the same length at which the electrochemical interactions act. Typical dimensions analyzed in this work span from tens of nanometers to few hundreds of micrometers. Hence, the adhesion can play a role only around the contact approach when the smaller probes (experiments at small characteristic lengths) are used; for all the other cases, adhesion effects can be neglected. Anyway, whenever this problem arose, it has been overcome using the proposed method for the detection of the initial contact point. The proper definition of the *initial contact point* is crucial and,

with or without adhesion, it requires a not trivial treatment: a wrong definition can follow in completely wrong considerations on the material properties.
Experimental procedures and literature papers already present solutions to solve this problem. For example, if the prescribed forces are orders of magnitude higher than the adhesion forces, an high value for the lowest force measurable can be set; as a consequence, the measure starts when the tip is certainly inside the sample but losing the information at low loads. In the present work, instead, detectable low level of load is required due to the low stiffness of the material: the approaches proposed above can't be used. In the work of Nia (Nia, Han, Li, Ortiz, & Grodzinsky, 2011) a detection algorithm during the post-processing phase is proposed.
In this thesis, the following procedure is used. Let us consider a force F – displacement h curve as in Figure 3.10.

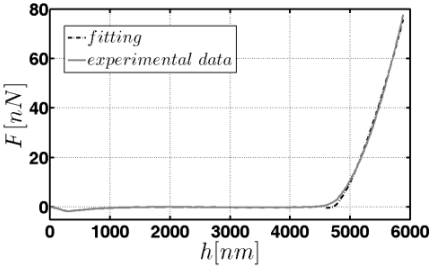

Figure 3.10: Example of force displacement curve (solid line) and best fitting curve (dashed line).

It is important to note that, in Figure 3.10, displacement h identifies the current position of the tip, from a reference position far from the surface to a certain depth measured from the reference point: it is not the indentation depth h_s; the contact point has to be defined somewhere in between $0 - 6000\ nm$ for the case shown in Figure. Equations (3.12) and (3.16) can be rewritten as

$$F = \frac{4}{3}\sqrt[2]{R}M_1(h - M_2)^{3/2} \tag{3.44}$$

$$F = \frac{2}{\pi}M_1(h - M_2)^2\ cot\ \alpha \tag{3.45}$$

assuming that the unknown parameters are the indentation modulus, M_1, and the displacement at which the contact occurs, M_2. A best fitting procedure is applied between the experimental load - displacement curve and the above relations: the procedure is implemented within a Matlab environment (MathWorks, Natick, MA, USA) using a least square method based on the interior - point algorithm. The knowledge of parameters M_2 gives the possibility to define the indentation depth since $h_s = h - M_2$ while M_1 is an estimation of the quasi static indentation modulus. Moreover, the softness of the material and the large displacement investigated could invalidate the correlations proposed in literature for hard materials. Hay (Hay &

Wolff, 2001) proposes a correction factor in the case of load - indentation curve in spherical indentation, showing how the error committed using the original *Hertzian approach* increases, moving to the case of incompressible material. The experimental work of Dintwa (Dintwa, Tijskens, & Ramon, 2008), instead, justifies the application of the Hertzian contact also in case of large deformations in soft tissues. In the present work, based on the hypothesis of Dintwa, an high value of the parameter R^2, found in applying the best fitting procedure described above, is used as index of goodness of that hypothesis: hence this verification is done for all the curves analyzed.

Again, due to the softness of the material, *low forces* are required even for large displacements. Then, the variation in voltage (or current) that the instrument has to detect can be very low, causing a very noisy measure. This problem rises, in particular, in the studies of small tips pressed at small indentation depths: the solution is the developing of a customized software. This point is not object of the this thesis since it refers to the AFM used in the University of Genova where the dynamic experiments are carried out.

Thermal drift can play an important role in a nanoindentation test: due to the small amount of volume tested, variations in temperature during the experiments can result into local heat flow between tip and sample, potentially affecting the measure. In a classical loading – unloading nanoindentation the effect of thermal drift is cleared up providing a correction computed leaving the tip in contact at a fixed small load level and fitting the consequent measured displacement with a linear relation; a correction computed on $60\,s$ is a typical value for an overall time testing length of few minutes. All the tests performed in this work are, instead, quite a long tests, overcoming tens of minutes: this means that the thermal variability that can be extracted within the last 30 – 60 s can not be considered representative of the whole experiment. Therefore, since the thermal conditions are monitored and a built - in control system was working, the variability along the whole duration of the experiment can be considered at mean null. No correction is applied to the data. Strictly related to the previous point is the question about the separation between the time dependent behavior due to the tissue properties and the one due to the thermal drift: the suggested explanation allows to consider that the whole measure is referred to material properties.

A particular problem is specific for tests based on DMA. A simple way to model a real system is through an equivalent based on a mass, a spring and a damper: this kind of system has a proper *natural frequency*. If this system is solicited at that specific frequency, the amplitude of its response is infinite, if no damping is present, or very high, depending of the amount of damping. In Figure 3.11 a typical graph of the oscillation amplitude with respect to the frequency for a mass – spring - damper system is shown: the effect of the damper is highlighted.

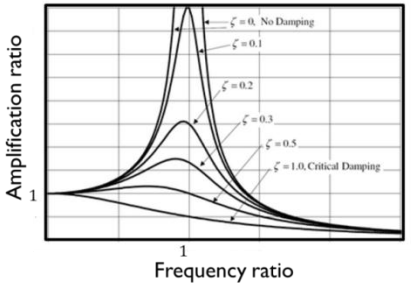

Figure 3.11: Typical amplitude response of a mass – spring – damper system. The abscissa contains the frequency normalized with respect of the natural frequency; ζ is the damping coefficient.

It is obvious that the response obtained soliciting the sample around that frequency is meaningless. This characteristic frequency can not be deleted, but the position can be changed varying the properties of the system: with reference to the specific configuration used in this work, the stiffness of the cantilever is the changeable parameter since the tip is fixed. Its choice comes from the balance between a cantilever too stiff, that causes large natural frequency but improper detection of low forces, and a too soft one, that allows the detection of low forces but has a small natural frequency that limit the range that can be swept. As a principle, the possibility to investigate up to $250\,Hz$ is the criterion used in the setting up of dynamic experiments.

3.5 SAMPLES PREPARATION

3.5.1 AC samples

Three different sets of AC samples are tested within the purpose of this work.

The samples to be tested in dynamic conditions are obtained from freshly slaughtered mature bovine knee. They are harvested from disarticulated femour (proximal condyles) within $1-2$ hours post - mortem using a biopsy punch with inside diameter of $2\,mm$. Each explanted plug consists of a full thickness articular cartilage fragment with its underlying subchondral bone. The plugs are transferred into PBS ($2.6\,mM\ NaH_2PO_4, 3\,mM\ Na_2HPO_4, 155\,mM, NaCl, 0.01\%\ NaN_3\ \frac{w}{v}, pH$ 7.0) supplemented with $20\ \frac{\mu g}{ml}$ of gentamycin, a protease inhibitor cocktail (P8340, St. Luis, MO, USA) and are kept on ice until use. This procedure has been performed at the Department of Biophysical and Electronic Engineering in University of Genova (Genova, Italy)

In the case of time domain tests on bovine AC, samples are obtained from lateral and medial condyles of a knee of slaughtered mature exemplary of bovine. The extraction of the samples is performed thorough a corer with inside diameter of $10\,mm$. During the extraction, the sample is constantly kept wet with physiological solution to avoid damage due to high temperature caused by the friction. Each

explanted plug consists of a full - thickness articular cartilage fragment with its underlying subchondral bone. The plugs are transferred into saline solution and are kept at temperature of $-80\ ^{o}C$ until measurement.

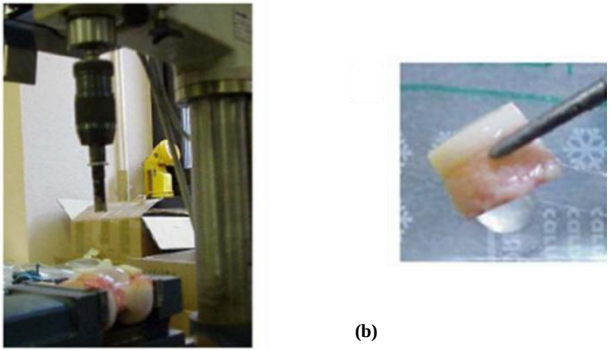

(a) (b)

Figure 3.12: (a) Setup for the extraction of bovina AC samples; (b) sample extracted: full thickness articular cartilage fragment with its underlying subchondral bone.

In case of time domain tests on porcine samples, they are extracted from porcine joints of the specie minipig, 18 months old and $70\ kg$ in weight. Control cartilage samples and engineered cartilage samples are considered: the control ones are extracted from medial and lateral femoral condyles of the left posterior articulation whereas engineered ones are extracted from the right counterpart. Photos of the articulation and the samples are shown in Figure 3.13. Samples diameter is in between $4.5 - 5\ mm$. This procedure has been performed at IRCCS, Istituto Ortopedico Galeazzi (Milano, Italy).

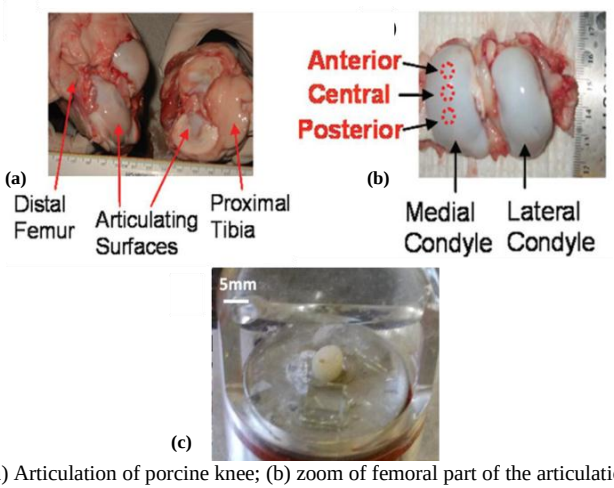

Figure 3.13: (a) Articulation of porcine knee; (b) zoom of femoral part of the articulation: the sites of extraction are highlighted; (c) sample extracted.

For all the situations, no sample by sample measurement of cartilage thickness has been carried out since the expected indentation depths are two orders of magnitude lower than the cartilage thickness; therefore, no effect of through – the - thickness material heterogeneity is expected.
In order to have top and bottom parallel surfaces, the irregular bone surface is manually grinded using a rasp just before to start the test. It is also assumed the freezing does not affect the behavior of the tissue as described by Kiefer (Kiefer, et al., 1989).

3.5.2 PDMS samples

PDMS disks are obtained mixing viscous components and curing agents with a ratio of 10:1 by weight using the commercial Sylgard 184 Elastomer Kit (Dow Corning, Midland, Michigan, USA). After mixing the two components for, at least, 5 minutes, cycles of applied vacuum and rest are done in order to eliminate all the air bubbles. PDMS samples solidify in a cylindrical mold of $15\ cm$ of diameter and $0.5\ cm$ of thickness at a temperature of $65\ ^{o}C$ for 45 minutes. Suitable PDMS samples are extracted using a biopsy punch with inside diameter of $10\ mm$.

REFERENCES

Biot, M. (1941). General theory of three dimensional consolidation. *Journal of Applied Physics, 12*, 155-164.

Briscoe, B., Fiori, L., & Pelillo, E. (1998). Nano-indentation of polymeric surfaces. *Journal of Physics D: Applied Physics, 19*, 2395-2405.

Carnelli, D., Lucchini, R., Ponzoni, M., Contro, R., & Vena, P. (2011). Nanoindentation testing and finite element simulations of cortical bone allowing for anisotropic elastic and inelastic mechanical response. *Journal of Biomechanics, 44*(10), 1852-1858.

Cheng, Y., Ni, W., & Cheng, C. (2006). Nonlinear analysis of oscillatory indentation in elastic and viscoelastic solids. *Physical Rewiev Letters, 97*.

Cowin, S., & Doty, S. (2006). *Tissue Mechanics.* New York: Springer Verlag.

Cowin, S., & Mehrabadi, M. (2007). Compressible and incompressible constituents in anisotropic poroelasticity: The problem of unconfined compression of a disk. *Journal of the Mechanical and Physics of Solids, 55*(1), 161-193.

Delafargue, A., & Ulm, F. (2004). Explicit approximations of the indentation modulus of elastically orthotropic solids for conical indenters. *International Journal of Solids and Structures, 41*, 7351-7360.

Dintwa, E., Tijskens, E., & Ramon, H. (2008). On the accuracy of the Hertz model to describe the normal contact of soft elastic spheres. *Granular Matter, 10*, 209-221.

Fischer-Cripps, A. (2005). *The IBIS Handbook of Nanoindentation.* Forestville, NSW: Fischer-Cripps Laboratories Pty Ltd.

Galli, M., & Oyen, M. (2009). Fast identification of poroelastic parameters from indentation tests. *Computer Modeling in Engineering and Science, 48*, 241-268.

Gouldstone, A., Chollacoop, N., Dao, M., Li, J., Minor, A., & Shen, Y. (2007). Indentation across size scales and disciplines: recent developments in experimentation and modeling. *Acta Materialia, 55*, 4015-4039.

Hay, J., & Wolff, P. (2001). Small correction required when applying the Herzian contact model to instrumented indentation data. *Journal of Material Research, 16*(5), 1280-1286.

Hertz, H. (1882). Uber die bueruhrung fester elastischer koper. *Jurnal fur Die Reine und Anewandte Mathematik, 92*, 156-171.

Hutter, J., & Bechhoefer, J. (1993). Calibration fo atomic force microscope tips. *Review of Scientific Instruments, 64*(7), 1868-1876.

Iwashita, N., Swain, M., Field, J., Ohta, N., & Bitoh, S. (2011). Elasto-plastic deformation of glass-like carbons heat-treated at different temperatures. *Carbon, 39*, 1525-1532.

Johnson, K. (1985). *Contact Mechanics.* Cambridge: Cambridge University Press.

Kiefer, G., Sundby, K., McAllister, D., Shrive, N., Frank, C., Lam, T., & Schachar, N. (1989). The effect of cryopreservation on the biomechanical bhavior of bovine articular cartilage. *Journal of Orthopaedic Research, 7*, 495-501.

Korhonen, R., Laasanen, M., Toyras, J., Rieppo, J., Hirvonen, J., Helminen, H., & Jurvelin, J. (2002). Comparison of the equilibrium response of articular cartilage in unconfined compression, confined compression and indentation. *Journal of Biomechanics, 35*, 903-909.

Li, L., Korhonen, R., Iivarinen, J., Jurvelin, J., & Herzog, W. (2008). Fluid pressure driven fibril reinforcement in creep and relaxation tests of articular cartilage. *Medical Engineering & Physics, 30*, 182-189.

Lin, D., Dimitriadis , E., & Horkay, F. (2007). Elasticity of rubber-like materials measured by AFM nanoindentation. *eXPRESS Polymer Letters, 1*(9), 576-584.

Lin, D., Shreiber, D., Dimitriadis, E., & Horkay, F. (2009). Spherical indentation of soft matter beyond the Hertzian regime: numerical and experimental validation of hyperelastic models. *Biomechanics and Modeling in Mechanobiology, 8*, 345-358.

Mak, A., Lai, W., & Mow, V. (1987). Biphasic indentation of articular cartilage - I. Theoretical analysis. *Journal of Biomechanics, 20*, 703-714.

Mayer, G., & Amer, N. (1988). Novel optical approach to atomic force microscopy. *Applied Physical Letter, 53*(12), 1045-1048.

Nia, H., Han, L., Li, Y., Ortiz, C., & Grodzinsky, A. (2011). Poroelasticity of cartilage at the nanoscale. *Biophysical Journal, 101*, 2304-2313.

Oyen, M., & Cook, R. (2009). A practical guide for analysis of nanoindentation data. *Journal of the Mechanical Behavior of Biomedical Materials, 2*, 396-407.

Raiteri, R., Preuss, M., Grattarola, M., & Butt, H. (1998). Preliminary results on the electrostatic double layer force between two surface with high surface potential. *Colloid Surface A, 136*, 195-201.

Shahsavari, R., & Ulm, F. (2009). Indentation analysis of fractional viscoelastic solids. *Journal of Mechanics of Materials and Structure, 4*, 523-550.

Sneddon, I. (1965). The relation between load and penetration in the axisymmetric Boussinesq problem for a punch of arbitrary profile. *International Journal of Engineering and Science, 3*(1), 47-57.

Tabor, D. (1951). *The hardness of metals.* London: Oxford University Press.

Vlassak, J., & Nix, W. (1993). Indentation modulus of elastically anisotropic half space. *Philosophical Magazine A, 67*(5), 1045-1056.

Vlassak, J., Ciavarella, M., Barber, J., & Wang, X. (2003). The indentation modulus of elastically anisotropic materials for indenter of arbitrary shape. *Journal of Mechanics adnd Physics of Solids, 51*, 1701-1721.

Wilson, W. (2005). An explanation for the onset of mechanically induced cartilage damage. Eindhoven, Technische Universiteit Eindhoven.

Chapter 4.

Experimental Tests: Nanoindentation in Frequency Domain and Time Domain

This Chapter is dedicated to all the experimental data analyzed in the presented work of thesis, in both frequency and time domains and at micrometric characteristic lengths. Section 4.1 presents the analysis of data collected from harmonic AFM - based nanoindentation tests on bovine samples. Section 4.2 shows both the experimental procedures and the data analysis for multiload nanoindentation creep test on bovine samples. In Section 4.3 the procedure in time domain is applied to investigate the mechanical properties of engineered articular cartilage.

A unified experimental technique and a relevant interpretation framework able to assess mechanical properties of the AC in liquid environment at multiple micrometric characteristic sizes are still missing. The aim of this Chapter is to evaluate two experimental techniques for the quantitative interpretation of the poroviscoelastic response of AC when it is subjected to i) dynamic mechanical tests in frequency domain and ii) multiload spherical indentation test coupled with a creep test in time domain. In both the cases, the samples are kept in physiological condition. The characteristic lengths investigated are in the ranges $[0.05 - 5.5]\mu m$ in the case of DMA and $[10 - 140]\mu m$ in the case of multiload creep tests: hence, the possibility to provide constitutive information of the microstructure (up to the single bundle of fibers) is achieved. The procedure based on the creep tests is, then, used to investigate the mechanical behavior of engineered porcine cartilage.
In Chapter 3, the basic aspects of the experimental techniques as well as the consolidated theoretical frameworks used to analyze experimental results have been presented; the samples preparation has also been shown. In this Chapter, then, the novel aspects and the relative results are deeply described and explained.

4.1 AFM - BASED NANOINDENTATION DMA TESTS ON MATURE BOVINE ARTICULAR CARTILAGE

AFM - based nanoindentation tests and DMA tests are widely used as shown in the introduction; several works are already presented coupling these techniques at other methodologies operating at macroscale. The application at microscale, instead, is still not completely investigated, especially going down to nanometric scale and trying to compare the effects at different characteristic lengths.
In this work, the investigation is based on three different tips. The experiments have not been conducted personally but in University of Genova. In Table 4.1 the parameters for the pairs *tip geometry – cantilever stiffness* used are shown. Fixing the tip geometry, the choice of the cantilever stiffness is driven by the requirement to ensure an allowable frequency range of $[0 - 250]Hz$.

Table 4.1: Experimental setups for the three configurations used.

SPHERICAL TIPS		
NAME	**CANTILEVER CONSTANT** $\boldsymbol{k_c}\left[\frac{\boldsymbol{nN}}{\boldsymbol{nm}}\right]$	**TIP RADIUS** $\boldsymbol{R}\ [\boldsymbol{nm}]$
R_{7500}	7.18	7500
R_{665}	0.7	665

CONICAL TIP			
NAME	**CANTILEVER CONSTANT** $\boldsymbol{k_c}\left[\frac{\boldsymbol{nN}}{\boldsymbol{nm}}\right]$	**HALF ANGLE** $\boldsymbol{\theta}[°]$	**TIP HEIGHT** $\boldsymbol{h_t}[\boldsymbol{\mu m}]$
C	0.03	22	15

In order to investigate the effect of different characteristic lengths, for any of the three configurations, tests are performed at different mean indentation depths, h_s. As already described, each dynamic test is preceded by a classic nanoindentation test in order to extract the value of h_s: it is obtained using the best fitting procedure through the Equations (3.44) and (3.45).
Table 4.2 shows the mean indentation depths achieved, over which the harmonic signal is imposed. The imposed load is also presented. The best fitting procedure is applied to load – unload curves already averaged from different sites: therefore, the indentation depths obtained are mean values but the information of standard deviation is not available.

Table 4.2: Force - displacement tests perfomed.

GEOMETRY	LOAD APPLIED $F[nN]$	MEAN INDENTATION DEPTH $h_s[nm]$
R_{7500}	350	2300
R_{7500}	70	1200
R_{7500}	35	927
R_{7500}	7	500
R_{665}	40	583
R_{665}	20	361
R_{665}	10	224
C	60	500
C	50	408
C	40	353

4.1.1 Data correction

Over the deformed configuration obtained achieving the prescribed mean indentation depth, the harmonic displacement is imposed. The choice of the magnitude of the input cantilever displacement is a balance among having a measurable output, without affecting itself, and keeping the tip in contact; $\Delta h_0 = 10\ nm$ is chosen. As in the case of classical tests, each mean indentation depth is investigated with the repetition of 5 dynamic tests: all the data are presented as mean and standard deviation; in the plots, the bars indicate standard deviation.
As already presented in Chapter 3, the outputs from a dynamic test are the amplitude ratio, $R^{i/o,j}(f) = \frac{\Delta h_c}{\Delta h_0}$, and the phase lag, $\emptyset_f^j(f)$, between the peak of the input (piezo displacement ${\Delta h_0}^j$) and the peak of the output (cantilever deflection ${\Delta h_c}^j$) waves. The superscript j indicates the case, $j = R_{7500}, R_{665}, C$.
For any of the configuration (cantilever and tip) studied, a preliminary oscillatory indentation test is carried out on a reference stiff sample in order to calibrate the

phase data drift intrinsic to the measuring system. A glass microscope slide, that exhibits a perfectly elastic behavior at least at the temperature and applied loads of interest in this work, is used to this purpose; its phase lag is denoted by $\emptyset_g^j(f)$. Then, $\emptyset_r^j(f)$ is the raw phase lag collected for the dynamic indentation experiment and it is corrected according to the relation:

$$\emptyset_f^j(f) = \emptyset_r^j(f) - \emptyset_g^j(f) \tag{4.1}$$

where $\emptyset_f^j(f)$ is the corrected phase lag value. Equation (4.1) holds for all the configurations shown in Table 4.1 In Figure 4.1 an example of the phase shift $\emptyset_g(f)$ measured using the glass sample is shown. The result presented refers to configuration R_{7500}.

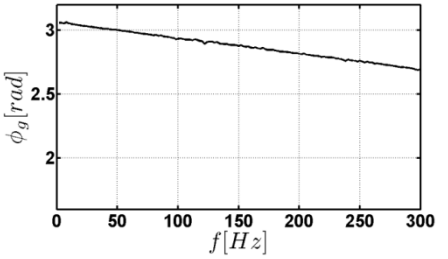

Figure 4.1: $\emptyset_g^{R_{7500}}(f)$ measured using the glass sample for the configuration R_{7500}.

For the three tips analyzed in this work, the phase correction is: $\emptyset_g^{R_{7500}}(f) = (\pi - 0.0014f)$ for the large spherical tip; $\emptyset_g^{R_{665}}(f) = (\pi - 0.0011f)$ for the small spherical tip; $\emptyset_g^{C}(f) = (\pi - 0.0013f)$ for the conical tip.

4.1.2 Experimental data analysis

Let us recall Equations (3.40) to (3.43) in which storage and loss moduli are computed for both the tip geometries: $E_s'^*(f)$ and $E_s''^*(f)$ for the spherical tip and $E_c'^*(f)$ and $E_c''^*(f)$ for the conical one.

In the case of quasi static loading ($f \to 0$) the behavior is basically governed by the elastic properties of porous matrix whereas, in the case of instantaneous loading ($f \to \infty$), the behavior is governed by the fluid flow through the pores of solid network. In this work, $E'^*(0)$ defines the drained modulus (in the case of time domain tests, it is recalled M_d maintaining the same meaning), whereas the undrained modulus, that exist properly only asymptotically is computed at the highest frequency analyzed and it is described by $E'^*(250)$ (in the case of time domain tests, it is recalled M_u). Drained and undrained moduli can be combined computing the normalized storage modulus (the consolidation rate in time domain) $\overline{E'^{*,j}}(f)$ and the drained to undrained ratio $R^{d/u,j}(f)$ defined as follow

$$\overline{E'^{*,j}}(f) = \frac{(E'^{*}(f) - E'^{*}(0))}{(E'^{*}(250) - E'^{*}(0))} \tag{4.2}$$

$$R^{d/u,j}(f) = \frac{E'^{*}(0)}{E'^{*}(250)} \tag{4.3}$$

where j indicates the configuration as shown before. $\overline{E'^{*,j}}(f)$ is dependent by the testing geometrical parameters; $R^{d/u,j}(f)$ is dependent by the tissue properties and independent by its time response.
Moreover, the balance between elastic and dissipative properties can be extracted from the shape of the tangent of the phase shift, $tan(\phi_f)$, versus frequency: its peak, $tan(\phi_f)_{max}$, is a measure of the amount of all the dissipative forces. The corresponding frequency at which it occurs, f_{max}, is indeed related to the typical time scale of the phenomenon under investigation. Since the lowest frequency measured is equal to $2\ Hz$, the value of $E'^{*}(0)$ is computed as a linear extrapolation of the first ten experimental data, ranging from $f = 2\ Hz$ to $f = 7.5\ Hz$, as presented in the work of Nia (Nia, Han, Li, Ortiz, & Grodzinsky, 2011).

4.1.3 Results

Using Equations (3.18) – (3.19) and (3.21) – (3.22) with the assumption of $K_\varepsilon = 1$, characteristic contact lengths and equivalent deformations can be computer for all the mean indentation depths analyzed. It is worth to be recalled that these two parameters can be considered, respectively, as a scalar representative measure of the inhomogeneous strain distribution beneath the indenter surface and the amount of tissue involved in the deformation process; these quantities, together with the information on the indentation depth, define an interesting way to better understand the response of the material and to relate them to its microstructure. In Table 4.3 these quantities are reported: as explained regarding the data in Table 4.2, mean values without standard deviations are presented.

Table 4.3: Indentation depths, computed equivalent deformations and characteristic contact lengths are reported for all the geometrical configuration analyzed.

SAMPLE	INDENTATION DEPTH $h_s[nm]$	EQUIVALENT DEFORMATION $\epsilon_{eq}[-]$	CHARACTERISTIC LENGTH $l_c[nm]$
R_{7500}, h_{2300}	2300	0.31	5405
R_{7500}, h_{1200}	1200	0.16	4070
R_{7500}, h_{927}	927	0.12	3620
R_{7500}, h_{500}	500	0.06	2693
R_{665}, h_{583}	583	0.88	660
R_{665}, h_{361}	361	0.54	592
R_{665}, h_{224}	224	0.33	498
C, h_{500}	500	2.5	129
C, h_{408}	408	2.5	105

SAMPLE	INDENTATION DEPTH $h_s[nm]$	EQUIVALENT DEFORMATION $\epsilon_{eq}[-]$	CHARACTERISTIC LENGTH $l_c[nm]$
C, h_{353}	353	2.5	91

The shape of the tangent of phase shift is presented in Figure 4.2; the different configurations (R_{7500}, R_{665}, C) are presented in separated plots and, within a single plot, results for all the indentation depths are shown. Looking at the frequency of the peak and at the magnitude of the peak itself, it is evident how the tissue response is different when the characteristic length of the experiment changes.

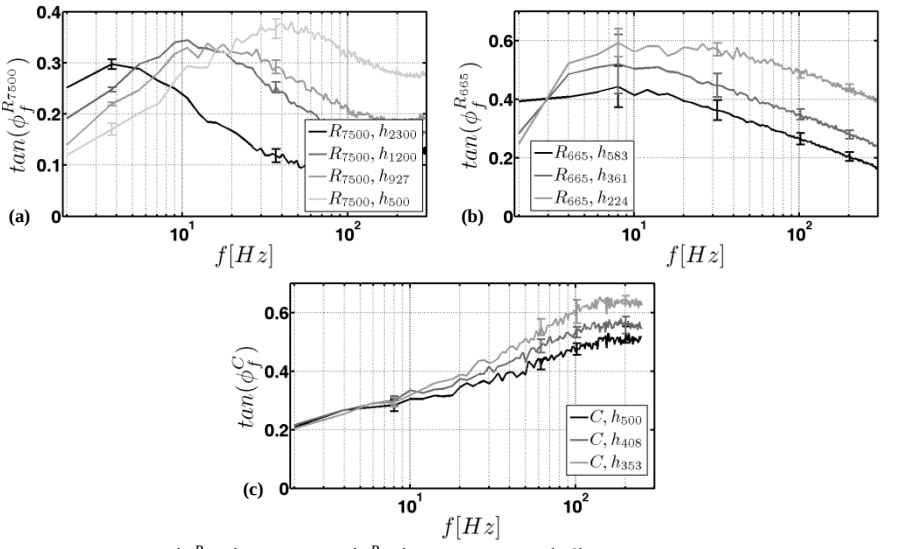

Figure 4.2: (a) $tan(\emptyset_f^{R_{7500}})(f)$, (b) $tan(\emptyset_f^{R_{665}})(f)$ and (c) $tan(\emptyset_f^{C})(f)$ measured for all the indentation depths analyzed in the study.

Results obtained with the conical indenter exhibit the highest values for both $tan(\phi_f)_{max}$ and f_{max}; moreover, peaks are centered on the same frequency f_{max}, for all the h_s investigated. For the spherical indenters, peaks decrease with the mean indentation depth; comparing the two radii, smaller is the radius higher is the $tan(\phi_f)_{max}$. f_{max} follows the same decreasing trend for the larger sphere whereas it appears almost constant (or slightly decreasing) for the smaller one.

Using Equation (4.2), the reduced storage modulus can be computed for all the indentation depths investigated. The effect of the characteristic length results into a smaller value for the smaller tip throughout the whole range of frequency investigated as presented in Figure 4.3 for the sole spherical tips.

In Table 4.4, experimental data extracted from Figure 4.2 and 4.3 are shown. The attention is focused on the drained $(E'^*(0))$ and undrained $(E'^*(250))$ conditions as

well as on the balance between dissipative and conservative effects ($tan(\emptyset_f)_{max}$) and the characteristic time of the phenomenon investigated (f_{max}): results from all the configurations and indentation depths are presented. The information on $E_c'^*(f = 250\ Hz)$ is not considered since these experimental data are not reliable.

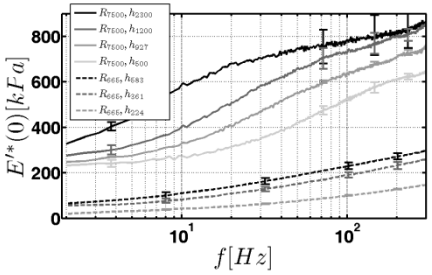

Figure 4.3: $E'^*(f)$ function of the natural frequency f for all the indentation depths investigated with the spherical tips. Solid line: indentation depths investigated with the configuration R_{7500}; dashed line: indentation depths investigated with the configuration R_{665}.

Table 4.4: Overview on the extracted experimental quantities. Drained reduced indentation moduli, undrained reduced indentation moduli, maxima of the tangent of phase shift and frequency of the peak are shown for all the analyses.

SAMPLE	$E'^*(0)$ $[kPa]$		$E'^*(250\ Hz)$ $[kPa]$		$tan(\emptyset_f)_{max}$		f_{max} $[Hz]$	
	mean	*std*	*mean*	*std*	*mean*	*std*	*mean*	*std*
R_{7500}, h_{2300}	264	7	838	45	0.30	0.02	2.9	0.4
R_{7500}, h_{1200}	245	2	820	41	0.34	0.01	6.3	0.3
R_{7500}, h_{927}	228	5	728	18	0.35	0.01	8.1	0.4
R_{7500}, h_{500}	223	17	623	12	0.38	0.03	23.3	1.2
R_{665}, h_{583}	65	10	285	11	0.45	0.07	4.4	1.1
R_{665}, h_{361}	51	8	249	9	0.53	0.10	6	1.6
R_{665}, h_{224}	22	9	139	7	0.62	0.01	5.6	2.6
C, h_{500}	56	6	–	–	0.54	0.01	142	23
C, h_{408}	63	8	–	–	0.60	0.02	152	15
C, h_{353}	61	4	–	–	0.69	0.03	130	10

In Figure 4.4, the value of drained indentation modulus is presented in function of the indentation depth and the characteristic contact length for all the cases analyzed. A clear effect of the characteristic length can be highlighted: indeed, the investigation of similar indentation depth (around $500\ nm$) ends with results that differ from almost one order of magnitude if investigated with tips of different sizes, but it appears to belong to an increasing trend when the dependence on l_c is considered for the sole spherical tips: with the conical one, in fact, results are out of

this trend, even they appear consistent when h_s is chosen as independent variable.

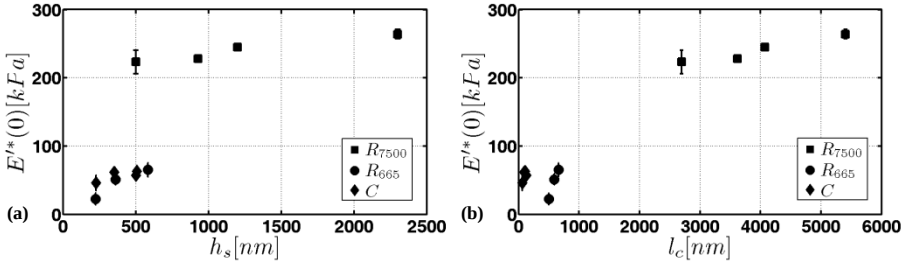

Figure 4.4: $E'^*(0)$ in function of (a) the indentation depth h_s and (b) the characteristic contact length l_c for all the cases analyzed.

The maximum value of the phase shift tangent, measure of the amount of the dissipative effects, follows a clear decreasing dependence with both the indentation depth and the characteristic contact length; it is shown in Figure 4.5.

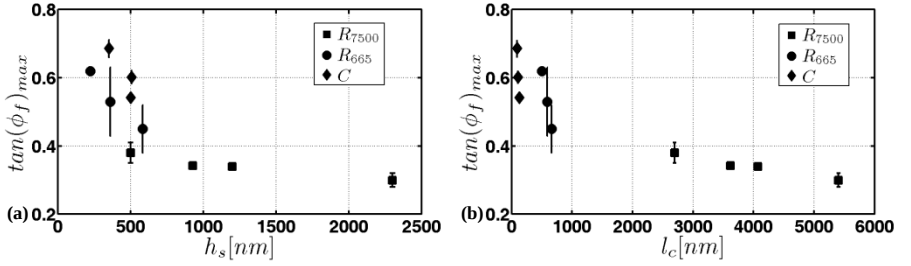

Figure 4.5: $tan(\emptyset_f)_{max}$ in function of (a) the indentation depth h_s and (b) the characteristic contact length l_c for all the cases analyzed.

In Figure 4.6, the variation of f_{max} is presented in relation to the equivalent deformation and the characteristic contact length; in this case, the trend is not so clear. The behavior recorded with the conical tip is very different from the one found using spherical tips.

Closing to the spherical tips, the frequency of the peak seems to decrease with the deformation ϵ_{eq} (as shown in Figure 4.6(a)) but, as highlighted by Figure 4.6(b), the different ranges of contact lengths investigated seems to respond in different ways: f_{max} is almost constant for low l_c, whereas it is decreasing for higher ones, suggesting the presence of a transition in tissue behaviour between these two conditions.

The same transition zone can be found looking at the drained to undrained ratio for the spherical tips: in Figure 4.7, in fact, the trend described by spherical (small spherical tip) and squared (large spherical tip) markers can suggest a change in the same interval of characteristic contact length found above $(1 - 2\ \mu m)$.

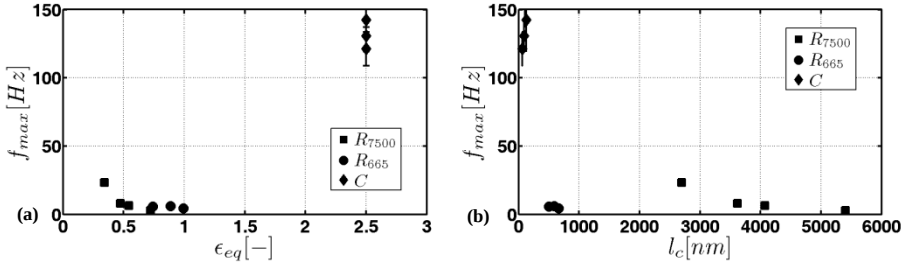

Figure 4.6: f_{max} in function of (a) the equivalent deformation ε_{eq} and (b) the characteristic contact length l_c for all the cases analyzed.

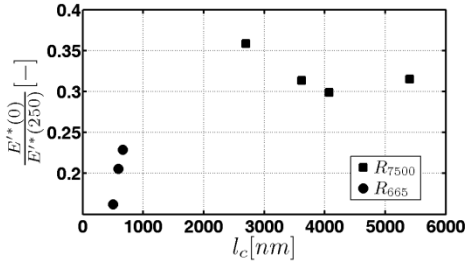

Figure 4.7: $\frac{E'^*(0)}{E'^*(250)}$ in function of the characteristic contact length l_c for all the cases analyzed whit spherical tips.

4.1.4 Discussion

In the present work, the dynamic AFM - based nanoindentation test is used in order to investigate the elastic properties and the time dependent behavior of AC at nanometric and micrometric characteristic lengths by sweeping frequencies ranging from $2\,Hz$ to $250\,Hz$. AC is expected to sustain cyclic or impact loading with frequency components that can be as high as $1\,kHz$ (Lee , et al., 2010) (Grodzinsky, Roth, Myers, Grossman, & Mow, 1981). AC is investigated in the proposed frequency range in order to avoid artifacts due to the bandwidth of the piezoelectric AFM scanner. According to the work of Dintwa (Dintwa, Tijskens, & Ramon, 2008), the use of an elastic framework to analyze the measures is justified.

The effect of the characteristic lengths on AC has been already highlighted in the work of Simha (Simha, Jin, Hall, Chiravarambath, & Lewis, 2007): he performs indentation tests on bovine patellar cartilage using flat-ended conical or cylindrical tips with end diameters ranging from $5\,\mu m$ to $4\,mm$. These results show that the elastic modulus remains constant, around $0.8\,MPa$ if the tips size is greater than $2\,mm$ and increases when the tip size is smaller and smaller, up to the $2.5\,MPa$ in the case of the smallest tip analyzed. In this work, two spherical tips that differ of one order of magnitude in radius are used in addition with a pyramidal one that ends

with a $20\,nm$ radius: the results seem to be in apparent disagreement with the previous cited references. In Figure 4.4(a), it is shown how the indentation depths investigated with the large spherical tip are greater (from $500\,nm$ up to $2300\,nm$) than the ones analyzed with the smaller tips (from $230\,nm$ to $500\,nm$): hence, except an overlap around $500\,nm$, it could be stated that the differences can be due to the diverse layers investigated. The explanation can be clearer looking at Figure 4.4(b): more than diverse layers, the larger tip investigates characteristic contact lengths that are 4 to 8 times greater than the greatest studied with the smaller ones. The behavior highlighted for the sole drained indentation modulus can be extended to the whole frequency range as shown in Figure 4.3: for both the tips, increasing the averaged indentation depth the storage modulus increases, reaching an almost constant value; comparing the two spherical tips, throughout the whole range of frequency, the storage modulus computed using the larger tips is always 4 to 6 times greater (depending on the averaged indentation depth) than the one computed with the smaller.

According the dimensions of the constituents and their arrangement in the superficial layers of AC as described in the introduction, if the investigation is performed at a characteristic contact length lower than micron, the solicitation inferred by the tip is probably carried out by an arrangement of few macromolecules; a larger contact length, instead, resolves to the investigation of the overall tissue. Therefore the hierarchical structure of AC is here evidenced.

Loparic (Loparic, et al., 2010) uses microindentation and nanoindentation to probe different structures on femoral head of porcine hip. Two tips are used: a spherical one with radius $10\,\mu m$ and a pyramidal one with nominal tip radius $< 20\,nm$; the maximum load is, respectively, $\sim 2\,\mu N$ and $\sim 1.8\,nN$. Results show how the averaged stiffness measured with the larger tip is almost constant through the surface and equal to $1.3 \pm 0.4\,MPa$, whereas two different values can be found with the smaller one, $\sim 22.3\,kPa$ related to proteoglycans and $\sim 384\,kPa$ related to collagen. Values of the storage modulus at drained condition found in this work fit the trend but not the values themself: larger tip measures higher values; the difference in the magnitude can be related to the different tissue (bovine vs porcine) investigated. Microindentation experiments on bovine cartilage sample proposed by Park (Park, Costa, Ateshian, & Hong, 2009) have shown that the indentation tissue modulus range from $10\,kPa$ to $80\,kPa$ for penetration depths up to $600\,nm$. In the work of Han (Han, et al., 2011) the storage modulus in drained condition measured on native AC is equal to $0.22 \pm 0.02\,MPa$ and increases to $0.77 \pm 0.10\,MPa$ to the limit of undrained one; these values are measured at a characteristic length of $\sim 1.5\,\mu m$ without differences between the tips since this quantities remains the same. They agree with the results found in this work using the large tip, evaluated in a range of lengths from $\sim 2.5\,\mu m$ and $\sim 5.5\,\mu m$. It is worth mentioning that, unlike this mismatching work, in the paper of Han the decreasing branch of the tangent of the phase shift is not measured.

The time dependent behavior of AC can be studied looking at two quantities, both related to the tangent of phase shift graph (Figure 4.3): the frequency at which the maximum occurs and the value of the maximum itself.
An high peak is related to a large dissipative effect; on the contrary, a low peak is indicative of a more elastic behavior. Figure 4.5(a) shows how the dissipative effects reduce increasing the mean indentation depth: the trend is clearly followed by all the three tips; the same trend can be noted in dependence of the characteristic contact length in Figure 4.5(b). According to these two graphs, it seems that the tissue reduces its time dependencies if the volume solicited increases: this could be related with the fact that, increasing the length, the effects of the single components vanish, driving toward a more homogeneous elastic material. In Figure 4.3(a), the peaks found for the different mean indentation depths occur at different frequencies; in particular, higher is the mean indentation depth, lower is the frequency at which it occurs. In Figure 4.3(b) and Figure 4.3(c), instead, the position of the peak is independent (almost independent for the small spherical tip) by the mean indentation depth. This difference can be explained looking at the combined poroviscoelastic behavior that characterizes AC: as shown by (Hu, Zhao, Vlassak, & Suo, 2010) the characteristic time with which a viscoelastic gel responds to a time dependent solicitation is independent by the length at which the solicitation is applied; at the contrary, a poroelastic response is. Then, if a dominant poroelastic behavior is investigated with the larger tip, a dominant viscoelastic behavior is evidenced with the smaller ones. Consistently with the discussion performed on parameter $E'^{*}(0)$, at a characteristic contact length lower than micron, the solicitation inferred by the tip is probably carried out by a network of fibrils; the intrinsic viscoelasticity of the filament, or a small network of macromolecules, is the predominant phenomenon investigated. A larger contact length (in this study, a threshold of $2000\ nm$ can be proposed) resolves to the investigation of the overall tissue and the weight of porosities become important. Some differences can be found between the smaller tips: the conical one investigates lengths lower than $500\ nm$ and the spherical one is in between $500\ nm$ and $1\ \mu m$. It can be stated that the response found with the former is directly related to the viscoelastic behavior of the collagen molecules; in the latter condition, instead, a small network of macromolecules plays and the viscoelastic behavior can be referred to the sliding between them (flow independent viscoelasticity), giving a slower effect in terms of both the characteristic frequency of the phenomenon and its magnitude.
The behavior measured with the conical tip is also characterized by an high indentation strain that could help to explain, partially, the high dissipative effect calculated.
The different trends shown by the two spherical tips suggest that a change in the mechanism of response happens at a characteristic length of $1 - 2\ \mu m$. This scale, in fact, can be the one in which the weight of the porosity solicited overcome the viscoelastic effect intrinsically present in the solid network. Indeed, both viscoelastic and poroelastic properties are now explainable looking at the microstructure of AC.

According to the dimensional description, these results can suggest how the characteristic lengths of viscoelastic effects are confined in the range of the dimensions of macromolecules ($[10^{-8} - 10^{-6}\ \mu m]$); the poroelastic effects take place at the scale in which the nanometric porosities are abundantly recruited from the solicitation.

4.2 MULTILOAD NANOINDENTATION CREEP TESTS ON MATURE BOVINE ARTICULAR CARTILAGE

Under the hypothesis that the tissue behaviour is primarily extrinsic (i.e. poroelastic), the response at equilibrium, the short term response and the permeability, are investigated through experiments with different characteristic lengths. The analytical solution to the confined compression of a fluid saturated porous solid (already shown in Chapter 3) is used to provide a quantitative estimation of the time dependent response of AC samples. For comparison purposes, the time dependent mechanical response exhibited by a Polydimethylsiloxane (PDMS) sample subjected to the same nanoindentation loading protocol as that used for AC samples, but in dry environment, is presented as a proof of a purely intrinsic (i.e. viscoelastic) reference response.

4.2.1 Multiload nanoindentation creep experiments

With respect to a classical indentation loading – unloading test, in a multiload nanoindentation test, the prescribed overall load is divided into a given number of steps; then, the sample is loaded with a prescribed loading rate to reach the value of the force corresponding to the first step; after an holding phase, the sample is loaded further to reach the subsequent load level. The procedure is repeated till the achievement of the maximum prescribed indentation load.

In this work, the multiload nanoindentation protocol is combined with a creep analysis: for each step, after the initial loading phase, a holding phase of $120\ s$ is scheduled and a continuous measure of the indentation depth is carried out while the load is kept constant (creep test). After each holding phase, the sample is immediately loaded to the next step.

In Table 4.5, the parameters set for the each test are presented. Two spherical tips are used: $R_{25} = 25\ \mu m$ and $R_{400} = 400\ \mu m$ The experiments with R_{25} have been run with a loading rate of $1\ \frac{mN}{s}$; whereas, the experiments with R_{400} have been run with two different loading rates ($1\ \frac{mN}{s}$ and $10\ \frac{mN}{s}$) in order to assess the influence of this experimental parameter on the measured properties. A suitable number of indentation spots, over which the multiload test is performed, is chosen in order to get statistically relevant results.

For the case of PDMS, instead, the experiments are performed in dry condition using two tips of radii $R_{25} = 25\ \mu m$ and $R_{100} = 100\ \mu m$; Table 4.6 shows the experimental setup for each case

Table 4.5: Parameters for the experiments carried out on the AC samples.

SAMPLE	TIP RADIUS $R\ [\mu m]$	LOADING RATE $v_L[\frac{mN}{s}]$	HOLD PHASE $t_h[s]$	TOTAL LOAD $F_T[mN]$	LOAD STEPS	INDENTATION SITES
$C(R_{400}, v_1)$	400	1	120	1	10	50
$C(R_{400}, v_{10})$	400	10	120	1	10	28
$C(R_{25}, v_1)$	25	1	120	1	10	10

Table 4.6: Parameters for the experiments carried out on the PDMS samples.

SAMPLE	TIP RADIUS $R\ [\mu m]$	LOADING RATE $v_L[\frac{mN}{s}]$	HOLD PHASE $t_h[s]$	TOTAL LOAD $F_T[mN]$	LOAD STEPS	INDENTATION SITES
$P(R_{25}, v_1)$	25	1	120	1	10	10
$P(R_{100}, v_1)$	100	1	120	1	10	10

4.2.2 The solution of 1D confined compression creep problem is adapted to nanoindentation creep test

In this work, the solution to the problem of the surface settlement of a poroelastic material layer resting on a stiff impermeable base subjected to constant surface loading, also regarded as consolidation problem, is taken as a reference solution with the purpose to define a fitting function in the time domain. Although the boundary conditions for nanoindentation and consolidation problems are different, the analytical solution to the one dimensional problem is borrowed with the only purpose to describe the time dependent response of a poroelastic solid subject to a constant load (creep test); the solution is presented in Chapter 3, Equations (3.30) to (3.34). For sake of clarity, Equations (3.33) and (3.34) are reported here again

$$u_3(0,\tau) = u_3^i(0,0) + u_3^t(0,\tau) = \frac{\alpha(1+\nu_d)WLP_0}{3K_d(1-\nu_d)}[1 + g(\tau)] \qquad (4.5)$$

with

$$g(\tau) = \sum_{m=0}^{\infty} \frac{8}{(1+2m)^2\pi^2}\left[1 - e^{-(1+2m)^2\pi^2\tau}\right] \qquad (4.6)$$

where K_d and ν_d are bulk modulus and Poisson's ratio in drained condition and $W = \frac{SC_d(1+\nu_d)}{[3\Lambda(1-\nu_d)+\alpha SC_d(1+\nu_d)]}$; $\alpha = 1 - \left(\frac{K_d}{K_m}\right)$ is the isotropic effective stress coefficient, S the Skempton parameter, $C_d = \widehat{\boldsymbol{U}}^T\widehat{\boldsymbol{S_d}}\widehat{\boldsymbol{U}}$ and Λ is a scalar function of the drained elastic properties of the porous matrix. u_3 indicates the displacement of the top surface; superscrip i indicates the instantaneous response whereas superscript t the transient one.

For the articular cartilage, incompressibility of the constituent material of the porous solid matrix and incompressibility of the wetting fluid have been assumed. Consequently, $\Lambda \to 0$, $\alpha = 1$ and $W = 1$; Equation (4.5) becomes

$$h(0,\tau) = h^i(0,0) + h^t(0,\tau) = \frac{(1+\nu_d)LP_0}{3K_d(1-\nu_d)}[1+g(\tau)] \qquad (4.7)$$

In order to use Equation (4.7) as a phenomenological fitting function for the force-displacement data of nanoindentation tests, h is regarded as the vertical displacement of the tip (in place of u_3) and it has the meaning of indentation depth h_s used in Section 4.1. A new dimensionless time τ is defined in analogy to that introduced by Galli (Galli & Oyen, 2009):

$$\tau = \frac{P_2^j t}{Rh(t=120)} \qquad (4.8)$$

in which, two characteristic lengths of a spherical indentation have been introduced: the radius of the spherical indenter, R, and the displacement at the end of the hold phase, $h(t=120)$. In definition (4.8), P_2^j is a fitting parameter which plays the role of a diffusivity parameter. In the nanoindentation problem, parameter P_2 is proportional to tissue permeability and drained indentation modulus.

Even if the penetration depth does increase during the creep phase, for sake of simplicity only the final penetration is accounted in the definition of τ; for this reason, only creep data showing a creep displacement $(h_{120} - h_0)$ less than 30% of initial displacement (h_0) have been retained.

In order to use Equation (4.7) for multiload nanoindentation creep tests, the displacement history during creep at the *j - th* load level $h^j(\tau)$is described with a two parameters (P_1^j, P_2^j) fitting curve

$$h^j = h^{i,j} + P_1^j g(\tau^j) \qquad (4.9)$$

in which $h^{i,j}$ is the indentation depth at the beginning of the creep phase and $g(\tau^j)$ defined in Equation (4.6), both computed for the *j-th* load level. Parameter $P_1^j(h)[nm]$ is the difference between the displacement in the drained $(t \to \infty)$ and that in the undrained $(t \to 0)$ conditions; $P_2^j(h)\left[\frac{nm^2}{s}\right] = kM_d$, depends on the drained indentation modulus M_d and the permeability k. The superscript *j* indicates the load level considered.

4.2.3 Experimental data analysis

The output data at each load level *j* of the experimental test are:

1. the indentation force F_L^j and the undrained displacement h_u^j. The undrained displacements (h_u^j) at the *j - th* load level F_L^j is obtained as summation of undrained displacement increments: $h_u^j = \sum_{k=1}^{j} \Delta h_u^k(F_L^k)$, in which the undrained displacement increment is $\Delta h_u^k(F_L^k) = h^{i,k} - h^{k-1}(t = 120s)$.
2. The drained indentation depth h_d^j, that represents the tissue response in drained (equilibrium) conditions. It is the indentation depth measured at the end of the *j - th* creep phase, $h_d^j = h^j(t = 120s)$.

3. The time domain data $h_F^j(t)$ which is the displacement history measured for each *j - th* load level during the holding phase.

Figures 4.8 and 4.9 show representative force history and displacement responses collected for the tip radius R_{400}.

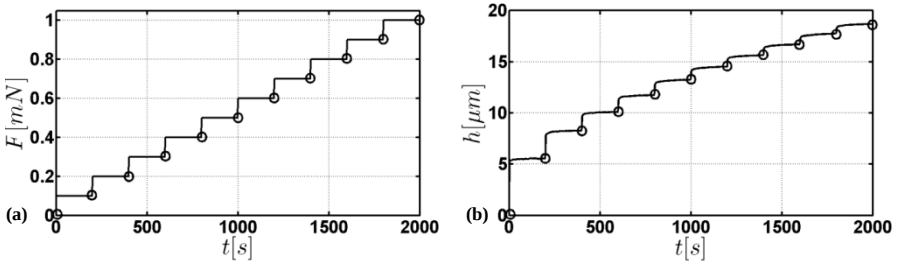

Figure 4.8: (a) Force vs time: ten load steps from 0 mN to 1 mN have been applied with load increments of 0.1 mN; (b) typical displacement in function of time recorded during the whole experiment. Open circles indicate the end of the creep phase at each load level.

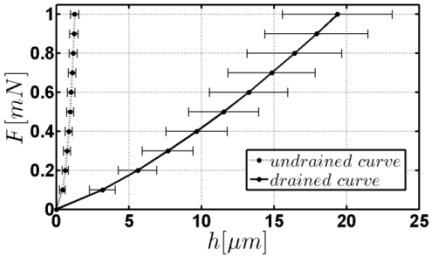

Figure 4.9: Example of drained curve (solid line) and undrained curve (dotted line) for the case $C(R_{400}, v_1)$. The data are presented by their mean values and standard deviations.

Figure 4.10 shows the creep behavior for all the ten levels of the same case presented above, as an example. The time is scaled in the range $[0 - 120]s$ for all the curves.

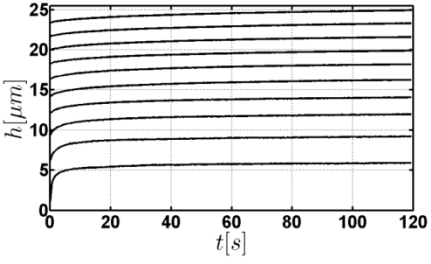

Figure 4.10: Example of creep curves related to the ten increasing loads in the range $[0.1 - 1]$ mN

The theory of the spherical indentation of a purely elastic half - space, based on the Hertzian contact theory (Johnson, 1985), is shown in Equation (3.12). Equation (3.12) can be used to fit the $(F_L - h_d)$ and $(F_L - h_u)$ data points to identify drained (M_d) and undrained (M_u) indentation moduli. To this purpose the following fitting Equations are introduced:

$$F_L = \frac{4}{3} M_d \sqrt[2]{R} h_d^{\frac{3}{2}} \tag{4.10}$$

$$F_L = \frac{4}{3} M_u \sqrt[2]{R} h_u^{\frac{3}{2}} \tag{4.11}$$

where $R = [R_{25}, R_{400}]$ is known. For PDMS samples, the modulus computed using data at the end of the creep phases is the long term modulus $M_{lt} = M(t \to \infty)$.
Applying a best fitting procedure on the experimental curves $h_F^j(t)$ using Equation (4.9), the parameter $P_2^j(h)$ can be identified. By using the definition of $P_2^j(h)$, a value for the depth dependent indentation permeability can be estimated as

$$k_{ind}{}^j(h) = \frac{P_2^j(h)}{M_d} \tag{4.12}$$

In order to highlight the effect of characteristic size of each load level and each indenter tip radius, a suitable normalization of the indenter displacement is introduced, also regarded as consolidation ratio:

$$\overline{h_F^j} = \frac{(h^j(t) - h_d^j)}{(h_u^j - h_d^j)} \tag{4.13}$$

The characteristic contact lengths and the equivalent deformations are computed as expressed in Equations (3.18) and (3.21) using $K_\varepsilon = 1$. In order to discriminate between drained and undrained conditions, these two quantities are rewritten as

$$l_{c,s,k}^j = \sqrt[2]{(2Rh_k^j - h_k^{j\,2})} \tag{4.14}$$

$$\varepsilon_{eq,s,k}^j = \frac{l_{c,s,k}^j}{R} \tag{4.15}$$

where the subscript s indicates spherical indentation and the subscript k indicates drained or undrained condition: in fact, h_k^j is equal to h_0^j in the case of undrained condition and h_∞^j in the case of drained condition.
The above Equations and the best fitting procedures are implemented into the commercial code Matlab (MathWorks, Natick, MA, USA) and the constrained interior-point algorithm is used in a least square framework to find the optimum parameters.

4.3.4 Results on articular cartilage

In Table 4.7, values of both the drained modulus M_d and undrained modulus M_u, identified by best fitting on the load - indentation curves using Equations (4.10) and

(4.11), are presented. The values are shown as mean and standard deviation, both computed over all the repetitions performed under the same conditions. Goodness parameter R^2 is also reported. The drained indentation modulus obtained with the small tip is larger than that obtained with the larger indenter. In particular, drained indentation modulus obtained with the R_{400} tip is about $500\ kPa$ for both the loading rates; whereas a value of $1741 \pm 41\ kPa$ is found with the R_{25} tip. This size dependence is not observed in the undrained modulus. To check the effect of the loading rates, experiments are carried out on cartilage samples with the larger tip ($C(R_{400}, v_1)$ and $C(R_{400}, v_{10})$) at two different rates: $1\ \frac{mN}{s}$ and $10\ \frac{mN}{s}$. As expected, a significant effect is found on the undrained response whereas no statistical difference was found on the equilibrium (drained) response. In all cases, undrained moduli are significantly higher than the drained ones.
Figure 4.11 shows the same data of Table 4.7 as an histogram: Figure 4.11(a) reports the drained modulus whereas Figure 4.11(b) to the undrained one. The black bars indicate the standard deviation of each value.

Table 4.7: Values of M_d and M_u for AC sample as mean value and standard deviation.

SAMPLE	DRAINED MODULUS $M_d\ [kPa]$			UNDRAINED MODULUS $M_u\ [kPa]$		
	mean	std dev	R^2	mean	std dev	R^2
$C(R_{400}, v_1)$	498	152	0.99	40	8	0.99
$C(R_{25}, v_1)$	1741	41	0.98	25	1	0.99

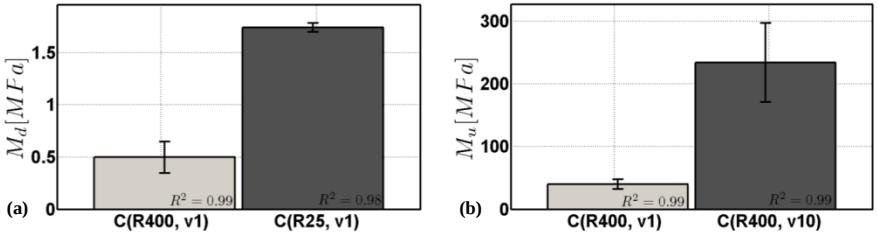

Figure 4.11: (a) Drained moduli for the cases of different tips and same loading rate; (b) Undrained moduli for the cases of same tip and different loading rates. Mean and standard deviation are presented.

In order to highlight the effect of the length scale at which the experiment is carried out, the dependence on the indentation strain and on the contact radius is accounted for. Figure 4.12 and Figure 4.13 present, respectively, the drained and undrained moduli as a function of the equivalent deformation (graphs 4.12(a) and 4.13(a)) and the contact radius (graphs 4.12(b) and 4.13(b)). For each value in the plots, mean and standard deviation (vertical line) are reported; the horizontal lines indicate the maximum and minimum deformation / contact radius achieved during the multiload experiments. An increasing indentation modulus is found for increasing

representative equivalent deformation; on the contrary, a decreasing modulus is found for an increasing characteristic length.

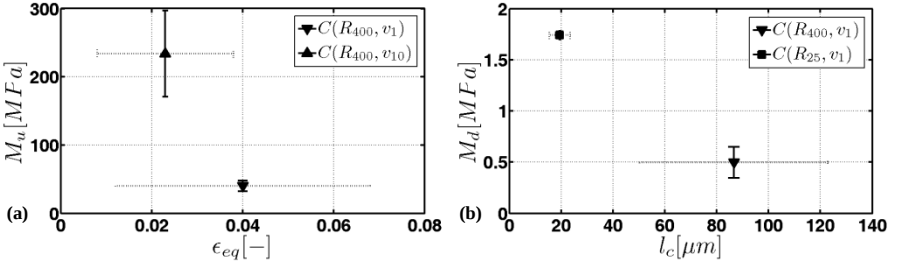

Figure 4.12: (a) Drained moduli vs equivalent deformation; (b) Drained moduli vs contact radius. Mean (marker) standard deviation (solid line) are presented as well as the range of both the parameters analyzed into a single multiload test (dotted line). Only tests carried out at the same loading rates are reported.

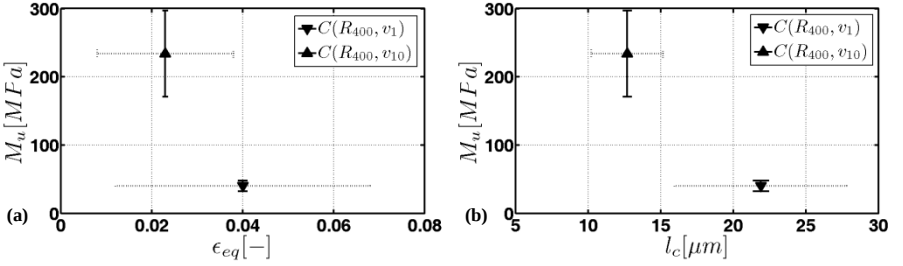

Figure 4.13: (a) Undrained moduli vs equivalent deformation; (b) Undrained moduli vs contact radius. Mean (marker) standard deviation (solid line) are presented as well as the range of both the parameters analyzed into a single multiload test (dotted line). Only tests carried out at the same loading rates are reported.

Figure 4.14 reports the values of indentation permeability (mean and standard deviation) computed as a function of the equivalent deformation (Figure 4.14(a)) and characteristic length (Figure 4.14(b)) for all load levels.

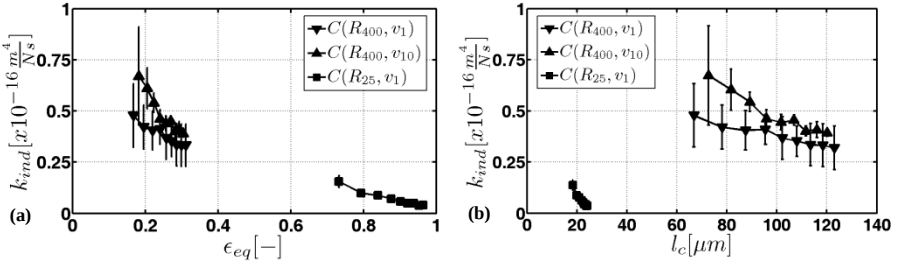

Figure 4.14: (a) Indentation permeability with respect to the equivalent deformation; (b) indentation permeability with respect to the contact radii. Mean (marker) and standard deviation are presented.

A decreasing permeability is found with increasing representative indentation strain; whereas, permeability is greater at larger characteristic lengths.

4.3.5 Results on PDMS

Table 4.8 shows the values of the long term indentation modulus calculated for the PDMS samples.

Table 4.8: Values of M_{lt} for PDMS samples as mean value and standard deviation.

SAMPLE	LONG TERM MODULUS M_{lt} $[MPa]$		
	mean	std dev	R^2
$P(R_{25}, v_1)$	3.77	0.08	0.983
$P(R_{100}, v_1)$	3.72	0.07	0.991

It is worth to be noted that the long term response for PDMS is independent of the indenter radius.

4.3.6 Time dependent response of AC and PDMS samples under nanoindentation

Figure 4.15(a) reports the consolidation ratio for ten representative levels of load using the R_{400} tip. For each level of load, the total indentation force is distributed over a contact area that increases with the force; thus, each load level is characterized by a specific characteristic size (i.e. the radius of the contact area). As expected from a fluid filled solid under a constant load, the consolidation rate is greater for smaller characteristic sizes; i.e. for increasing levels of the load, the contact area increases and the time required to achieve a given consolidation ratio increases as well.

The characteristic size of the indentation can be changed by changing the tip radius. In Figure 4.15(b), the consolidation ratio is reported for ten levels of load, using the R_{25} tip. The time response under multiload creep is qualitatively similar to the response obtained with the larger tip; consolidation is considerably faster for small tip with respect to that observed with the large tip as shown in Figure 4.15(c). Following the theoretical solution of the consolidation problem, the $\overline{h_F^j}$ becomes independent from the characteristic size if the normalized time $\bar{t}^j = t\frac{P_2^j}{Rh^j{}_{(t=120s)}}$ is considered. To this purpose, the diffusivity parameter P_2^j identified by the curve fitting procedure is used. R^2 values found for all curves fitting the creep data ranged between 0.8 and 0.99 for the large tip radius and between 0.7 and 0.95 for the small radius tip. If consolidation curves are reported as a function of normalized time for all the load levels and for all tip radii, no appreciable difference can be observed; in Figure 4.15(d), the consolidation curves for all the studied cases overlap. This result indicates that the displacement risen under constant load is mostly owed to the

poroelastic dissipation mechanism.

As a comparison, Figure 4.16 shows the time dependent response to a constant indentation load for PDMS in dry condition: the normalized consolidation rate $\overline{h_F^J}$ as a function of the natural time overlaps within the experimental scattering for all characteristic lengths; this shows that, for PDMS, the time dependent phenomenon is independent on the contact radius of the experiment. It can be then speculated that indentation on PDMS in dry condition is mostly an intrinsically viscoelastic phenomenon. Also in this case, only few representative curves are presented.

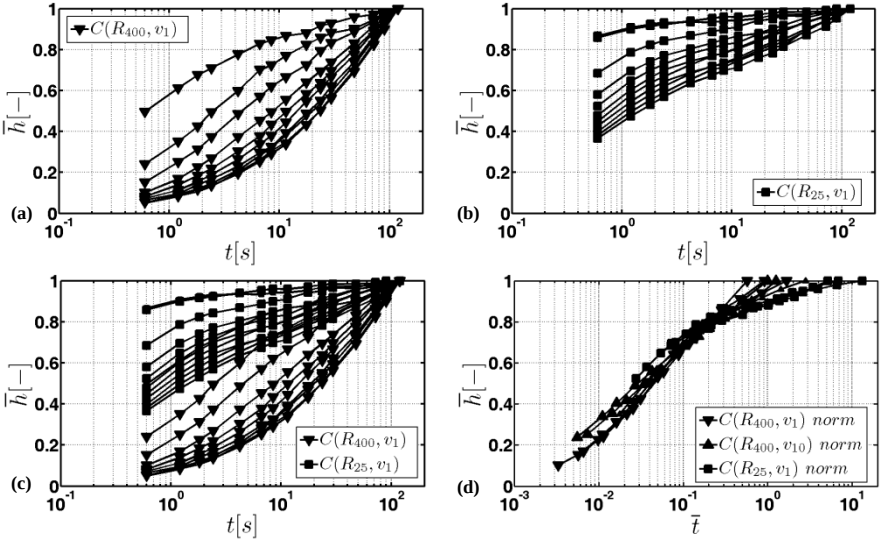

Figure 4.15: (a) Consolidation ratio curves for a representative 10 load levels for the experiment $C(R_{400}, v_1)$ in function of natural time. (b) Consolidation ratio curves for a representative 10 load levels for the experiment $C(R_{25}, v_1)$ in function of natural time. (c) Curves in (a) and (b) are plotted together. (d) Selected consolidation ratio curves in dependence of normalized time for all the three cases analyzed for AC samples.

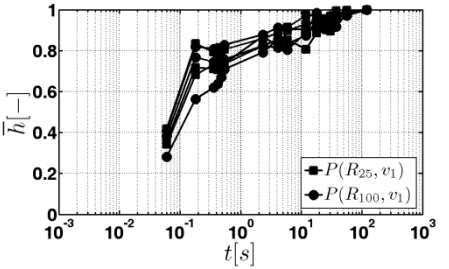

Figure 4.16: Normalized indentation depth plotted in dependence of natural time for PDMS samples. For the different tip radii and loading condition, only representative curves are presented.

4.2.6 Discussions

The complex behavior of the superficial layers of the AC derives from the spatial organization in which the different constituents are arranged (Jurvelin, et al., 1996). In this work, the attention is focused on the effect of the characteristic length of the nanoindentation experiment on the time dependent response of AC in a physiological (i.e. liquid) environment. The analyses allow identifying both drained and undrained indentation moduli as well as permeability. Characteristic lengths are investigated by performing nanoindentation experiments with spherical tips with two different radii and with different penetration depths obtained by setting multiple levels of load.

In terms of elastic properties, the value of drained modulus is three times higher in the case of the smaller tip ($R_{25} = 25\ \mu m$) than in the case of larger one ($R_{400} = 400\ \mu m$). A comparatively smaller decrease, of about 50%, can be observed for the undrained modulus, instead, with an opposite trend. This effect has already been pointed out in the work of Simha (Simha, Jin, Hall, Chiravarambath, & Lewis, 2007) in which the drained indentation modulus, measured on bovine patella cartilage, decreases up to three times (from $4.5\ MPa$ to $1.5\ MPa$) when the radius of curvature of a conical tip increases from $0.1\ mm$ to $1\ mm$. Simha concludes that the indentation modulus is dependent on the indenter radius due to the spatial heterogeneity of the volume fraction of collagen fibrils and their orientation distribution as well as to the different amount of AC tissue involved with different tip size. Further considerations can be done by introducing the equivalent deformation and the contact radius in the data analyses. The experiments carried out with the small tip cover a wide range of high equivalent deformations ($\varepsilon_{eq} \in [0.61 - 0.96]$) and small characteristic contact sizes ($l_c \in [15 - 23]\ \mu m$); vice versa, those conducted with the large tip investigate a range of smaller equivalent deformations ($\varepsilon_{eq} \in [0.12 - 0.31]$) with large contact sizes ($l_c \in [50 - 125]\ \mu m$). According to Figures 4.12, the drained indentation modulus (measure of the elastic properties of the solid matrix in AC) increases with the equivalent deformation applied, as seen at macroscale with unconfined compression (Li, Buschmann, & Shirazi-Adl, 2003), and decreases with the increasing contact radius. Merging the two results, the following explanation can be suggested: the drained modulus increases if smaller volume of tissues (namely, a smaller amount of collagen fibrils) are recruited and loaded at high strains unlike the activation of a high number of collagen fibrils loaded at low strains, suggesting a size dependence of the elastic response given by tissue heterogeneity. In the work of Bonnevie (Bonnevie, Baro, Wang, & Burris, 2012), the drained modulus is measured using a spherical tip of $3.2\ mm$ pressed into the sample to reach indentation depths in the range $[22 - 140\ \mu m]$: they have shown that for indenter tip greater than $1\ mm$ in radius, the drained modulus is fairly constant, as confirmed by the work of Korhonen (Korhonen, et al., 2002). Hence, by increasing the length at which the analysis is performed, the AC is better approximated as a homogenous medium.

The value of the undrained modulus increases substantially if the loading rate increases, as expected and evidenced in the histogram in Figure 4.11(b) (result on sample $C(R_{400}, v_1)$). Comparing the cases having the same rate and different tip radius, the undrained modulus is slightly affected by the equivalent deformation: indeed, if the loading conditions are such that the volumetric load is completely sustained by the physiological fluid, no dependence on tip radius can be evidenced.
The high values of the R^2 found in all the cases show that the hypothesis of Hertzian contact is acceptable for both the drained and undrained moduli (Dintwa, Tijskens, & Ramon, 2008) for which a purely elastic behavior can be expected.
In this study, the penetration depths of all experiments are lower than $25\ \mu m$. It is reasonable to consider that through - the - thickness inhomogeneity plays no relevant role in such small amount of material. The capability of nanoindentation to probe small amount of materials (unlike compression tests on large samples) and, in particular, to analyze thin superficial layers, is one of the key features of this specific experimental technique. Inhomogeneous material properties can be probed by making nanoindentation on different sites on the sample; through – the - thickness inhomogeneity of articular cartilage can be probed by slicing tissue sample at different depths or making cross - section indentations.
Anisotropy is also an important issue on cartilage mechanics. It is well known that superficial layers exhibit in - plane Young's modulus (or stiffness, for more generally non - linear material response) higher than that along the thickness direction. This peculiar property is owed by the collagen fibrils orientation distribution which, on superficial layers, has the predominant direction parallel to the articulating surface. In this work, the indentation parameter which account for tissue stiffness is the indentation modulus (M). Theoretical solutions to the problem of indentation on elastic anisotropic materials show that the indentation modulus is a known function of the elastic tensor components (see for example the work of Delafargue (Delafargue & Ulm, 2004)). For isotropic materials this relationship reduces to $M = \frac{E}{1-\nu^2}$; in this definition, E is the Young's modulus and ν is the Poisson ratio. As in the work of Hu (Hu, Zhao, Vlassak, & Suo, 2010), where phenomenological estimations are proposed, a one dimensional problem is here considered; in this case, moreover, the analytical solution is borrowed from a one dimensional consolidation problem and it allows an estimation of the tissue indentation permeability at different equivalent indentation strains. In the cases analyzed in Figure 4.14(b), all the curves show a decreasing trend. More interesting are the results in Figure 4.14(a): matching the results from the two tips, it is clear that the permeability of the tissue is lower for higher equivalent deformations. In particular the permeability as a function of the equivalent indentation strain can be fitted with a function of strain (Ateshian, Warden, Kim, Grelsamer, & Mow, 1997)

$$k_{ind}(\varepsilon) = k_0 e^{-k_1 \varepsilon} \tag{4.16}$$

where k_0 and k_1 are two fitting parameters. Figure 4.17 shows the result of the best

fitting procedure, where $k_0 = 1x10^{-16}\ \frac{m^4}{Ns}$ and $k_1 = 3.06$.

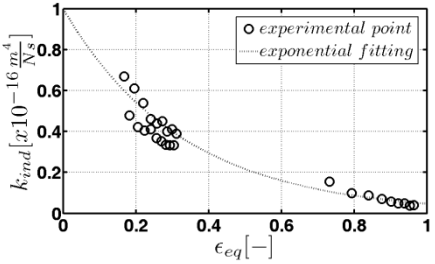

Figure 4.17: Permeability in function of the deformation. The dot line is the best fitting found using the exponential relation in Equation (4.16).

Nia (Nia, Han, Li, Ortiz, & Grodzinsky, 2011) finds an average permeability of $10^{-14}\ \frac{m^4}{Ns}$ on immature bovine cartilage samples by a dynamic AFM - based nanoindentation; whereas, Chen (Chen, Bae, Schinagl, & Sah, 2001) computes a permeability extrapolated at zero compressive strain of $4.55x10^{-14}\ \frac{m^4}{Ns}$ on superficial layers of adult bovine cartilage samples using confined compression experiments. Furthermore, Williamson (Williamson, Chen, & Sah, 2001) shows that tissue permeability is strain dependent (values are in the range $10^{-15} - 10^{-17}\ \frac{m^4}{Ns}$ for compressive strain ranging from 0.15 to 0.45) as well as age - dependent, finding decreasing permeability with tissue age, especially at large strain. Williamson has also found positive correlations between permeability and constituent concentrations. The creep nanoindentation technique presented in this paper predicts tissue permeability which is lower than that found by Nia and Chen; however, experimental conditions and tissue sources should be carefully accounted for when making consistent comparisons between tissue permeability measures. Confined compression tests induce a uniaxial fluid flow along the thickness direction with a flowing path length of the order of the sample thickness. Indentation tests, instead, induce a multiaxial flow of water with a fluid path which is of the order of the contact radius. This is a substantial difference that may well justify the different permeability estimates. In one dimensional consolidation the characteristic length is the sample thickness; for nanoindentation problem, it can be assumed that the characteristic length $\widetilde{l_c}$ is proportional to the contact radius l_c through a proportionality constant β.

$$\widetilde{l_c} = \beta l_c \tag{4.17}$$

Therefore, the normalized time in Equation (4.8) can be rewritten as

$$\tau = \frac{P_2 t}{\beta^2 Rh(t=120)} \tag{4.18}$$

A multiload nanoindentation creep tests is simulated on an isotropic elastic material (Young's modulus $E_i = 1.3\,MPa$ and Poisson's ratio $\nu_i = 0.3$) with homogeneous and strain - independent permeability $k_i = 10^{-16}\frac{m^4}{Ns}$. Five load levels are simulated, $[0.1 - 0.5\,mN]$, with both the tips presented in this work, R_{25} and R_{400}. The creep curves, five for each tip, are fitted by using Equation (4.9) and parameter P_2 can be extracted for each of them; the goodness of the fitting is represented by an $R^2 \sim 0.97$. Consistently with the analytical prediction (Equation (3.12)), the drained modulus estimated using Equation (4.10) is equal to $1.5\,MPa$ for both the tips. Parameters P_2 remains constant throughout the loads in both the cases, in agreement with the tissue homogeneity, with mean values of 31.2 $\frac{\mu m^2}{s}$ and 28.1 $\frac{\mu m^2}{s}$ for R_{400} and R_{25}, respectively. Parameter β can be estimated from P_2 and M_d, since k_i is known and k_{ind} is extracted as in Equation (4.12). Indeed

$$\beta = \sqrt[2]{\frac{k_i}{k_{ind}}} \tag{4.19}$$

and two values are found: $\beta_{25} = 2.3$ and $\beta_{400} = 2.2$; it appears that this proportional parameter is almost constant with the tip radius.

The comparison with literature data shows that the proposed experimental technique still needs to be validated as a toll to determine permeability of the superficial layers of articular cartilage; nevertheless, it has been proven that it can offer an insight in the poroelastic response of the tissue at small scale. The validation for tissue permeability will imply a thorough comparison among different techniques with the same tissue source, harvesting location as well as testing condition. In particular, it is worth to investigate whether permeability assessment through the time domain nanoindentation used in the present work and the frequency domain nanoindentation are somewhat related.

The results presented suggest that the overall behavior related to the porosity is not affected by the characteristic length of the test but it is dependent on the applied deformation only, at least in the range of sizes explored in this study. Further studies exploring a wider size range are required to identify the characteristic length range of validity of this theory.

The time dependent response is recorded over a time span of 120 seconds. The choice of the $120\,s$ of holding time is a compromise between the total duration of the whole experiment session and the necessary condition of achieving an equilibrium configuration (total dissipation of the excessive pore pressure). In order to check the achievement of a steady state configuration at a good level of accuracy, the numerical derivative of the creep displacement as a function of time has been computed as shown in Figure 4.18 for the sole mean curves in any case. It has been found that, for all experimental types (both the tip radii), a negligible time derivative (steady state) has been recorded after less than $20\,s$. A further argument to support this choice can be found by considering the function $g(\tau)$, introduced in Equation

(3.34) as a summation of exponential terms, the dominant contribution of which is given by the first one: $\frac{8}{\pi^2}\left[1-e^{-\pi^2\tau}\right]$. For a tip radius $R=400\mu m$, tissue permeability $k=5x10^{-17}\ \frac{m^4}{Ns}$ and a drained indentation modulus $M_d=500\ kPa$ (the case having the longest characteristic time), this term corresponds to a characteristic time of $\sim 40\ s$, which is about 3 times lower than total duration of the creep phase. In conclusion, for this specific tissue properties (tissue stiffness and permeability) and characteristic indentation length, all characteristic times are substantially lower than $120\ s$.

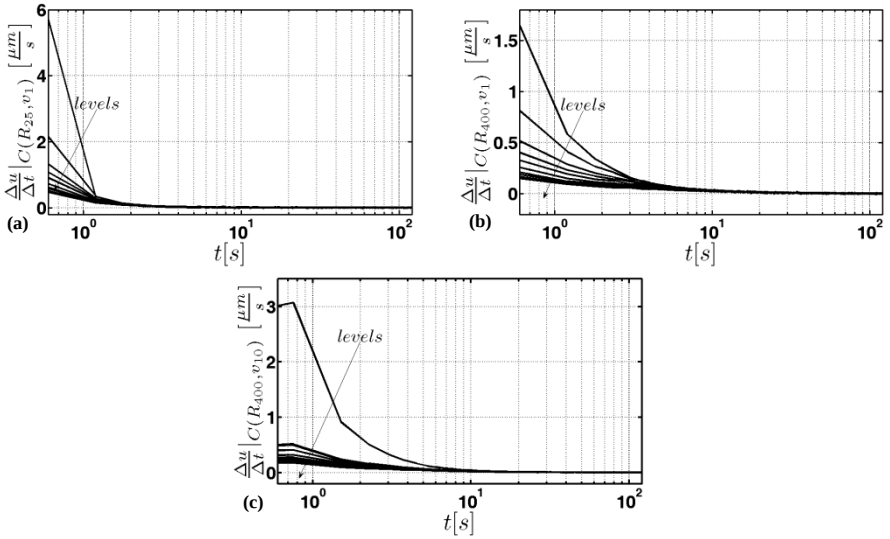

Figure 4.18: Numerical derivative computed for the mean curves obtained from sample (a) $C(R_{25},v_1)$, (b) $C(C_{400},v_1)$ and (c) $C(R_{400},v_{10})$.

For comparison purposes, the same experimental protocol has been applied on PDMS samples in dry conditions which is expected to be homogeneous and intrinsically viscoelastic. Table 4.8 evidences that no statistical differences (p-value from the t-test equal to 0.38) on drained indentation moduli can be found between the experiments with different tip radii ($R_{25}=25\ \mu m - R_{100}=100\ \mu m$). Figure 4.16 shows that PDMS has a prevalent viscoelastic behavior: indeed, normalized creep curves (normalized displacement vs natural time) obtained at different indentation loads overlap, i.e. do not exhibit size dependence. This result has been experimentally proved also by Hu (Hu, Chen, Whitesides, Vlassak, & Suo, 2011)
Unlike the PDMS, the time response of cartilage can be explained through the poroelastic dissipation mechanism. Indeed, Figure 4.15 suggests that poroelasticity is the main phenomenon governing AC in superficial zone. In the figure, the size dependence induced using two different tip radii and different penetration depths is

shown by plotting normalized displacement vs natural time. If the normalized displacement is plotted against the normalized time, by using normalization rule introduced in Equation (4.8), all curves overlap (size dependence disappears) as suggested by the analytical solution of a poroelastic problem. This result supports the initial hypothesis that poroelasticity is the main dissipation mechanism at least at the time scales investigated in this study.
It can be expected that intrinsic viscoelastic behavior of collagen fibrils as well as of the other molecular components of cartilage solid matrix may also play a role. However, as the typical fibril diameter is $30 - 80\,nm$, viscous dissipation should be detectable for characteristic sizes much smaller than those investigated in this work and on larger time scales. It can be speculated that AFM - based indentation using a sharp tip radius and low applied loads may be suitable to probe the viscoelastic response of the fibrillar component: indeed, it has been shown in Section 4.1
The newly gained knowledge that can be achieved through the technique proposed in this work that operates at the microscale, combined with AFM - based technique operating at a lower scale level will be also critical in the development of novel diagnostic tools for cartilages pathology as these properties are important indicators to relate alteration in the tissue mechanical properties to its molecular structural changes: Section 4.3 provides an interesting example.

4.3 MULTILOAD NANOINDENTATION CREEP TESTS ON PORCINE ARTICULAR CARTILAGE: A COMPARISON BETWEEN HEALTY AND ENGINEERED TISSUES

This Section describes the results of a collaboration with the Istituto Ortopedico Galeazzi based on the comparison of mechanical properties between native porcine AC and engineered porcine AC to evaluate cartilage repair when a lesion is healed in different engineered constructs.
In Table 4.9 the samples are presented: control samples are not subjected to zonal differentiation, so all the measures are summarized under a sole sample C_s, whereas the engineered ones are, since different treatments are considered.

Table 4.9: List of porcine samples under investigation.

CONTROL SAMPLE	ENGINEERED SAMPLES	
	NAME	DESCRIPTION
C_s	$E_{s,PL}$	Proximal Lateral sample. Scaffold and autologous Adult Stem Cell (ASC)
	$E_{s,PM}$	Proximal Medial sample. Only scaffold
	$E_{s,DL}$	Distal Lateral sample. Empty

A brief description of the engineered tissues is required: sample

$E_{s,PL}$ is extracted from a zone in which, after the injury is created, the scaffold is implanted together with stem cells of the same animal that can differentiate during the growth; sample $E_{S,PM}$ contains only the scaffold and no stem cells; in sample $E_{S,DL}$ the injury is left evolving without any insertion of scaffold or cells. The multiload nanoindentation creep test are performed using the two tips, $R_{25} = 25\ \mu m$ and $R_{400} = 400\ \mu m$, at a single loading rate of $1\ \frac{mN}{s}$. The hold phase is always $120\ s$ long. In Table 4.10 the parameters set for each experiment are shown

Table 4.10: Parameters for the experiments carried out on porcine samples.

SAMPLE	TIP RADIUS $R\ [\mu m]$	TOTAL LOAD $F_T[mN]$	LOAD STEPS	INDENTATION SITES
$C_s(R_{25})$	25	0.9	0.1	8
$C_s(R_{400})$	400	1	0.1	6
$E_{s,PL}(R_{25})$	25	0.7	0.1	3
$E_{s,PL}(R_{400})$	400	1	0.1	4
$E_{s,PM}(R_{25})$	25	1	0.1	4
$E_{s,PM}(R_{400})$	400	1	0.1	4
$E_{s,DL}(R_{25})$	25	0.3	0.1	5
$E_{s,DL}(R_{400})$	400	0.6	0.1	4

The total load reached is not fixed to $1\ mN$ for all the experiments due to the softness of some samples; in those cases, the maximum indentation depth equal to $24\ \mu m$ imposed by the instrument used is the first condition achieved.

4.3.1 Results on porcine articular cartilage

Data of all the samples are analyzed to extract the drained modulus M_d, and the time dependent properties: the permeability k, if M_d can be correctly extracted; parameter P_2, otherwise. The whole procedure has been already presented in Section 4.2 on bovine samples: results permit to infer about mechanical properties of the three methodologies with respect to control sample. In Table 4.11 the values of the drained modulus are shown for all the cases under the hypothesis of Hertzian contact. As for bovine samples, smaller tip resolves to higher values.

Table 4.11: Values of M_d for all the porcine samples as mean value and standard deviation.

SAMPLE	DRAINED MODULUS $M_d\ [kPa]$		
	mean	std dev	R^2
$C_s(R_{25})$	603	199	0.99
$C_s(R_{400})$	238	68	0.98
$E_{s,PL}(R_{25})$	545	96	0.99
$E_{s,PL}(R_{400})$	272	29	0.99

SAMPLE	DRAINED MODULUS M_d $[kPa]$		
	mean	std dev	R^2
$E_{s,PM}(R_{25})$	268	102	0.92
$E_{s,PM}(R_{400})$	110	10	0.90
$E_{s,DL}(R_{25})$	292	47	0.88
$E_{s,DL}(R_{400})$	81	25	0.86

In Figure 4.19, the same information is presented as histograms to better visualize it. Star indicates that the hypothesis of Hertzian contact is not verified: value of R^2 is, in fact, quite small; the tissue does not behave as an elastic medium and the estimated M_d is, in these cases, not representative of drained modulus.

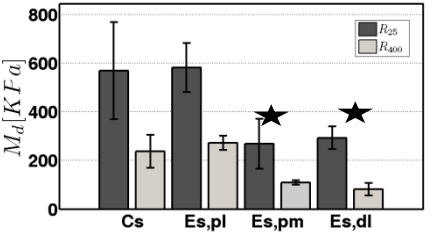

Figure 4.19: Drained modulus computed for all the samples and for both the tips considered

Since the hypothesis of Hertzian contact is not verified for samples $E_{s,PM}$ and $E_{s,DL}$, their proposed drained modulus is no more than a rough estimation of their elastic properties; then, Equation (4.12) can be properly used only for samples C_s and $E_{s,PL}$. Therefore, a first comparison on the different tissues is done on parameter P_2 that condenses the poroelastic properties. Further on, only the mean curves and the mean values are considered, for sake of simplicity.

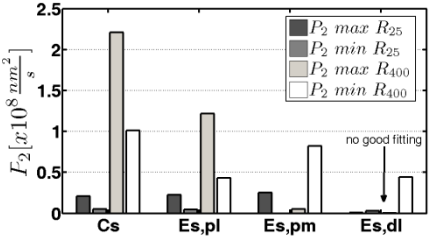

Figure 4.20: Parameter P_2, in term of maximum and minimum values found with both the tips, is shown for all the four cartilage samples

Parameter P_2 shows a decreasing trend with respect to the indentation depth; in

Figure 4.20, for any sample, the maximum value (first load level) and the minimum one (last load level) are shown for both the tips used. The poroelastic fitting is not good for sample $E_{s,DL}$, whereas sample $E_{s,PM}$ shows an opposite trend (P_2 increases with depth) when investigated with the larger radius. Sample $E_{s,PL}$, indeed, is in good agreement with the control one.
Consistent values for the indentation permeability can be computed for the samples C_s and $E_{s,PL}$ when investigated with both the tips. Then, in Figure 4.21 the trend of permeability with respect to the equivalent deformation is presented for both the samples. Sample $E_{s,PL}$ appears a little less permeable at smaller deformation.

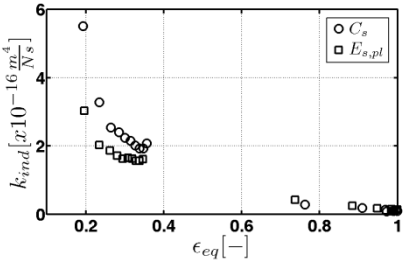

Figure 4.21: Indentation permeability in function of the deformation in the case of control sample (circles) and engineered sample $E_{S,PL}$ (squares).

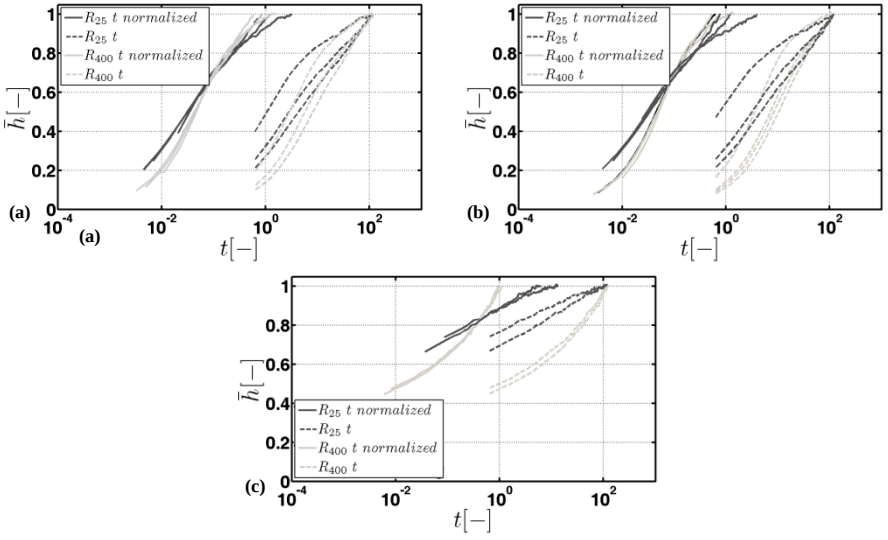

Figure 4.22: (a) Consolidation ratio curves for representative load levels for the experiment on C_S sample in function of natural time (solid lines) and normalized time (dashed lines). (b) Consolidation ratio curves for representative load levels for the experiment on $E_{S,PM}$ sample in function of natural time (solid lines) and normalized time (dashed lines). (c) Consolidation ratio curves for representative load levels for experiments on $E_{S,PL}$ sample in function of natural (solid lines) and normalized (dashed lines) time

Finally, using the normalization of the time proposed in Equation (4.8), the poroelastic hypothesis is checked. In Figure 4.22 selected curves are presented for the sample C_s (Figure 4.22(a)), $E_{s,PL}$ (Figure 4.22(b)) and $E_{s,PM}$ (Figure 4.22(c)) for both the two tips. In each graph, the selected curves are shown with respect to natural time t and normalized time $\bar{t}$. As expected, a complete overlap between creep curves collected at different load and different tip radii is found for the control sample. In the case of sample $E_{s,PL}$ the overlapping is good enough to consider the material governed mainly by poroelasticity whereas sample $E_{s,PM}$ shows a more complex behavior. Curves collected at different depths overlap within the same tip when normalized time is used; between the tips, instead, the overlapping does not occur. No data are presented for the sample $E_{s,DL}$ since no acceptable poroelastic fitting can be found.

4.3.2 Discussion

The methodology proposed in Section 4.2 is here used to evaluate three different engineered tissues. A lesion is get on articular cartilage of minipig animals and it is treated with: scaffold and cells (sample $E_{s,PL}$); scaffold without cells (sample $E_{s,PM}$); neither scaffold nor cells (sample $E_{s,DL}$). Native sample, that represents the healthy condition of porcine AC, is used as comparison. Drained modulus and permeability (parameter P_2, more in general) are chosen as quantities to be compared.

No comparison is performed based on the concepts of characteristic contact lengths and equivalent deformations since almost all the tests reach the maximum depth of $24\ \mu m$, giving approximately l_c up to $147\ \mu m$ and $24\ \mu m$ and ε_{eq} up to 0.36 and 0.99 for R_{400} and R_{25}, respectively.

With reference to the control sample, the values found are in agreement with the literature, suggesting again that the procedure is suitable to extract mechanical parameter for soft tissues. Testing porcine cartilage, Loparic (Loparic, et al., 2010) finds a drained modulus of $1.3 \pm 0.4\ MPa$ using a spherical indentation with a tip radius equal to $10\ \mu m$: according with its increasing trend while the radius decreases, $M_d = 603 \pm 199\ MPa$ for the smaller tip and $M_d = 238 \pm 68\ MPa$ for the larger appear consistent values. In his work, Franke (Franke, et al., 2007) measures a reduced modulus of $2 \pm 0.3\ MPa$ using a Berkovich tip and applying a load of $2.5\ mN$. These last results are also found in agreement with the following paper (Franke, Goken, Meyers, Durst, & Hodge, 2011) in which porcine cartilage is tested by the use of dynamic test with a Berkovich tip. Even if the averaged maximum indentation depth is comparable with the $24\ \mu m$ reached in this study, the load applied is more than two times higher than the one used in this work as well as the deformation. Using different loading conditions on a complex hierarchical structure can explain the differences on the values found.

As expected from its preparation, sample $E_{s,PL}$ better replicates the properties of native cartilage with respect to drained elastic properties, overall elastic behavior and permeability: indeed, Hertzian hyphotesis is verified, like in the case of native

sample. In particular, it has almost the same indentation modulus, with both R_{400} and R_{25}, whereas the permeability appears slightly smaller than control condition for low levels of deformation. Furthermore, this last consideration is supported looking at Figure 4.22(b): applying the time normalization, curves overlap within the same tip radius whilst, between the tips, the same occurs only in an *averaged* way.
Samples $E_{s,PM}$ and $E_{s,DL}$, instead, show comparable estimations (Herzian contact not verified) of drained elastic properties between themself but two or three times lower than the control. Figure 4.20 suggests how poroelastic properties are absolutely not comparable with the target: $E_{s,PM}$ is characterized by an increasing trend for parameter P_2if investigated with the larger tip and applying the poroelastic theory to $E_{s,DL}$ gives meaningless results. To confirm this statement, in Figure 4.22(c) no overlapping occurs if the normalized time is introduced. Besides, dashed gray curves seem to overlap already with respect to natural time, suggesting that viscoelastic properties can play a relevant role, at least at the largest length analyzed. This last result confirms the very limited ability for cartilage to self-healing (Henrotin & Reginster, 1999): if the lesion is untreated, the regrowth results a tissue with worst properties, losing its poroelastic aspects.
A lower drained indentation modulus related to the larger tip is a consolidated outcome; among the samples analyzed here, this condition is achieved not only for native and $E_{s,PL}$ samples, but also for $E_{s,PM}$ sample. This consideration suggests that the particular scaffold used appears suitable to define a skeleton over which the cells can grow: in fact, when the natural migration of chondrocytes happens, its structure is able to respond in a similar way than the fibrous organization of native cartilage. On the contrary, it does not provide the proper *porous* properties showing more marked *viscous* aspects than control condition at least at the characteristic length scales analyzed here. Thus, the particular growth of stem cell in this kind of scaffold is very promising: elastic properties are recovered almost completely, whereas the organization of the porosity seems not to replicate the proper native condition. It is important to remember that the interests in the organization at micrometric length derives from the fact the macroscopic properties arise from the microstructure and only a proper microscopic organization can result in correct mechanical properties.

REFERENCES

Ateshian, G., Warden, W., Kim, J., Grelsamer, R., & Mow, V. (1997). Finite deformation biphasic material properties of bovine articular cartilage from confied compression experiments. *Journal of Biomechanics, 30*, 1137-1164.

Bonnevie, E., Baro, V., Wang, L., & Burris, D. (2012). Fluid load support during localized indentation of cartilage with a spherical probe. *Journal of Biomechanics, 45*, 1036-1041.

Chen, A., Bae, W., Schinagl, R., & Sah, R. (2001). Depth- and strain-dependendent mechanical and electromechanical properties of full-thickness bovine articular cartilage in confined compression. *Journal of Biomechanics, 34*(1), 1-12.

Delafargue, A., & Ulm, F. (2004). Explicit approximations of the indentation modulus of elastically orthotropic solids for conical indenters. *International Journal of Solids and Structures, 41*, 7351-7360.

Dintwa, E., Tijskens, E., & Ramon, H. (2008). On the accuracy of the Hertz model to describe the normal contact of soft elastic spheres. *Granular Matter, 10*, 209-221.

Franke, O., Durst, K., Maier, V., Goken, M., Birkholz, T., Schneider, H., . . . Gelse, K. (2007). Mechanical properties of hyaline and repair cartilage studied by nanoindentation. *Acta Biomaterialia , 3*, 873-881.

Franke, O., Goken, M., Meyers, M., Durst, K., & Hodge, A. (2011). Dynamic nanoindentation of articular porcine cartilage. *Materials Science and Engineering C, 31*, 789-795.

Galli, M., & Oyen, M. (2009). Fast identification of poroelastic parameters from indentation tests. *Computer Modeling in Engineering and Science, 48*, 241-268.

Grodzinsky, A., Roth, V., Myers, E., Grossman, W., & Mow, V. (1981). The significance of electromechanical and osmotic forces in nonequilibrium swelling behavior of articular cartilage in tension. *Journal of Biomechanical Engineering - The ASME Digital Library, 103*, 221-231.

Han, L., Frank, E., Greene, J., Lee, H., Hung, H., Grodzinsky, A., & Ortiz, C. (2011). Time-Dependent Nanomechanics of Cartilage. *Biophysical Journal, 100*, 1846-1854.

Henrotin, Y., & Reginster, J. (1999). Anabolic events in osteoarthritis. *Osteoarthritis and Cartilage, 7*, 310-312.

Hu, Y., Chen, X., Whitesides, G., Vlassak, J., & Suo, Z. (2011). Indentation of polydimethylsiloxane submerged in organic solvents. *Journal of Material Research, 26*, 785-795.

Hu, Y., Zhao, X., Vlassak, J., & Suo, Z. (2010). Using indentation to characterize the poroelasticity of gels. *Applied Physics and Letters, 96*, 121904-1:3.

Johnson, K. (1985). *Contact Mechanics.* Cambridge: Cambridge University Press.

Jurvelin, J., Muller, D., Wong, M., Studer, D., Engel, A., & Hunziker, E. (1996). Surface and subsurface morphology of bovine humeral articular cartilage as assessed by atomic force and transmission electron microscopy. *Journal of Structural Biologiy, 117*, 45-54.

Korhonen, R., Wong, M., Arokoski, J., Lindgern, R., Helminen, H., Hunziker, E., & Jurvelin, J. (2002). Importange of the superficial tissue layer for the indentation stiffness of articular cartilage. *Medical Engineering and Physics, 24*, 99-108.

Lee , B., Han, L., Frank, E., Chubinskaya, S., Ortiz, C., & Grodzinsky, A. (2010). Dynamic mechanical properties of the tissue engineered matrix associated with individual chondrocytes. *Journal of Biomechanics, 43*, 469-476.

Li, L., Buschmann, M., & Shirazi-Adl, A. (2003). Strain-rate dependent stiffness of articular cartilage in unconfined compression. *Journal of Biomechanical Engineering, 125*, 161-168.

Loparic, M., Wirtz, D., Daniels, A., Raiteri, R., vanLandingham, M., Guex, G., . . . Stolz, M. (2010). Micro- and nanomechanical analysis of articular cartilage by indentation-type atomic force microscopy: validation with a gel-microfiber composite. *Biophysical Journal, 98*, 2731-2740.

Nia, H., Han, L., Li, Y., Ortiz, C., & Grodzinsky, A. (2011). Poroelasticity of cartilage at the nanoscale. *Biophysical Journal, 101*, 2304-2313.

Park, S., Costa, K., Ateshian, G., & Hong, K. (2009). Mechanical properties of bovine articular cartilage under microscale indentation loading from atomicc force microscopy. *Proceedings of the Institution of Mechanical Engineers. Part H, Journal of Engineering in Medicine, 223*(3), 339-347.

Simha, N., Jin, H., Hall, M., Chiravarambath, S., & Lewis, J. (2007). Effect of indenter size on elastic modulus of cartilage measured by indentation. *Journal of Biomechanical Engineering, 129*, 767-775.

Williamson, A., Chen, A., & Sah, R. (2001). Compressive properties and function-composition relationships of developing bovine articular cartilage. *Journal of Orthopaedic Research, 19*, 1113-1121.

Chapter 4. Experimental Tests: Nanoindentation in Frequency Domain and Time Domain

Chapter 5.

Numerical Model of Nanoindentation DMA Test in Frequency Domain

In this Chapter the implementation of a poroelastic model capable to simulate the problem of dynamic mechanical analysis applied to nanoindentation is presented. In Section 5.1, the theoretical and numerical backgrounds are widely explained. The proper validation of the model and a sensitivity analysis are shown in Section 5.2: the effects of geometrical (setup of a spherical nanoidentation test) and constitutive (mainly, anisotropy ratio and out - of -plane Poisson's ratio for a transversely isotropic material) parameters are studied. In Section 5.3, the model is used in an inverse procedure to identify the constitutive parameters from selected experimental data analyzed in Section 4.1.

The aim of the present Chapter is to study, by means of numerical models, the poroelastic frequency response of AC, or poroelastic soft hydrated tissues in general, subjected to dynamic nanoindentation test.
To achieve this goal, a suitably developed computational model for the simulation of harmonic forced oscillations on poroelastic media in the frequency domain is used. The analytical solution available for confined compression test is used as benchmark to validate the numerical model. Then, the computational model is proven to be well - suited to explore the effects of material constitutive parameters and experiment characteristic size in harmonic nanoindentation tests. Sensitivity analyses are performed for both geometrical and constitutive parameters. In the former, a linear poroelastic isotropic material of given Young's modulus, Poisson's ratio and permeability is indented using a spherical tip. The role played by the indenter radius and the indenter penetration depth are highlighted. In the latter case study, a linear elastic transversely isotropic material is indented in a fixed geometric configuration, by varying the anisotropy ratio and the out - of - plane Poisson's ratio. Length scale effect and anisotropic properties, in fact, introduce complexities in the model but the key features of an interesting tissues as AC are hidden behind them. Once the model is validated and the sensitivity analysis performed, it is applied to a real situation: among the experimental data presented in the Section 4.1, experiments collected with the larger spherical tip ($R_{7500} = 7500\,nm$) are considered again. This continuum based numerical model is used with the purpose to determine constitutive parameters, as the anisotropy ratio between the axial and transverse stiffness of the superficial layers, shear modulus, local permeability of the fluid-filled tissue as well as the Poisson's ratios of superficial layers in mature bovine articular cartilage.

5.1 DMA NUMERICAL MODEL

5.1.1 Anisotropic elastic material

According to the framework proposed by Zienkiewicz (Zienkiewicz & Taylor, 2000), the constitutive relation in a transversely isotropic linear elastic material for an axisymmetric case yields:

$$\begin{cases} \varepsilon_r = \frac{\sigma_r}{E_1} - \frac{\nu_2\sigma_z}{E_2} - \frac{\nu_1\sigma_\theta}{E_1} \\ \varepsilon_z = -\frac{\nu_2\sigma_r}{E_2} + \frac{\sigma_z}{E_2} - \frac{\nu_2\sigma_\theta}{E_2} \\ \varepsilon_\theta = -\frac{\nu_1\sigma_r}{E_1} - \frac{\nu_2\sigma_z}{E_2} + \frac{\sigma_\theta}{E_1} \\ \gamma_{rz} = \frac{\tau_{rz}}{G_2} \end{cases} \tag{5.1}$$

where r, z and θ are respectively the axial, radial and circumferential coordinates. E identifies the Young's modulus and ν the Poisson's ratio; subscripts 1 and 2 indicate the in - plane contribution (radial and circumferential directions) and the out - of -

plane contribution (axial direction), respectively; in the $r-\theta$ plane the material response is isotropic.

Defining the anisotropy ratio $\lambda = \frac{E_2}{E_1}$ and recalling $E_2 = E_a$, $\nu_2 = \nu$ and $\nu_1 = \lambda\eta$, the compliance matrix can be written as

$$\boldsymbol{D} = \frac{1}{E_a}\begin{bmatrix} \lambda & -\nu & -\lambda\eta & 0 \\ -\nu & 1 & -\nu & 0 \\ -\lambda\eta & -\nu & \lambda & 0 \\ 0 & 0 & 0 & \frac{E_a}{G_2} \end{bmatrix} \tag{5.2}$$

The validity of the constitutive relation, in a thermodynamic sense, is subjected to the positive definition of the compliance matrix. Because of the symmetry of the matrix, the conditions come from the positivity of principal minors, as follows:

$$\begin{cases} \lambda > 0 \\ -\sqrt[2]{\lambda} < \nu < +\sqrt[2]{\lambda} \\ -\frac{\sqrt[2]{2}*\sqrt[2]{\lambda-\lambda\eta}}{2} < \nu < +\frac{\sqrt[2]{2}*\sqrt[2]{\lambda-\lambda\eta}}{2} \end{cases} \tag{5.3}$$

As shown in Figure 5.1, given a value of η, ν can span over the space defined under the respective thin curve, because the more restrictive condition is given by the third Equation in System (5.3).

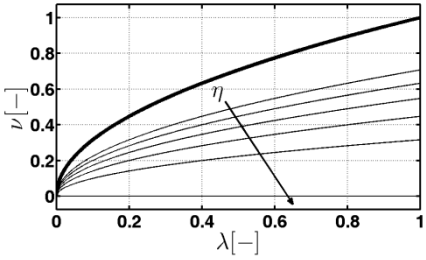

Figure 5.1: Bold line: plot of second Equation in (5.3); thin lines: plot of third Equation in (5.3), assuming η as parameter. Only positive values of ν are considered.

If one considers the case in which the in - plane and the out – of - plane Poisson's ratios are equal, the compliance matrix becomes

$$\boldsymbol{D} = \frac{1}{E_a} * \begin{bmatrix} \lambda & -\nu & -\lambda\nu & 0 \\ -\nu & 1 & -\nu & 0 \\ -\lambda\nu & -\nu & \lambda & 0 \\ 0 & 0 & 0 & \frac{E_a}{G_2} \end{bmatrix} \tag{5.4}$$

and the positively definiteness conditions have the form of

$$\begin{cases} \lambda > 0 \\ -\sqrt[2]{\lambda} < \nu < +\sqrt[2]{\lambda} \\ -\frac{\lambda}{4} - \frac{\sqrt[2]{\lambda^2+8\lambda}}{4} < \nu < -\frac{\lambda}{4} + \frac{\sqrt[2]{\lambda^2+8\lambda}}{4} \end{cases} \tag{5.5}$$

In Figure 5.2 as well, given a value of η, ν can span over the space defined under the thin curve, because the more restrictive condition is given by the third Equation in System (5.5).

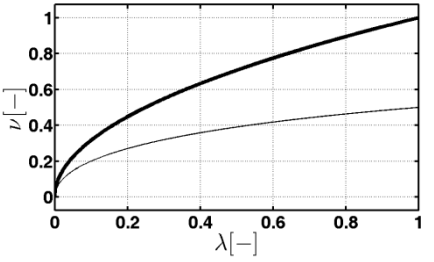

Figure 5.2 Bold line: plot of second Equation in (5.5); the solid line is the graph of the third Equation in (5.5). Only positive values of ν are considered.

5.1.2 Implementation

In this Section the problem formulation for a saturated porous medium is briefly introduced: spatial configuration is assumed.

According to Cowin and Doty (Cowin & Doty, 2006), if one considers a representative volume element (RVE) subjected to a total stress $\boldsymbol{\sigma}$ and to a pressure p, the deformation of the medium can be split in two parts (Voigt notation is adopted):

- i) Elastic deformation of the solid matrix due to the effective stress $\boldsymbol{\sigma}'$ (Terzaghi, 1943) namely
  $$\boldsymbol{\sigma}' = \boldsymbol{\sigma} + \boldsymbol{m}p \tag{5.6}$$
  where $\boldsymbol{\sigma}$ is the total Cauchy stress, $\boldsymbol{m} = [1\ 1\ 1\ 0\ 0\ 0]$.
- ii) Volumetric elastic deformation due to the fluid pressure.

By combining the above two contributions, the total deformation can be written as

$$\boldsymbol{\varepsilon} = \boldsymbol{C^d}^{-1}(\boldsymbol{\sigma} + \boldsymbol{m}p) - \boldsymbol{m}\frac{p}{3K_s} \tag{5.7}$$

where $\boldsymbol{C^d}$is the elastic drained stiffness matrix, K_s is the bulk modulus of the solid matrix. Then, the total stress is

$$\boldsymbol{\sigma} + \alpha\boldsymbol{m}p = \boldsymbol{C^d}\boldsymbol{\varepsilon} \tag{5.8}$$

where $\alpha = 1 - \frac{\boldsymbol{m}^T\boldsymbol{C^d}\boldsymbol{m}}{9K_s}$ is the Biot coefficient. In case of isotropic material, the

drained bulk modulus K_T is defined as $K_T = \frac{\boldsymbol{m}^T \boldsymbol{C}^d \boldsymbol{m}}{9} = \frac{3C^d}{9(1-2\nu)}$ in which ν is the Poisson's ratio and $\alpha = 1 - \frac{K_T}{K_s}$. In this way, using two mechanical parameters as K_s and K_T, the parameter α is defined.

Concerning the fluid phase, the total variation of fluid content $\dot{\xi}$ has to be defined. Its time variation is due to several contributions:

- Total macroscopic deformation of the structure;
- Fluid compression due to pressure increment;
- Matrix compression due to pressure increment;
- Matrix deformation due to matrix stresses.

Introducing the porosity a as the ratio between the volume of pore fluid and the total volume, $a = \frac{dV^v}{dV}$, the total variation of fluid can be written as

$$\dot{\xi} = \boldsymbol{m}^T \dot{\boldsymbol{\varepsilon}} + a\frac{\dot{p}}{K_F} + (1-a)\frac{\dot{p}}{K_S} - \frac{\boldsymbol{m}^T \dot{\boldsymbol{\sigma}}'}{3K_S} \tag{5.9}$$

that can be reduced as

$$\dot{\xi} = \alpha \boldsymbol{m}^T \dot{\boldsymbol{\varepsilon}} + \frac{\dot{p}}{M_B} \tag{5.10}$$

where the Biot modulus M_B is defined as $\frac{1}{M_B} = \frac{a}{K_F} + \frac{\alpha - a}{K_S}$, K_F is the bulk modulus of fluid phase and the overdot indicates the partial derivative with respect to time.

Equations (5.8) and (5.10) describe the coupled constitutive Equations for a poroelastic medium:

$$\begin{cases} \boldsymbol{\sigma} + \alpha \boldsymbol{m} p = \boldsymbol{C}^d \boldsymbol{\varepsilon} \\ \dot{\xi} = \alpha \boldsymbol{m}^T \dot{\boldsymbol{\varepsilon}} + \frac{\dot{p}}{M_B} \end{cases} \tag{5.11}$$

The system of Equations (5.11) holds for small displacements and small strains, when hydrostatic fluid stresses, isothermal process and total fluid saturation are assumed. Since bulk modulus of the solid matrix is much larger than volumetric compressibility of the porous medium, the assumption of intrinsic incompressibility is done. If also fluid is assumed incompressible, the Biot coefficient and the Biot modulus become, respectively, $\alpha = 1$ and $\frac{1}{M_B} = 0$ (Simon, 1992).

The equilibrium equation, in a general framework, is

$$\begin{cases} div(\boldsymbol{\sigma}) = \boldsymbol{F} + \rho \ddot{\boldsymbol{u}} \; in \; \Omega \\ \boldsymbol{\sigma n} = \boldsymbol{f} \; in \; \Gamma \end{cases} \tag{5.12}$$

where $\boldsymbol{F}$ and $\boldsymbol{f}$ are, respectively, body forces and surface forces in a RVE of volume Ω and boundary Γ.

In the absence of inertia and body forces, the terms $\boldsymbol{F}$ and $\rho \ddot{\boldsymbol{u}}$ are equal to zero.

The flow of the pore fluid is assumed to obey Darcy's law, i.e. the fluid flux J is proportional to the gradient of the pressure ∇p :

$$\boldsymbol{J} = -\boldsymbol{K}\boldsymbol{\nabla}p \tag{5.13}$$

where $\boldsymbol{K}\left[\frac{m^4}{N*s}\right]$ is the permeability tensor. In case of isotropy and homogeneity, the permeability reduces to a scalar k which can be a function of the void ratio, a.
The continuity equation is

$$-div(J) = \dot{\xi} \tag{5.14}$$

Substituting Equation (5.13) in (5.10), under the hypothesis of isotropic and homogeneous permeability, the continuity equation becomes

$$kdiv(\boldsymbol{\nabla}\mathrm{p}) = \alpha \boldsymbol{m}^T \dot{\boldsymbol{\varepsilon}} \tag{5.15}$$

A finite element formulation of the above set of governing Equations has been obtained by using the Galërkin approach which provides the basis for the weak formulation of the first Equation in (5.11) and Equation (5.15). The *principle of virtual displacements* is formulated as follows:

$$\int_\Omega \boldsymbol{\varepsilon}^T \boldsymbol{C^d}\, \delta\boldsymbol{\varepsilon} d\Omega - \int_\Omega p\boldsymbol{m}^T \delta\boldsymbol{\varepsilon} d\Omega - \int_\Gamma \boldsymbol{f}^T \delta\boldsymbol{u} d\Gamma = 0 \;\forall \delta\boldsymbol{u} \; and \; \delta\boldsymbol{\varepsilon} = \boldsymbol{C}\delta\boldsymbol{u} \tag{5.16}$$

where $\delta\boldsymbol{u}$ is the virtual displacement and $\delta\boldsymbol{\varepsilon}$ is the virtual strain compatible with virtual displacement. A *virtual pressure principle* is also considered

$$\int_\Omega \boldsymbol{\nabla}p^T k\, \boldsymbol{\nabla}\delta p d\Omega - \int_\Omega \boldsymbol{m}^T \dot{\boldsymbol{\varepsilon}} \delta p d\Omega = 0 \;\forall \delta p \tag{5.17}$$

where δp is the virtual pressure variation. In this simplified model, the material parameters are the isotropic homogeneous permeability parameter k and the elastic parameters in the drained stiffness matrix $\boldsymbol{C^d}$. Integrals in Equations (5.16) and (5.17) are evaluated on the whole region Ω and on its boundary Γ. The region Ω is divided into finite elements, denoted hereinafter by the superscript (e). In a single element both the virtual field and the actual field are interpolated as follows:

$$\begin{aligned}
\boldsymbol{u} &= \boldsymbol{N}_u \boldsymbol{u}_n \\
\delta\boldsymbol{u} &= \boldsymbol{N}_u \delta\boldsymbol{u}_n \\
\boldsymbol{\varepsilon} &= \boldsymbol{B}_u \boldsymbol{u}_n \\
\delta\boldsymbol{\varepsilon} &= \boldsymbol{B}_u \delta\boldsymbol{u}_n \\
p &= \boldsymbol{N}_p \boldsymbol{p}_n \\
\dot{p} &= \boldsymbol{N}_p \dot{\boldsymbol{p}}_n \\
\delta p &= \boldsymbol{N}_p \delta\boldsymbol{p}_n \\
\nabla p &= \boldsymbol{B}_p \boldsymbol{p}_n
\end{aligned} \tag{5.18}$$

where the entries of the vectors $\boldsymbol{u}_n$ and $\boldsymbol{p}_n$ are the unknown variables of displacement and pressure for the single n - *th* element and the matrices $\boldsymbol{N}_u, \boldsymbol{N}_p, \boldsymbol{B}_u$ and $\boldsymbol{B}_p$ describe the shape functions for the displacement field, the shape functions for the pressure field, the compatibility matrix for strain and the gradient matrix for pressure, respectively. Introducing for each element the connectivity matrices $\boldsymbol{L}_u^e$

and $\boldsymbol{L}_p^e$ that link the displacement (pressure) degrees of freedom of a single element, $\boldsymbol{u}_n$ $(\boldsymbol{p}_n)$, to all the displacement (pressure) degrees of freedom for the whole model, $\boldsymbol{U}$ $(\boldsymbol{P})$, the governing Equations in the finite element framework are derived

$$\begin{aligned}&\boldsymbol{U}^T \sum_e \boldsymbol{L}_u^{eT} \int_{\Omega_e} \boldsymbol{B}_u{}^T \boldsymbol{C}^{\boldsymbol{d}} \boldsymbol{B}_u \, d\Omega \boldsymbol{L}_u^e \delta\boldsymbol{U} - \boldsymbol{P}^T \sum_e \boldsymbol{L}_p^{eT} \int_{\Omega_e} \boldsymbol{N}_p{}^T \boldsymbol{m}^T \boldsymbol{B}_u \, d\Omega \boldsymbol{L}_u^e \delta\boldsymbol{U} = 0 \;\forall\; \delta\boldsymbol{U} \\ &\boldsymbol{P}^T \sum_e \boldsymbol{L}_p^{eT} \int_{\Omega_e} \boldsymbol{B}_p{}^T k \, \boldsymbol{B}_p \, d\Omega \boldsymbol{L}_p^e \delta\boldsymbol{P} + \dot{\boldsymbol{U}}^T \sum_e \boldsymbol{L}_u^{eT} \int_{\Omega_e} \boldsymbol{B}_u{}^T \boldsymbol{m}^T \boldsymbol{N}_p \, d\Omega \boldsymbol{L}_p^e \delta\boldsymbol{P} = 0 \;\forall\; \delta\boldsymbol{P}\end{aligned} \tag{5.19}$$

where $\boldsymbol{u}_n = \boldsymbol{L}_u^e \boldsymbol{U}$ and $\boldsymbol{p}_n = \boldsymbol{L}_p^e \boldsymbol{P}$. As the vectors $\delta\boldsymbol{U}$ and $\delta\boldsymbol{P}$ can be simplified in the system of Equations (5.19) and recalling

$$\boldsymbol{K}_{uu}{}^T = \sum_e \boldsymbol{L}_u^{eT} \int_{\Omega_e} \boldsymbol{B}_u{}^T \boldsymbol{C}^{\boldsymbol{d}} \boldsymbol{B}_u \, d\Omega \boldsymbol{L}_u^e, \qquad \boldsymbol{G}_{up}{}^T = \sum_e \boldsymbol{L}_p^{eT} \int_{\Omega_e} \boldsymbol{N}_p{}^T \boldsymbol{m}^T \boldsymbol{B}_u \, d\Omega \boldsymbol{L}_u^e,$$

$$\boldsymbol{G}_{pu}{}^T = \sum_e \boldsymbol{L}_u^{eT} \int_{\Omega_e} \boldsymbol{B}_u{}^T \boldsymbol{m}^T \boldsymbol{N}_p \, d\Omega \boldsymbol{L}_p^e, \text{ and } \boldsymbol{K}_{pp}{}^T = \sum_e \boldsymbol{L}_p^{eT} \int_{\Omega_e} \boldsymbol{B}_p{}^T k \, \boldsymbol{B}_p \, d\Omega \boldsymbol{L}_p^e,$$

the problem can be written as

$$\begin{cases} \boldsymbol{K}_{uu}\boldsymbol{U} - \boldsymbol{G}_{up}\boldsymbol{P} = 0 \\ \boldsymbol{G}_{pu}\dot{\boldsymbol{U}} + \boldsymbol{K}_{pp}\boldsymbol{P} = 0 \end{cases} \tag{5.20}$$

By imposing a harmonic forced displacement $\bar{\boldsymbol{U}}$ at a given frequency f_0 and known magnitude $\boldsymbol{U}_0$

$$\bar{\boldsymbol{U}} = \boldsymbol{U}_0 e^{if_0 t} \tag{5.21}$$

the model response will be of the form:

$$\begin{cases} \boldsymbol{U} = \boldsymbol{U}_{node} e^{if_0 t} \\ \boldsymbol{P} = \boldsymbol{P}_{node} e^{if_0 t} \end{cases} \tag{5.22}$$

where $\boldsymbol{U}_{node}$ and $\boldsymbol{P}_{node}$ are, in general, complex numbers, defined by a modulus and a phase shift.

Substituting (5.21) and (5.22) into the system (5.20), the problem reduces to

$$\begin{cases} \boldsymbol{K}_{uu}\boldsymbol{U}_{node} e^{if_0 t} - \boldsymbol{G}_{up}\boldsymbol{P}_{node} e^{if_0 t} = \boldsymbol{F}_u e^{if_0 t} \\ if\,\boldsymbol{G}_{pu}\,\boldsymbol{U}_{node} e^{if_0 t} + \boldsymbol{K}_{pp}\boldsymbol{P}_{node} e^{if_0 t} = \boldsymbol{F}_p e^{if_0 t} \end{cases} \tag{5.23}$$

where the right hand side terms come from the imposed displacement (5.22). In particular, since the known displacement has an amplitude $\boldsymbol{U}_0$ that is a real vector, $\boldsymbol{F}_u$ is only composed by its real part $\boldsymbol{F}_{ur}$ and $\boldsymbol{F}_p$ is only composed by its imaginary part $\boldsymbol{F}_{pi}$. Finally, the poroelastic problem under harmonic forced displacement (in the case of imposed force, the derivation is similar) becomes, in matrix form

$$\begin{bmatrix} \boldsymbol{K}_{uu} & -\boldsymbol{G}_{up} \\ if\,\boldsymbol{G}_{pu} & -\boldsymbol{K}_{pp} \end{bmatrix} * \begin{bmatrix} \boldsymbol{U}_{node} \\ \boldsymbol{P}_{node} \end{bmatrix} = \begin{bmatrix} \boldsymbol{F}_u \\ \boldsymbol{F}_p \end{bmatrix} \tag{5.24}$$

The above set of finite element Equations have been implemented in the Matlab environment (MathWorks, Natick, MA, USA).

5.1.3 Limit cases: numerical computation of drained and undrained indentation moduli

The behavior of a poroelastic medium is governed by the mechanical properties of the matrix and the flow of the fluid through pores; these two aspects can be analyzed separately by studying the frequency response for two limit cases.

In particular, if one considers the limit to quasi - static loading ($f \to 0$), the fluid pressure is uniform into the specimen and there is equilibrium with the external pressure: the behavior is then governed by the porous matrix only; this condition is defined as drained state. The second limit case is the ideal step loading ($f \to \infty$), in which $\dot{\xi}$=0 and the hydrostatic stress component is carried by the fluid: this condition is defined as undrained state.

The analytical computation of the limit cases has been already shown in Equation (3.25) for the isotropic case and Equation (3.27) for the transversely isotropic one. Let us move to the proposed numerical model, instead. Since the solutions described by the vectors $\boldsymbol{U}_{node}$ and $\boldsymbol{P}_{node}$ have complex entries, they can be explicitly expressed as

$$\begin{cases} \boldsymbol{U}_{node} = \boldsymbol{U}_r + i\boldsymbol{U}_i \\ \boldsymbol{P}_{node} = \boldsymbol{P}_r + i\boldsymbol{P}_i \end{cases} \tag{5.25}$$

where $\boldsymbol{U}_r$ and $\boldsymbol{P}_r$ are the real parts and $\boldsymbol{U}_i$ and $\boldsymbol{P}_i$ are the imaginary parts.

Substituting (5.25) in (5.23), the problem can be written as

$$\begin{cases} \boldsymbol{K}_{uu}(\boldsymbol{U}_r + i\boldsymbol{U}_i) - \boldsymbol{G}_{up}(\boldsymbol{P}_r + i\boldsymbol{P}_i) = \boldsymbol{F}_{ur} \\ if\boldsymbol{G}_{pu}\,(\boldsymbol{U}_r + i\boldsymbol{U}_i) - \boldsymbol{K}_{pp}(\boldsymbol{P}_r + i\boldsymbol{P}_i) = \boldsymbol{F}_{pi} \end{cases} \tag{5.26}$$

And, simplifying,

$$\begin{cases} \boldsymbol{K}_{uu}\boldsymbol{U}_r + i\boldsymbol{K}_{uu}\boldsymbol{U}_i - \boldsymbol{G}_{up}\boldsymbol{P}_r - i\boldsymbol{G}_{up}\boldsymbol{P}_i = \boldsymbol{F}_{ur} \\ if\boldsymbol{G}_{pu}\,\boldsymbol{U}_r - f\boldsymbol{G}_{pu}{}^T\boldsymbol{U}_i - \boldsymbol{K}_{pp}\boldsymbol{P}_r - i\boldsymbol{K}_{pp}\boldsymbol{P}_i = \boldsymbol{F}_{pi} \end{cases} \tag{5.27}$$

This system of two vector Equations can be split in the real and imaginary parts giving a system of four vector Equations:

$$\begin{cases} \boldsymbol{K}_{uu}\boldsymbol{U}_r - \boldsymbol{G}_{up}\boldsymbol{P}_r = \boldsymbol{F}_{ur} \\ \boldsymbol{K}_{uu}\boldsymbol{U}_i - \boldsymbol{G}_{up}\boldsymbol{P}_i = 0 \\ f\boldsymbol{G}_{pu}\,\boldsymbol{U}_i + \boldsymbol{K}_{pp}\boldsymbol{P}_r = 0 \\ f\boldsymbol{G}_{pu}\,\boldsymbol{U}_r - \boldsymbol{K}_{pp}\boldsymbol{P}_i = \boldsymbol{F}_{pi} \end{cases} \tag{5.28}$$

If $f \to 0$ (drained state), the system (5.28) becomes

$$\begin{cases} \boldsymbol{K}_{uu}\boldsymbol{U}_r - \boldsymbol{G}_{up}\boldsymbol{P}_r = \boldsymbol{F}_{ur} \\ \boldsymbol{K}_{uu}\boldsymbol{U}_i - \boldsymbol{G}_{up}\boldsymbol{P}_i = 0 \\ \boldsymbol{K}_{pp}\boldsymbol{P}_r = 0 \\ \boldsymbol{K}_{pp}\boldsymbol{P}_i = \boldsymbol{F}_{pi} \end{cases} \tag{5.29}$$

and the solution, in terms of pressure and displacement, is

$$\begin{cases} \boldsymbol{U}_r = \boldsymbol{K}_{uu}{}^{-1}\boldsymbol{F}_{ur} \\ \boldsymbol{U}_i = \boldsymbol{K}_{uu}{}^{-1}\boldsymbol{G}_{up}\boldsymbol{K}_{pp}{}^{-1}\boldsymbol{F}_{pi} \\ \boldsymbol{P}_r = 0 \\ \boldsymbol{P}_i = \boldsymbol{K}_{pp}{}^{-1}\boldsymbol{F}_{pi} \end{cases} \tag{5.30}$$

If $f \to \infty$ (undrained state), the system (5.28) becomes

$$\begin{cases} \boldsymbol{K}_{uu}\boldsymbol{U}_r - \boldsymbol{G}_{up}\boldsymbol{P}_r = \boldsymbol{F}_{ur} \\ \boldsymbol{K}_{uu}\boldsymbol{U}_i - \boldsymbol{G}_{up}\boldsymbol{P}_i = 0 \\ \boldsymbol{G}_{pu}\,\boldsymbol{U}_i = 0 \\ \boldsymbol{G}_{pu}\,\boldsymbol{U}_r = 0 \end{cases} \tag{5.31}$$

and the solution, in terms of pressure and displacement, is

$$\begin{cases} \boldsymbol{U}_r = \boldsymbol{K}_{uu}{}^{-1}\left(\boldsymbol{F}_{ur} + \boldsymbol{G}_{up}\boldsymbol{P}_r\right) = \left(\boldsymbol{K}_{uu}{}^{-1} + \boldsymbol{K}_{uu}{}^{-1}\boldsymbol{G}_{up}(\boldsymbol{G}_{pu}\boldsymbol{K}_{uu}{}^{-1}\boldsymbol{G}_{up})^{-1}\boldsymbol{G}_{pu}\boldsymbol{K}_{uu}{}^{-1}\right)\boldsymbol{F}_{ur} \\ \boldsymbol{U}_i = \boldsymbol{K}_{uu}{}^{-1}\boldsymbol{G}_{up}\boldsymbol{P}_i = 0 \\ \boldsymbol{P}_r = -(\boldsymbol{G}_{pu}\boldsymbol{K}_{uu}{}^{-1}\boldsymbol{G}_{up})^{-1}\boldsymbol{G}_{pu}\boldsymbol{K}_{uu}{}^{-1}\boldsymbol{F}_{ur} \\ \boldsymbol{P}_i = 0 \end{cases} \tag{5.32}$$

In a displacement - based test, the reaction force under the indenter is the sum of the reaction force on each node 'of the indenter'. For both $f \to 0$ and $f \to \infty$, these nodal forces are such that

$$\begin{cases} \boldsymbol{F}_{ur} \neq 0 \\ \boldsymbol{F}_{ui} = 0 \end{cases} \tag{5.33}$$

This result shows that, at both bounds, the behavior can be described only by real forces and displacements.

5.1.4 Implementation of a DMA AFM - based nanoindentation test

A typical DMA AFM - based nanoindentation test has been already widely explained. Here, the procedure is replicated by a two steps numerical simulation. In the first step, the preload is applied and a static (time independent) indentation is simulated; in the second step, an harmonic load is applied and the problem is solved in the frequency domain, where the reference (initial) configuration is the one obtained from the preload indentation. A two - dimensional axisymmetric model for spherical poroelastic dynamic indentation has been built. A rigid, spherical indenter of radius R is pressed into a cylindrical sample of radius W and height B. Indentation depth is denoted by h_s. The radius of the specimens is 20 times larger than the radius of the tip and the height of the specimen is 30 times larger than the indentation depth. These conditions are assumed to guarantee that the mechanical response to indentation is not affected by the domain boundaries.

For the first step, model geometry is defined and discretization is performed (approximately 15000 first order four-node elements) using the commercial

displacement - based finite element code Abaqus 6.8-EF1 (Simulia, Providence, RI, USA). A quasi - static indentation is simulated with depth h_s to obtain the deformed state to be used as input for the harmonic loading. According to the purpose of this step, the material model is linear elastic. The contact radius is resolved with approximately 30 elements. In Figure 5.3, a representation of the assembly constituted by a tip and a sample, is shown; since the model is axisymmetric the cartoon in Figure 5.3(a) is just a 3D representation.

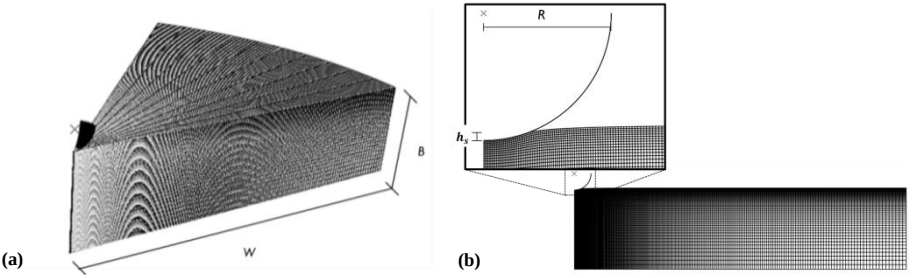

Figure 5.3: (a) 3D visualization of the axisymmetric mesh in the undeformed configuration and (b) the 2D axisymmetric mesh of the model in the deformed configuration with a zoom of the zone under the tip. The generic dimensions are highlighted.

Subsequently, the deformed geometry is used as input for the frequency domain model developed within the Matlab environment (MathWorks, Natick, MA, USA). The deformed mesh is used as stress - free initial configuration for the simulation of the dynamic nanoindentation in the frequency domain, according to the poroelastic framework introduced. A poroelastic material is now considered. An harmonic vertical displacement Δh_s of $0.1\ \mu m$ is imposed to the node set representing the contact radius. It is worth noting that for the linearized framework (small displacement oscillations) implemented in this work, the model response is independent of the displacement oscillation magnitude. The investigated range of frequencies varies from $0\ Hz$ (drained condition) up to the undrained condition, here simulated with a conventional frequency of $10^7\ Hz$.

Results coming out from the simulation are: the vertical reaction force $F = \Delta F(f) e^{ift} e^{i\phi_f(f)}$, where $\Delta F(f)$ is the magnitude of the sinusoidal response, and the correspondent phase shift $\phi_f(f)$, both dependent on the imposed frequency f. For sake of clarity, the way and the quantities used to analyze the results are briefly recalled here. The reduced storage modulus $E'^*(f)$ and the reduced loss modulus $E''^*(f)$ can be calculated as (Cheng, Ni, & Cheng, 2006)

$$E'^*(f) = \frac{1}{2}\frac{1}{\sqrt[2]{Rh_s}}\left|\frac{\Delta F(f)}{\Delta h_s}\right|\cos(\phi_f) \tag{5.34}$$

$$E''^*(f) = \frac{1}{2}\frac{1}{\sqrt[2]{Rh_s}}\left|\frac{\Delta F(f)}{\Delta h_s}\right|\sin(\phi_f) \tag{5.35}$$

in which R is the tip radius.
The normalized storage modulus $\overline{E'^*}$ highlights the effect of geometric parameters and it is defined as

$$\overline{E'^*}(f) = \frac{(E'^*(f) - E'^*(0))}{(E'^*(f\to\infty) - E'^*(0))} \quad (5.36)$$

The drained to undrained ratio $\frac{E'^*(0)}{E'^*(f\to\infty)}$ is dependent on the tissue properties and independent of its time response. The value of the tangent of the phase shift, $tan(\phi_f)$, versus frequency and the peak frequency, f_{max}, are measures of the typical scale in which fluid flow mainly occurs.
Numerical results is also analyzed by using the normalized frequency defined in analogy to the Equation (4.5) (Galli & Oyen, 2009) as follows:

$$\bar{f} = f\frac{Rh_s}{m} \quad (5.37)$$

where the parameter m has the same role of parameter P_2 in Section 4.2 and it is proportional to the permeability and to the elastic modulus; m is kept constant through all the simulations performed.

5.2 DMA NUMERICAL MODEL: SENSITIVITY ANALYSIS ON GEOMETRICAL AND CONSTITUTIVE PARAMETERS

5.2.1 Validation

The validation of the numerical code in the frequency domain is carried out by solving the plane strain problem of confined compression for which the analytical solution is known. The bottom and the lateral edges are impermeable whereas the top boundary is permeable. Due to the homogeneity along the horizontal direction (x direction), the problem can be simply reduced to a 1-D problem. In particular, the analytical solution in terms of fluid pressure and of top boundary displacement reads (Cowin & Doty, 2006):

$$p(z,t) = P_0\left(1 + tan\left(\sqrt{\frac{ifL^2}{c}}\right)\sinh\left(\frac{z}{L}\sqrt{\frac{ifL^2}{c}}\right) - cos\left(\frac{z}{L}\sqrt{\frac{ifL^2}{c}}\right)\right)e^{ift} \quad (5.38)$$

$$u(0,t) = \frac{1}{E}\sqrt{\frac{c}{ifL^2}}tan\left(\sqrt{\frac{ifL^2}{c}}\right)e^{ift} \quad (5.39)$$

where f is the frequency and c is a material parameter. In case of isotropic elasticity and incompressible materials, $c = \frac{kE(1-\nu^d)}{(1+\nu^d)(1-2\nu^d)}$ in which $E\ [MPa]$ is the Young's Modulus, ν^d is the drained Poisson's ratio, $k\ [\frac{m^2N}{s}]$ is the permeability. Equation (5.38) shows the value of the pressure as a function of the depth of the specimen and of the frequency, while Equation (5.39) shows the value of the displacement of the upper surface as a function of the frequency. The implemented model well compares

with the reference analytical solution: Figure 5.4 shows the fluid pressure distribution across the normalized thickness for a selected frequency.

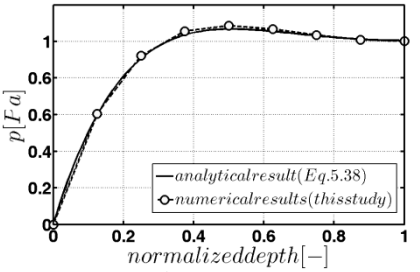

Figure 5.4: Pressure versus normalized depth for the 1-D benchmark problem; symbols refer to the finite element formulation; the solid line refers to the analytical solution (Cowin & Doty, 2006).

5.2.2 Effect of geometrical parameters

The harmonic indentation problem is first studied with respect to geometrical parameters. The indented material is, at this stage, modeled as homogeneous, isotropic and linear elastic with Young's modulus $E_i = 300\ KPa$, Poisson's ratio $\nu_i = 0.22$ and constant permeability $k_i = 10^{-15}\ \frac{m^4}{N\,s}$. These values fall within the range of interest for AC tissue. Indeed, in the literature, a wide range of values for Young's modulus can be found. Variability is basically a consequence of the specific type of tissue (human or animal or site of harvesting) as well as the probing technique. Jurvelin (Jurvelin, Buschmann, & Hunziker, 2003) reports Young's modulus of $581\pm168\ kPa$ after unconfined compression on samples extracted from the patellofemoral groove of human knee; Boschetti (Boschetti, Pennati, Gervaso, Peretti, & Dubini, 2004) performs unconfined compression tests on hip human native cartilage, obtaining $250\pm150\ kPa$ on the surface, $350\pm100\ kPa$ on the middle and $500\pm200\ kPa$ on deep layers. Kiviranta (Kiviranta, Lammentausta, Toyras, Kiviranta, & Jurvelin, 2008) carries out indentation on human patellae cartilage at different stages of tissue degradation due to osteoarthritis, that yielded values of $640\pm300\ kPa$ for healthy cartilage, $700\pm620\ kPa$ for early degeneration, down to $210\pm260\ kPa$ for advanced degradation. Concerning animal samples, Miller (Miller & Morgan, 2010) recently reports from microindentation and unconfined compression on human knee patellofemoral groove samples a mean value for Young's modulus of $740\ kPa$.

Different indentation depths and indentation radii are considered and the results for the different cases are compared. In particular, Table 5.1 summarizes the (R, h_s) sets along with model geometries used here to evaluate the effect of indentation depth while indenter radius R is kept constant. Table 5.2 reports the (R, h_s) sets and the respective specimen geometries adopted to investigate the effect of indenter/specimen size (i.e., the characteristic size), while the h_s/R ratio (i.e., an

estimation of the equivalent deformation) is kept constant.

Table 5.1: (R, h_s) case studies and respective model geometries for the evaluation of indentation depth effect (constant indenter radius). Sample radius W set to 20 times the indenter radius, sample height B set to 30 times the indenter radius.

$R[\mu m]$	$h_s[\mu m]$	$h_s/R[-]$	$W[\mu m]$	$B[\mu m]$
400	40	0.1	8000	1200
400	80	0.2	8000	2400
400	120	0.3	8000	3600
400	160	0.4	8000	4800

Table 5.2: (R, h_s) case studies and respective model geometries for the evaluation of size dependence (constant equivalent deformation). Sample radius W set to 20 times the indenter radius, sample height B set to 30 times the indenter radius.

$R[\mu m]$	$h_s[\mu m]$	$h_s/R[-]$	$W[\mu m]$	$B[\mu m]$
400	40	0.1	8000	1200
125	12.5	0.1	2500	375
25	2.5	0.1	500	75
7.5	0.75	0.1	150	22.5

In Table 5.3, the results obtained from the sensitivity analyses with respect to geometrical parameters are summarized. A good consistence is found in terms of reduced storage modulus E'^* and reduced loss modulus E''^*computed at limit conditions. Using Equation (3.27), the analytical estimates $E'^*(0) = 387\ KPa$ and $E'^*(f \to \infty) = 652\ KPa$ can be obtained. Results in Table 5.3 fit well, bearing in mind that the undrained stiffness matrix can be defined only asymptotically.
In Figure 5.5 the values of $\overline{E'^*}$ (consolidation ratio) are presented for both constant radius (a) and constant h_S/R ratio (b) cases, versus frequency. For both sets of analyses, it has been found that the frequency response shifts towards higher frequencies at decreasing penetration depth (Figure 5.5(a)) or decreasing indenter radius (Figure 5.5(b)).

Table 5.3: Geometric sensitivity analysis, involving all case studies.

CASE STUDY $R - h_s$	$E'^*(0)$ $[kPa]$	E'^* $(f \to \infty)$ $[kPa]$	$\frac{E'^*(0)}{E'^*(f \to \infty)}$ $[numerical]$	Max $tan(\phi_f)$	f_{max} $[Hz]$	$\frac{E'^*(0)}{E'^*(f \to \infty)}$ $[analytical]$
$i400 - h160$	354	520	0.68	0.111	0.0129	0.6
$i400 - h120$	359	535	0.67	0.116	0.0129	
$i400 - h80$	372	561	0.66	0.121	0.0245	
$i400 - h40$	394	604	0.65	0.129	0.0468	

CASE STUDY $R-h_s$	$E'^*(0)$ $[kPa]$	E'^* $(f\to\infty)$ $[kPa]$	$\frac{E'^*(0)}{E'^*(f\to\infty)}$ $[numerical]$	Max $tan(\phi_f)$	f_{max} $[Hz]$	$\frac{E'^*(0)}{E'^*(f\to\infty)}$ $[analytical]$
$i125-h12.5$	394	604	0.65	0.129	0.468	
$i25-h2.5$	394	604	0.65	0.129	12	
$i7.5-h0.75$	394	602	0.65	0.129	124	

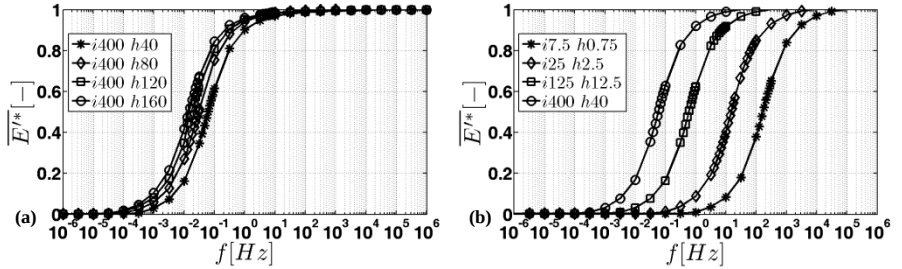

Figure 5.5: (a) $\overline{E'^*}$ vs frequency for simulations at given radius and (b) at given ratio.

Figures 5.6(a) and 5.6(b), show that the frequency responses overlap for all numerical experiments when normalized frequency is used.

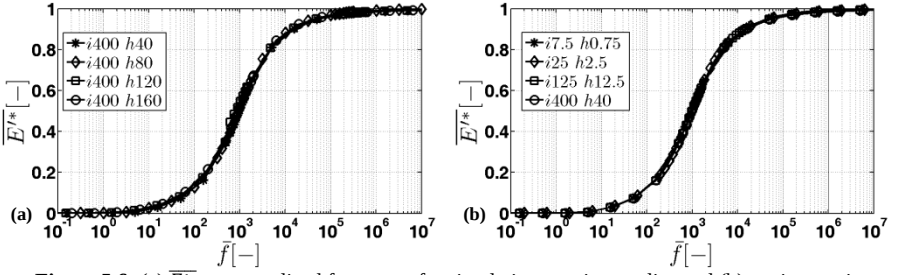

Figure 5.6: (a) $\overline{E'^*}$ vs normalized frequency for simulations at given radius and (b) at given ratio.

Figure 5.7 shows the tangent of the phase shift for all the analyzed cases. A shift of the frequency at peak can be found for both sets of numerical examples.
As for the consolidation rate, the response in terms of tangent of phase shift versus normalized frequency shows an overlap of frequency at peak (Figure 5.8). It is worth noting that the geometric parameters R and h_s affect the frequency at peak in both sets of analyses.

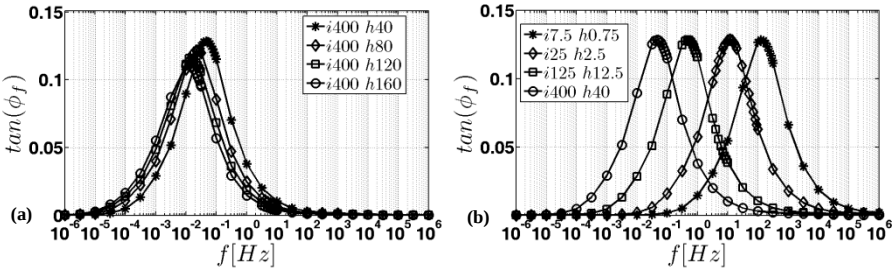

Figure 5.7: (a) $tan(\phi_f)$ vs frequency for simulations at given radius and (b) at given ratio.

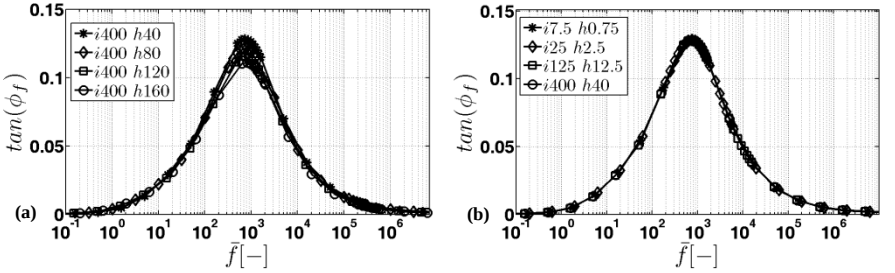

Figure 5.8: (a) $tan(\phi_f)$ vs normalized frequency for simulations at given radius and (b) at given ratio.

The relationship between the frequency at peak versus the geometrical parameter Rh_s, in a log - log plot, is presented in Figure 5.9; a good fitting with a linear function has been found of Equation: $f_{max} = 711.52(Rh_s)^{-0.996}$

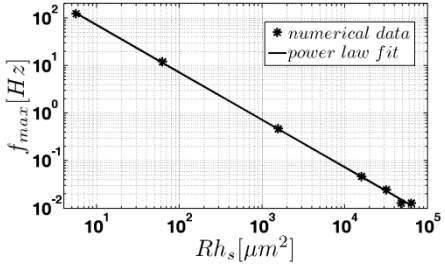

Figure 5.9: f_{max} vs geometrical parameter (Rh_s) for all cases.

5.2.3 Effect of constitutive parameters

The transversely isotropic model presented in Section 5.1 is now considered. The same nomenclature is used further on.

The sensitivity analysis is performed with respect to the anisotropy ratio λ and the out - of - plane Poisson's ratio ν. The other constitutive parameters (G, E_a, η) are kept fixed according to the following assumptions:

(i) Shear modulus has been assumed as $G = 100\ KPa$;
(ii) axial Young modulus has been chosen according to the following relationship $E_a = 2G$;
(iii) two different cases have been considered for the in - plane Poisson's ratio η: a) η=0 and b) $\eta = \nu$.

In Tables 5.4 and 5.5 the values of parameters λ and ν used in the analyses are presented, for in - plane Poisson's ratio $\eta = 0$ and $\eta = \nu$, respectively.

Table 5.4: Parametric study in the case of in-plane Poisson's ratio $\eta = 0$.

	λ	1	0.8	0.6	0.4	0.2	0.1
$\frac{\nu}{\nu_{max}}$	0.2	0.141	0.126	0.109	0.089	0.063	0.045
	0.4	0.283	0.253	0.219	0.179	0.126	0.089
	0.6	0.422	0.375	0.329	0.268	0.190	0.134
	0.8	0.566	0.506	0.438	0.358	0.253	0.179
	0.9	0.636	0.569	0.493	0.403	0.285	0.201

Table 5.5: Parametric study in the case of in-plane Poisson's ratio $\eta = \nu$.

	λ	1	0.8	0.6	0.4	0.2	0.1
$\frac{\nu}{\nu_{max}}$	0.2	0.1	0.09	0.084	0.072	0.054	0.04
	0.4	0.2	0.185	0.167	0.143	0.108	0.08
	0.6	0.3	0.278	0.251	0.215	0.162	0.12
	0.8	0.4	0.371	0.334	0.287	0.216	0.16
	0.9	0.45	0.417	0.376	0.323	0.243	0.18

As shown in Section 5.1, for a fixed set of parameters (G, E_a, λ, η), an upper bound for the out - of - plane Poisson's ratio ν, namely ν_{max}, can be found. The results, for each value of the anisotropy ratio λ, are presented here for different values of $\frac{\nu}{\nu_{max}}$.

The drained to undrained ratio $\frac{E'^*(0)}{E'^*(f\to\infty)}$ obtained through the numerical model is reported as a function of λ and for in - plane Poisson's ratio η=0 (Figure 5.10(a)); a good agreement with the analytical estimation is also observed (dashed lines). In Figure 5.10(b) a comparison between the two cases a) η=0 and b) $\eta = \nu$ is reported. In all cases a decrease of the drained to undrained ratio is found for materials with high anisotropy ratio (small λ). It is worth noting that the drained to undrained ratio can be smaller than 0.5 (lower bound for isotropic materials) for λ smaller than 0.4.

In Figure 5.11, the tangent of the phase shift as a function of lambda is presented, showing the comparison between the two cases of in - plane Poisson's ratio η. Figure 5.11 shows that the peak of phase shift is significantly affected by the anisotropy ratio; whereas, the frequency at peak is affected by the anisotropy ratio to a lesser extent.

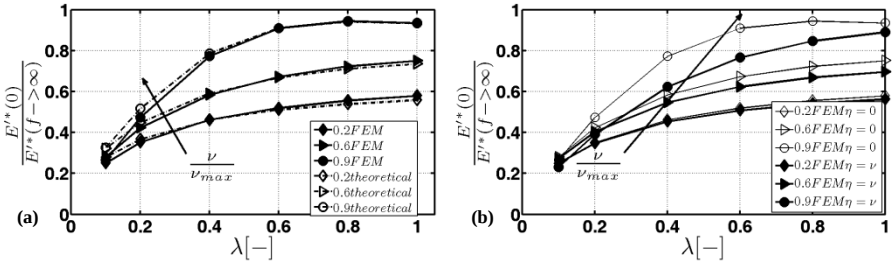

Figure 5.10: (a) The drained to undrained $\frac{E'^*(0)}{E'^*(f\to\infty)}$ vs λ is shown, parametrized with the ratio $\frac{\nu}{\nu_{max}}$. Solid lines refer to FEM simulations; dotted lines refer to analytical solutions. (b) Comparison of the drained to undrained ratio for $\eta = 0$ (open symbols) and $\eta = \nu$ (filled symbols).

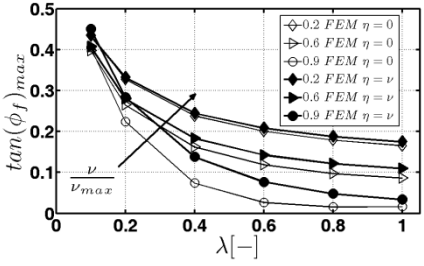

Figure 5.11: $tan(\emptyset_f)$ vs λ parametric with the ratio $\frac{\nu}{\nu_{max}}$; $\eta = 0$ (open symbols) $\eta = \nu$ (filled symbols).

Indeed, Figure 5.12 shows a decrease of the frequency at peak while remaining within the same order of magnitude; the case η=ν is shown.

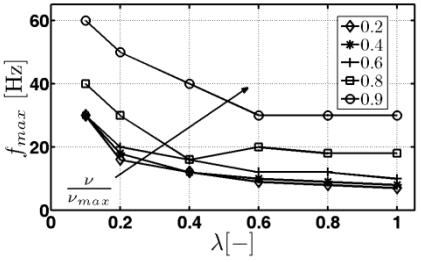

Figure 5.12: f_{max} *vs* λ parametrized with the ratio $\frac{\nu}{\nu_{max}}$.

5.2.4 Discussion

The object of this Section is to assess the frequency response of hydrated biological tissues to dynamic indentation loading through a numerical approach. The focus is on the effects of the characteristic lengths of the experiment and of the anisotropic

properties of the tissue.

The results have shown that the indentation radius (for constant penetration depth) has a large effect on the real part of the material response (see Figure 5.5(a)), whereas penetration depth (for constant h_s/R ratio) has a negligible effect on the real part of the response (see Figure 5.5(b)). In both cases, when normalized (dimensionless) frequency is used, the geometric effect disappears (all curves overlaps). This is consistent with a purely poroelastic response of the material as can be inferred from the analytical solution presented for the one dimensional confined compression in the frequency domain. Indeed, the analytical solution shows that the frequency response of pressure and displacement (Equations (5.38) and (5.39)) is dependent on the ratio $\frac{fL^2}{c}$ thus indicating that a the problem is strictly dependent on a dimensionless frequency $\bar{f} = \frac{fL^2}{c}$ in which the characteristic length of the experiment (L) is introduced. In this Section, this concept is extended to the frequency domain by introducing the dimensionless frequency for the indentation problem (Equation 5.37).

In the case of constant tip radius, if the indentation depth grows, both the values of $E'^*(0)$ and $E'^*(f \to \infty)$ decrease, as well as the maximum value of the tangent of the phase shift. For a large indentation depth, that is still reasonable in real experiments, the ratio $\frac{E'^*(0)}{E'^*(f\to\infty)}$ is higher and both $E'^*(0)$ and $E'^*(f \to \infty)$ are lower than expected from theory (see Table 5.3): the assumption of Hertzian contact introduced in the work of Delafargue (Delafargue & Ulm, 2004) may then not hold.

A good agreement between numerical and analytical responses in terms of the real part ($\frac{E'^*(0)}{E'^*(f\to\infty)}$), has been found for anisotropic poroelastic material. Slight differences found between numerical and analytical predictions can be due to the limitations of the elastic contact solutions used in the analytical model.

Furthermore, the undrained to drained ratio is strongly dependent on the anisotropy ratio. In fact, the lowest values of $\frac{E'^*(0)}{E'^*(f\to\infty)}$ can be found for strongly anisotropic materials, i.e. $\lambda \ll 1$, while for isotropic material $\frac{E'^*(0)}{E'^*(f\to\infty)} > 0.5$.

By combining the information on Figures 5.10(b) and 5.11, it is possible to infer that, for a small anisotropy ratio $\lambda \ll 1$, both the undrained to drained $\frac{E'^*(0)}{E'^*(f\to\infty)}$ ratio and the tangent of the phase are less sensitive to Poisson's coefficients. This is an advantage when identifying material properties of anisotropic materials for which it is difficult to identify Poisson's ratios accurately. Even if the sensitivity analysis is performed on a relatively small range of variability for some parameters (e.g. the in - plane Poisson's ratio η), the results show that the mechanical properties can vary to a large extent in some regions of the space defined by the 5 - ple $(G, E_a, \lambda, \eta, \nu)$ for a transversely isotropic material. Other works have already shown that dynamic indentation testing on cartilage tissue is a technique able to provide more

information with respect to quasi - static indentation experiments (Miller & Morgan, 2010) (Han, et al., 2011).
The results obtained in the present work lead to two important conclusions: first, if poroelasticity is the main dissipation mechanism for tissues exhibiting a time dependent response under dynamic indentation, then the results in terms of the dimensionless frequency will be independent on the geometric parameters. Consequently, if further size dependence is still observed in the dimensionless frequency domain, then further dissipative mechanisms are playing a role, and viscoelasticity would probably be involved. A second relevant result obtained in the present investigation is that nanoindentation experiments on poroelastic specimens in the frequency domain are strongly affected by material anisotropy. It follows that anisotropy ratio of anisotropic tissues (like articular cartilage) can be identified by carrying out nanoindentation experiments along one single direction in the frequency domain. In this case, experiments in drained and undrained conditions should be carried out.
Further developments are required for a reliable application to the frequency dependent characterization of biological tissues like cartilage, such as the implementation of the anisotropy of the hydraulic tensor in the finite deformation framework proposed by Ateshian (Ateshian & Weiss, 2010) or Federico (Federico & Herzog, 2008), and the formulation of the frequency domain response of nonlinear fibril reinforced constitutive law, more suited for cartilage tissues. A continuous distribution of fibril orientation of the collagen network as proposed in Shirazi (Shirazi, Vena, Sah, & Klisch, 2011) or in Federico (Federico & Gasser, 2010). This latter improvement would imply the linearization of the finite strain nonlinear constitutive law to be used in place of the transversely isotropic linear Equations which relates the increments of the stress with the increments of strains.

5.3 DMA NUMERICAL MODEL: PARAMETERS IDENTIFICATION

Numerical models are widely used because of their ease to collect information with respect to the real experimental tests; it is obvious that such of models need to use the correct parameters as input in order to reach meaningful results with a certain level of confidence. The main idea is to identify a set of parameters such that, over a desired range of operating conditions and in some well - defined sense, the model outputs are close to the system outputs when both of them are submitted to the same inputs (Castello, Rochinha, Roitman, & Magluta, 2008). Hence, the inverse approach on the parameters identification means to use the results from a completely known model to fit the experimental results coming from samples of which the knowledge about the mechanical parameters is low or null at all (Lei & Szeri, 2007). Due to incompleteness of available information and unavoidable measurements errors, system identification only achieves an approximation of the actual system.
The identification problem on soft tissues is an issue of current interest. For example, Olberding and Suh (Olberding & Suh, 2006) propose a method for the

material characterization of soft biological tissues using a biphasic poroviscoelastic constitutive model and data from creep and stress relaxation test collected with a solid plane - ended cylindrical indenter. In the work of Namani (Namani, Simha, & Lewis, 2003), instead, the nonlinear material parameters of bovine AC is identified by matching experimental and analytical microindentation load - displacement curves.

5.3.1 Specific sensitivity analysis

The sensitivity analysis proposed in Section 5.2 describes a useful overview about how a soft hydrated tissue responds to an harmonic oscillation. Nevertheless, in order to apply an identification procedure to a real case, it is useful to reorganize those selected results.

In Figure 5.13(a) drained modulus $E'^*(0)$ is plotted as a function of the anisotropy ratio λ and parameterized with respect of the out - of - plane Poisson's ratio ν; similarly, in Figure 5.13(b) undrained modulus $E'^*(f \to \infty)$ is presented. $E'^*(0)$ is almost constant with λ but decreases with ν whereas the opposite situation occurs for $E'^*(f \to \infty)$.

Figure 5.14(a) shows how the anisotropy ratio affects the value of the peak of the tangent of the phase shift and Figure 5.14(b) the relation between the same ratio and the frequency at which this peak occours; if the material is isotropic, the peak is lower and occours at lower frequency then in case of high anisotropy.

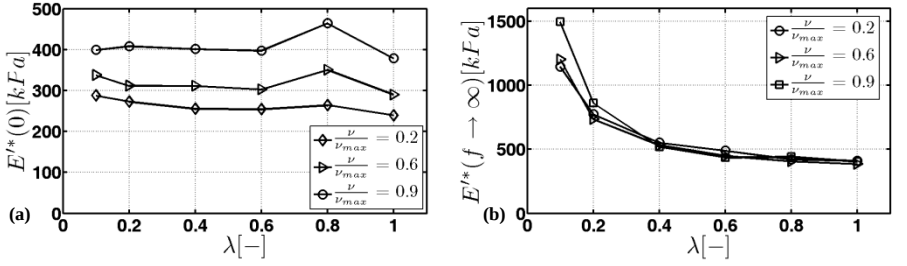

Figure 5.13: (a) $E'^*(0)$ and (b) $E'^*(f \to \infty)$ function of anisotropy ratio λ; parametrized with ratio $\frac{\nu}{\nu_{max}}$.

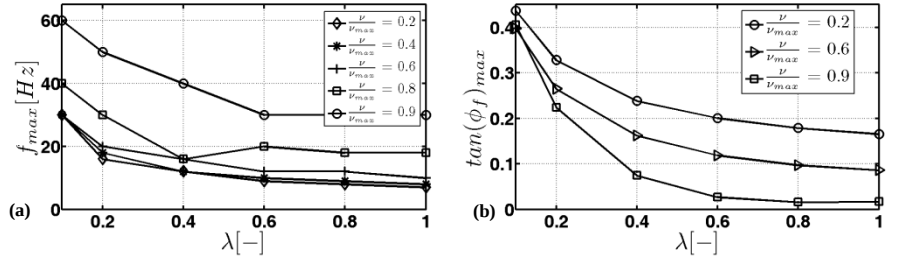

Figure 5.14: (a) $tan(\phi_f)$ and (b) f_{max} function of anisotropy ratio λ; parametrized with ratio $\frac{\nu}{\nu_{max}}$.

Unlikely to the drained and undrained moduli (Figure 5.13), λ and ν affect both the quantities reported in Figure 5.14 in a more complex way. The frequency at peak increases with increasing anisotropy with a repeatible pattern almost independent by ν: this latter parameter rises or lowers the whole curve. The tangent of the phase shift, besides, is less affected by variation in the ratio $\frac{\nu}{\nu_{max}}$ if highly anisotropic case is considered. It is worth to be noted, indeed, that the limit of $\frac{\nu}{\nu_{max}} = 1$ describes a sort of incompressible condition.

Combining the information in Figure 5.13 and Figure 5.14 and keeping fixed the set $[E_a, G, \nu, \eta, k] = \left[200\ kPa, 100\ kPa, 0.15, 0{,}1x10^{-15}\frac{m^4}{Ns}\right]$, in Figure 5.15 the effect of the anisotropy ratio λ on the whole shape of both the storage modulus and the tangent of phase shift is present. In Figure 5.15(b), the dashed line describes the linear trend (in a log - linear graph) of peak of the tangent in function of the frequency. Decreasing in λ corresponds in the increasing of both the difference between drained and undrained conditions as well as the dissipative effects, since the peak in Figure 5.15(b) becomes higher.

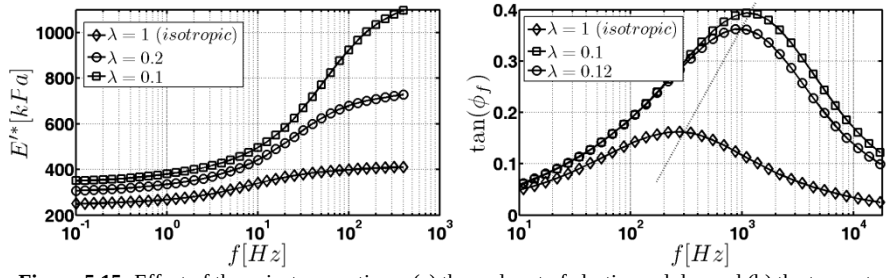

Figure 5.15: Effect of the anisotropy ratio on (a) the real part of elastic modulus and (b) the tangent of phase shift.

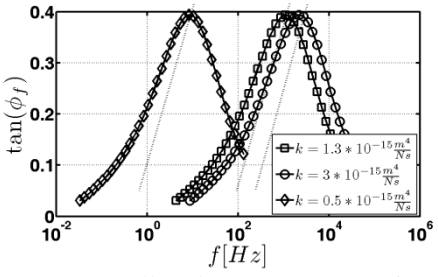

Figure 5.16: Effect of permeability on $tan(\emptyset_f)$.

Figure 5.16 explains the effect of the permeability (fixed constitutive parameters: $[E_a, \nu, k, \alpha] = [200\ kPa, 100\ kPa, 0.15, 0]$); in the plot, $tan(\phi_f)$ is presented in

function of the natural frequency for three different values of parameter k.
The effect of the permeability k is to shift the peak along the frequency axis; greater is k, faster is the phenomenon.
To complete the study, some further remarks: increasing the value of axial stiffness E_a, the magnitude of both drained and undrained moduli increase; vice versa, if it decreases, both the moduli decrease. The axial stiffness has no influence on the characteristic time of the phenomenon. Furthermore, the shear modulus G affects both the ratio $\frac{E'^*(f\to\infty)}{E'^*(0)}$ and the magnitude of the peak: both of these quantities increase, increasing G but with a lower effect than the one due to λ.

5.3.2 Identification of constitutive mechanical parameters of AC

The experimental curves considered in this identification process are presented in Section 4.1; in Figure 5.17 graphs of $E'^*(f)$ and $tan(\phi_f)$ are reported again, for sake of clarity: linear abscissa axis is considered in Figure 5.17(a) while logarithmic one in Figure 5.17(b). Curves refers to the experiments conducted with a tip radius R_{7500} for all the mean indentation depth h_s analyzed.

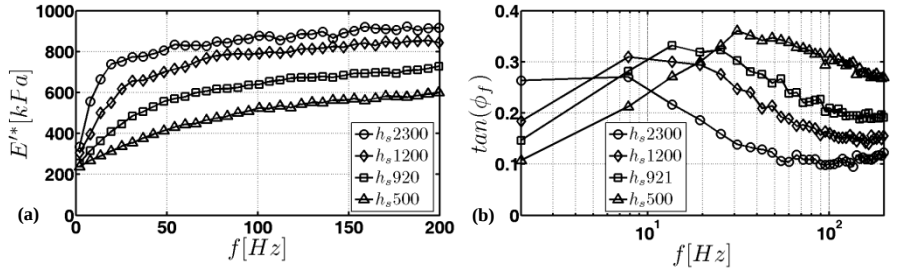

Figure 5.17: Experimental data collected with R_{7500} tip at four mean indentation depths. (a) $E'^*(f)$ and (b) $tan(\emptyset_f)(f)$.

The in - plane Poisson's ratio is set null, $\eta = 0$. All the variables in the set of constitutive parameters $[E_a, G, \nu, k, \alpha]$ have been changed during the best fitting procedure using the rules described below.

1. The axial modulus E_a and the shear modulus G are chosen to have both the drained and undrained conditions of the order of magnitude of the experimental data;
2. The anisotropy ratio λ and the out - of - plane Poisson's ratio ν are chosen in order to adjust the shape of both the graphs $E'^*(f)$ and $tan(\phi_f)(f)$.
3. The permeability k is chosen to have the peak of the tangent of phase shift centered at the correct experimental frequency.

In Figure 5.18(a) and Figure 5.18(b), both the experimental data and the best fitting results are shown.

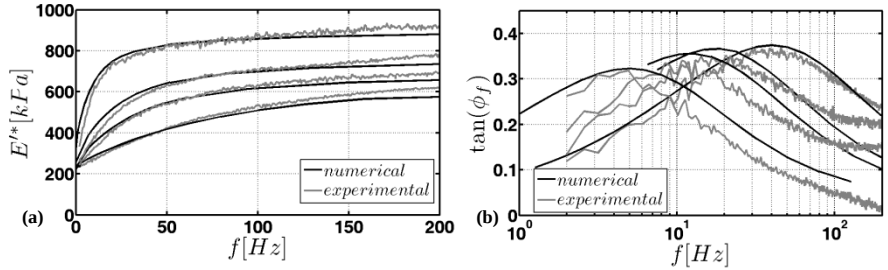

Figure 5.18: Best fitting results for all the analyzed experimental data, in terms of (a) $E'^*(f)$ and (b) $tan(\phi_f)(f)$.

In Table 5.6, the constitutive parameters estimated for all the analyzed experimental data are presented. It seems that elastic properties in the first three cases are almost the same and they differ with respect to the last case.

Table 5.6: Estimated sets of constitutive parameters for all the experimental data with $R_{7500} = 7.5\ \mu m$.

$h_s[nm]$	$E_a[kPa]$	$G\ [kPa]$	$\nu[-]$	$k\left[x10^{-15}\frac{m^4}{Ns}\right]$	$\lambda[-]$	$E'^*(0)[kPa]$
500	180	90	0.04	2	0.16	222
920	150	100	0.05	1.5	0.15	229
1200	170	105	0.05	1.3	0.15	256
2300	200	140	0.06	0.8	0.15	320

Drained storage modulus (through elastic parameters) and permeability are identified separately and independently each other; tip radius and mean indentation depths are known data. Recalling Equation (5.37) and explicating parameter m, the normalized frequency can be written as

$$\bar{f} = \frac{Rh_s}{E'^*(0)k} \tag{5.40}$$

In Figure 5.19 the tangent of phase shift is plotted against the normalized frequency:

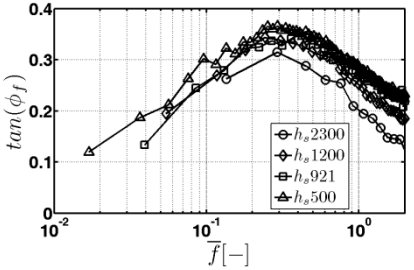

Figure 5.19: Best fitting results for all the analyzed experimental data, in terms of (a) $E'^*(f)$ and (b) $tan(\phi_f)(f)$.

A proper normalization is used for each curve: in this framework, the peaks are centered at the same value, consistently with the poroelastic behavior already explained for this set of data (Section 4.1).

5.3.3 Discussion

A novel method for the estimation of poroelastic constitutive parameters of AC, and soft hydrated tissues in general, has been presented: it is based on the coupling between experimental and numerical results on DMA AFM - based spherical nanoindentation. The tissue is modeled as a transversely isotropic poroelastic material with isotropic and strain - independent permeability. A specific sensitivity analysis, that extends the results obtained in Section 5.2, is performed in order to better highlight how the five parameters considered affect the global quantities extracted experimentally. Almost the whole range of frequency experimentally investigated are here considered, $f = [2 - 200]Hz$. The study of the behavior at high frequency is useful to understand the effects of impact and fast torsion in sports, as explained by Buckwalter (Buckwalter, 2002).

This further analysis proves again all the criticism related to the choice of constitutive parameters, when applied to an identification process with real data.

New interesting correlations have been extracted. Once axial elastic modulus and shear modulus are fixed, the drained behavior is driven only by the out - of - plane Poisson's ratio whereas the undrained behavior by the anisotropy ratio; then, it is possible to identify them separately. Also the permeability can be uniquely estimated since the characteristic time of the experiment is well defined by the frequency at which the peak of the tangent of phase shift occurs. Within the limitations of the proposed model, these three rules define an easy and clear way towards the identification. Anisotropy ratio and out - of - plane Poisson's ratio affect the peak of the tangent of phase shift in an opposite way: increasing parameter λ, the magnitude of the peak increases; increasing parameter ν, the magnitude decreases.

The experimental data have been discussed and explained in Section 4.1, together with their agreements with literature results. According to the depth dependent properties of AC (Chen, Bae, Schinagl, & Sah, 2001), experimental data show both drained and undrained moduli increasing with the mean indentation depth; the effect of the depth can be also seen looking at the magnitude and the position of the peak: both of these measures are lower if the mean indentation depth is higher. The estimated out - of - plane Poisson's ratio ($\upsilon \sim 0.05$) seems to be constant through a thickness up to $2300\,nm$ as well as the anisotropy ratio ($\lambda \sim 0.15$); besides, the permeability shows a slight decrease with the indentation depth, whereas the drained modulus itself increases. Even if the identification process proposed by Nia (Nia, Han, Li, Ortiz, & Grodzinsky, 2011) is focused on a smaller characteristic length ($\sim$1.7 μm versus experiments considered here ranging from 2.6 μm to 5.4 μm) and young bovine AC is considered, the parameters estimation found in this Section are consistent with those results: in her work, she uses a fiber reinforced model, finding

$E_{m,NIA} = 0.032\ MPa$, $E_{f,NIA} = 0.29\ MPa$ and $k_{NIA} = 1.3x10^{-14}\frac{m^4}{Ns}$, referring to the matrix stiffness, the fiber stiffness and the permeability, respectively. A unique Poisson's ratio equal to 0.1 is imposed. Considering the increasing trend of the elastic properties with the depth (or, more in general, with the characteristic length) it can be expected higher elastic moduli (axial or transversal) for larger contact lengths; however, since fibers in superficial layer are mostly parallel to the surface, $E_{m,NIA}$ can be related to the axial stiffness whereas $E_{f,NIA}$ to the transversal one: those values differ of almost a factor 10, very close to an anisotropy ratio of 0.15 found here. Regarding permeability, instead, values of an order of magnitude lower are identified; the explanation can be found looking at the different lengths investigated. The work of Lu (Lu, Wan, Guo, & Mow, 2010) studies the effect of aspect ratio (ratio between the ratio of a flat punch indenter and the sample thickness) on indentation creep tests at millimetric characteristic length; the agreement between numerical results and experimental data is found using an aggregates modulus of $0.24\ MPa$, a Poisson's ratio equal to 0.15 and a permeability of $1.5x10^{-15}\frac{m^4}{Ns}$. These values are completely in accordance with the proposed ones in Table 5.6.

An improvement with respect to the suggested references is that this work give also the possibility to manage the Poisson's ratios that allows to look for a more complete description of the tissue.

No frequency dependent properties are taken into account; however, the good agreement found between experimental and numerical results and the conclusions provided in the work of Park (Park, Costa, Ateshian, & Hong, 2009) suggests that the mechanical properties do not vary with the frequency, at least in the proposed ranges of lengths and frequencies.

According with the microstructure of the tissues, some hypotheses can be proposed: the constancy of the anisotropy ratio can be explained with the fact that the fibers distribution of the considered layers remain almost constant up to $2300\ nm$ of depth; the increasing on the elastic properties can be due, then, not to a change in the material but to different ways (i.e. different deformation applied) in the recruitment of the components, mainly collagen fibers bundles.

The procedure presented here use an inverse approach to estimate constitutive parameters. Only one indentation is required to estimate all of them, reducing drastically the amount of material to be tested and of time to use for the analysis. The homemade developed software for the simulation of DMA nanoindentation tests simulates the problem directly in the frequency domain, overcoming the time consuming aspect (i.e., waiting for the achievement of steady state condition) of the implementation in the time domain. The interest is with specific regard to the effect of material anisotropy and of the characteristic size of the experiment: the anisotropic properties and tissue permeability affect the dynamic response to dynamic indentation in a peculiar fashion along with the geometric features of the

test. As widely explained in Chapter 1, the hierarchical structure of cartilage shows both time scale dependence and length scale dependence. The different structure, from single macromolecules to representative volume elements, interact each other in different ways as response of different solicitations. For example, by comparing the different response, at the same scale, of different tissues (i.e. native vs osteoarthritic or native vs engineered) this identification technique shows that the proposed poroelastic numerical model can be used for the extraction of mechanical properties and, potentially, for the early detection of pathologies as well as for the validation of engineered tissues.

REFERENCES

Ateshian, G., & Weiss, J. (2010). Anisotropic hydraulic permeability under finite deformation. *Journal of Biomechanical Engineering, 132*.

Boschetti, F., Pennati, G., Gervaso, F., Peretti, G., & Dubini, G. (2004). Biomechanical properties of human articular cartilage under compressive loads. *Biorheology, 41*, 159-166.

Buckwalter, J. (2002). Articular cartilage injuries. *Clinical Orthopaedics and Related Research, 402*, 21-37.

Castello, D., Rochinha, F., Roitman, N., & Magluta, C. (2008). Constitutive parameter estimation of a viscoelastic model with internal variables. *Mechanical Systems and Signal Processing, 22*, 1840-1857.

Chen, A., Bae, W., Schinagl, R., & Sah, R. (2001). Depth- and strain-dependendent mechanical and electromechanical properties of full-thickness bovine articular cartilage in confined compression. *Journal of Biomechanics, 34*(1), 1-12.

Cheng, Y., Ni, W., & Cheng, C. (2006). Nonlinear analysis of oscillatory indentation in elastic and viscoelastic solids. *Physical Rewiev Letters, 97*.

Cowin, S., & Doty, S. (2006). *Tissue Mechanics.* New York: Springer Verlag.

Delafargue, A., & Ulm, F. (2004). Explicit approximations of the indentation modulus of elastically orthotropic solids for conical indenters. *International Journal of Solids and Structures, 41*, 7351-7360.

Federico, S., & Gasser, T. (2010). Nonlinear elasticity of biological tissues wth statistical fibre orientation. *Journal of the Royal Society Interface, 7*, 955-966.

Federico, S., & Herzog, W. (2008). On the anisotropy and inhomogeneity of permeability in articular cartilage. *Biomechanics and Modeling in Mechanobiology, 7*, 367-378.

Galli, M., & Oyen, M. (2009). Fast identification of poroelastic parameters from indentation tests. *Computer Modeling in Engineering and Science, 48*, 241-268.

Han, L., Frank, E., Greene, J., Lee, H., Hung, H., Grodzinsky, A., & Ortiz, C. (2011). Time-Dependent Nanomechanics of Cartilage. *Biophysical Journal, 100*, 1846-1854.

Jurvelin, J., Buschmann, M., & Hunziker, E. (2003). Mechanical anisotropy of the human knee articular cartilage in compression. *Proceedings of the Institution of Mechanical Engineers, Part H, 217*(3), 215-219.

Kiviranta, P., Lammentausta, E., Toyras, J., Kiviranta, I., & Jurvelin, J. (2008). Indentation diagnostic of cartilage degeneration. *Osteoarthritis and Cartilage, 16*(7), 796-804.

Lei, F., & Szeri, A. (2007). Inverse analysis of constitutive models: Biological soft tissues. *40*, 936-940.

Lu, X., Wan, L., Guo, X., & Mow, V. (2010). A linearized formulation of triphasic mixture theory for articular cartilage and its application to indentation analysis. *Journal of Biomechanics, 43*, 673-679.

Miller, G., & Morgan, E. (2010). Use of microindentation to characterize the mechanical properties of articular cartilage: comparison of biphasic material properties across length scales. *Osteoarthritis and Cartilage, 18*, 1051-1057.

Namani, R., Simha, N., & Lewis, J. (2003). Nonlinear elastic parameters of articular cartilage. *Summer Bioengineering Conference.* Key Biscayne.

Nia, H., Han, L., Li, Y., Ortiz, C., & Grodzinsky, A. (2011). Poroelasticity of cartilage at the nanoscale. *Biophysical Journal, 101*, 2304-2313.

Olberding, J., & Suh, J. (2006). A dual optimization method for the material parameter identification of a biphasic poroviscoelastic hydrogel: potential application to hypercompliant soft tissues. *Journal of Biomechanics, 39*, 2468-2475.

Park, S., Costa, K., Ateshian, G., & Hong, K. (2009). Mechanical properties of bovine articular cartilage under microscale indentation loading from atomicc force microscopy. *Proceedings of the Institution of Mechanical Engineers. Part H, Journal of Engineering in Medicine, 223*(3), 339-347.

Shirazi, R., Vena, P., Sah, R., & Klisch, S. (2011). Modeling the collagen fibril network of biological tissues as a nonlinear elastic material using a continuous volume fraction distribution function. *Mathematics and Mechanics of Solids, 16*, 706-715.

Simon, B. (1992). Multiphase poroelastic finite element models for soft tissue structures. *Applied Mechanics Reviews, 45*, 191-218.

Terzaghi, V. (1943). *Theoretical soil mechanics.* New York: Wiley.

Zienkiewicz, O., & Taylor, R. (2000). *The Finite Element Method, Fifth Edition, Volume 1: The Basis.* Oxford, United Kingdom: Butterworth - Heinemann.

Chapter 6.

Poroviscoelastic FEM including Continuous Fibers Distribution

In this Chapter a poroviscoelastic constitutive relationship that includes a continuous fiber distribution is considered and its numerical implementation in a User MATerial subroutine is described.

Section 6.1 is dedicated to the description of the relation, showing values for the mechanical parameters consistent with literature results; Section 6.2 shows relevant numerical implementation issues; in Section 6.3 the sensitivity analysis (geometrical parameters of fibers distribution) based on unconfined compression test is presented; in Section 6.4 results from sensitivity analysis is applied to a nanoindentation problem.

In Chapter 2, models for the description of the behavior on AC have been presented but only few of them consider the effect of all the tissue constituents. Moreover, they are often validated by the use of experimental tests at macroscale as tension, compression or indentation; Wilson (Wilson, van Donkelaar, van Rietbergen, & Huiskes, 2005), in particular, shows a wide range of results collected at macroscale. From a numerical point of view, simulation of nanoindentation test introduces more difficulties than tests at macroscale due to the high nonlinearities induced by the deformation field around the tip. In general, rigorous numerical approach can overcome all the troubles related to the experimental approach, helping a better understanding of experimental data.
The experimental work presented by Han (Han, et al., 2011) states that intrinsic properties (mainly, viscosity) and extrinsic properties (mainly, porosity) work in different ways, depending on the characteristic lengths of the experiment. The dichotomy between viscoelasticity and poroelasticity is a more recent topic. In 1963, Elmore (Elmore, Skoloff, Norris, & Carmeci, 1963) states that the response, in case of macroscopic indentation test, is primary due to the fluid exudation. The work of Huang (Huang, Mow, & Ateshian, 2001) and Hu (Hu, Zhao, Vlassak, & Suo, 2010) propose quantitative correlations based on the study of elastomeric gels behavior. For these reasons, the effect of the characteristic length of the experiment can not be neglected: in modeling AC viscous and porous aspects have to be considered within the description of the single components.
In this Chapter a poroviscoelastic with continuous fiber distribution model is implemented in the finite element commercial code Abaqus 6.8-EF1 (Simulia, Providence, RI, USA) with the purpose to simulate nanoindentation tests. This model is developed from the one presented by Shirazi (Shirazi, Vena, Sah, & Klisch, 2011). The aim of the numerical model presented here is to determine the relationship between the properties of the tissues (constitutive parameters), the geometrical feature of the experiments (nanoindenter tip radii) and the mechanical response of the nanoindentation experiment in the time domain. The final purpose of the model is to identify the values of input parameters which best fit the experimental results presented in Section 4.2, collected from multiload nanoindentation creep test with $R_{400} = 400\ \mu m$ radius.
First, a sensitivity analysis is performed using stress relaxation unconfined compression test keeping fixed the constitutive parameters of the material and varying the shape of fiber distribution. Material parameters are chosen in agreement with literature data. The purpose is to have idea about the overall behavior of the material and to suggest a way to use simple confined compression test to set up the more complex nanoindentation simulation.

6.1 DESCRIPTION OF THE CONSTITUTIVE RELATIONSHIP

In this Section, the peculiar aspects of the constitutive relation as well as the relevant numerical details regarding its implementation in a *User defined MATerial (UMAT)*

routine are shown. First, the mechanical parameters, related to the single constituents are presented; then, the numerical issues are pointed out.

6.1.1 Mechanical constitutive parameters

The mechanical constitutive parameters refer to the major tissue constituents that play a role in the mechanical response of AC: collagen (COL), glycosaminoglycans (GAGs) and matrix (MAT).

- $\widehat{\boldsymbol{\alpha_1}}[\boldsymbol{MPa}]$, $\boldsymbol{\alpha_2}[-]$. *GAGs parameters.*

The relationship between the swelling pressure, π^{GAGs}, and the GAGs density in a reference configuration, ρ_0^{GAGs}, is

$$\pi^{GAGs} = \alpha_1(\rho_0^{GAGs})^{\alpha_2} \tag{6.1}$$

The consequent Cauchy stress can be computed as

$$\boldsymbol{\sigma}^{GAGs} = \alpha_1 \left(\frac{\rho_0^{GAGs}}{J}\right)^{\alpha_2} \boldsymbol{I} \tag{6.2}$$

Since the information on ρ_0^{PGs} is not known for the specific tissue over which the identification process will be applied, Equation (6.2) is rearranged as follow

$$\boldsymbol{\sigma}^{GAGs} = \alpha_1 \left(\frac{\rho_0^{GAGs}}{J}\right)^{\alpha_2} \boldsymbol{I} = \alpha_1(\rho_0^{GAGs})^{\alpha_2} \left(\frac{1}{J}\right)^{\alpha_2} \boldsymbol{I} = \widehat{\alpha_1} \left(\frac{1}{J}\right)^{\alpha_2} \boldsymbol{I} \tag{6.3}$$

where the new parameter $\widehat{\alpha_1}$ summarizes also the information on the density.
According to Equation (6.1), parameter $\widehat{\alpha_1}$ is the swelling pressure in reference configuration and a proper value can be extracted from the work of Chahine (Chahine, Chen, Hung, & Ateshian, 2005): the relation between the swelling pressure π^{GAGs} (or osmotic pressure) and the fixed charge density FCD (or c^F) is extracted for different saline concentrations as shown in Figure 6.1; FCD is, namely, the GAGs density. The physiological value for the saline concentration is 0.15 M.

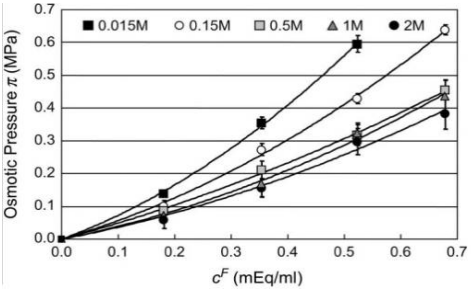

Figure 6.1: Swelling pressure in dependence on fixed charged density and parameterized in term of the bath concentration Reprinted from Biophysical Journal, 83, Chahine, Chen, Hung, Ateshian, Direct measurement of osmotic pressure of glycosaminoglycan solutions by membrane osmometry at room temperature, 1546, Copyright (2005), with permission from Elsevier [OR APPLICABLE SOCIETY COPYRIGHT OWNER].

The work of Ateshian (Ateshian, Rajan, Chahine, Canal, & Hung, 2009), supported by the work of Lu (Lu & Mow, 2008), suggests that mature bovine AC has typical values for c^F ranging in between 0.04 $\frac{mEq}{l}$ and 200 $\frac{mEq}{l}$. A more precise value can be found in the work of Han (Han, Chen, Klisch, & Sah, 2011) in which the value of 100 $\frac{mEq}{l}$ at 0% strain is proposed as characteristic of the whole AC sample: from the knowledge on the structure of AC at microscale (Buckwalter, Mankin, & Grodzinsky, 2005), GAGs concentration is lower in the superficial layer and, consequently, c^F should be a bit lower than the averaged value of 100 $\frac{mEq}{l}$. Choosing $c^F = 100\ \frac{mEq}{l}$ in Figure 6.1 and moving on the proper curve, a value of $\widehat{\boldsymbol{\alpha_1}} = \mathbf{0.07}\ \boldsymbol{MPa}$ is considered as a given input for the simulations. Swelling strains along axial and radial directions obtained through the numerical simulations will be compared with experimental measures of swelling strains reported by Broom (Broom & Flachsmann, 2003), Wang (Wang, et al., 2008) (Wang, Zheng, Niu, & Mak, 2007) and Wilson (Wilson, 2005).

In the work of Buschmann (Buschmann & Grodzinsky, 1995) a PB - cell model for the explanation of the relation between swelling pressure and GAGs concentration is presented. GAGs are modeled as charged cylinders of radius a; the intercharge distance is defined by parameter b and the radial distance between two cylinder is R. In Figure 6.2, the prediction of PB-cell model for varying parameters a and b is shown.

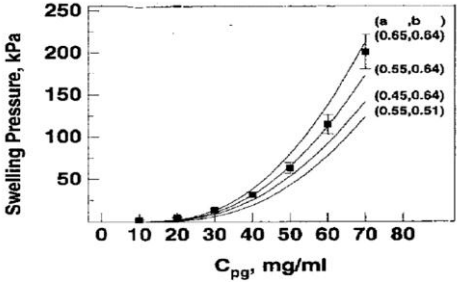

Figure 6.2: Swelling pressure in dependence on concentration of GAGs (Buschmann & Grodzinsky, 1995).

In the same cited work, the equilibrium modulus computed for uniaxial confined compression test on adult bovine sample is measured in function of the molarity of the solution in which the sample is submerged. A best fitting is obtained using the following parameters of PB - cell model: $a = 0.55\ nm, b = 0.64\ nm, R = 1.91\ nm$. Hence, it is possible to choose the curve that in Figure 6.2 is relative to the proposed parameters and to apply a best fitting procedure based on Equation (6.1): it is worth to be noted that $\rho_0^{GAGs} = C_{pg}$ to match the notation used in Buschmann. The result of the best fitting procedure is presented in Figure 6.3.

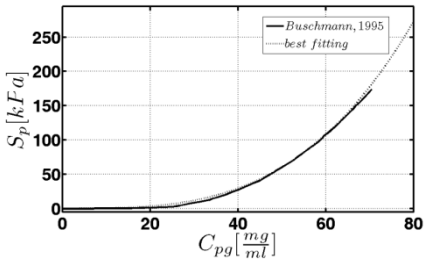

Figure 6.3: Best fitting of the selected numerical curve from Buschmann (Buschmann & Grodzinsky, 1995)

The best fitting parameters are: $\alpha_1 = 0.000203\ kPa \frac{ml}{mg}^{\alpha_2}$, $\boldsymbol{\alpha_2}[-] = \mathbf{3.22}$. Since the parameter α_1 is overcome by parameter $\widehat{\alpha_1}$ in the proposed formulation, this best fitting procedure allows to identified parameter α_2 that will be kept fixed further on.

- $\boldsymbol{\mu}\ [\boldsymbol{MPa}]$. *MAT shear modulus*.

The work of Buckley (Buckley, Glghorn, Bonasser, & Cohen, 2008) shows that the static shear modulus G_s of the most superficial AC layers is in the range $[0.20 - 0.25]\ MPa$; this value belongs to the tissue as a whole, so it is not referred to the properties of the sole matrix. The experimental condition used by Buckley consists in a precompression step of a 2.5% of the total thickness and a following application of an angular displacement $u_{r,3} = 0.023\ rad$ (equivalent of a shear strain of 2.3%). The consequent shear modulus is computed as

$$G_s = \frac{M_t L}{J_{zz} u_{r,3}} \tag{6.4}$$

where L is the thickness of the specimen, M_t is the torque and $J_{zz} = \frac{1}{2}\pi r^4$ is the moment of inertia for a disk of radius r.

A preliminary simulation of torsion test, the details of which will be described further, is done in order to set up the proper value of μ that, combined with the particular fiber distribution chosen, returns a shear modulus $G_s \sim [0.20 - 0.25]\ MPa$.

- $\boldsymbol{k(e)}\ \left[\frac{\boldsymbol{\mu m}}{\boldsymbol{s}}\right]$. *Permeability, as required by Abaqus*

From the experimental tests performed on the particular AC tissue shown in Section 4.2, a relation between permeability k and equivalent strain ε_{eq} has been found as follow:

$$k(\varepsilon_{eq}) = k_0 exp^{-k_1 \varepsilon_{eq}} = 10^{-7} exp^{-3.06\varepsilon_{eq}} \tag{6.5}$$

where ε_{eq} is the equivalent deformation. According to the work of van der Voet (van der Voet, 1997), the relation $k(e)$ is obtained from the parameters k_0 and k_1 found in Equation (6.5). In particular,

$$k(e) = k_0 \left(\frac{1+e}{1+e_0}\right)^{k_1} \quad (6.6)$$

where e is the current void ratio and e_0 is the initial void ratio. Since the time dependent response of AC is due on the interaction between poroelastic and viscoelastic effects, the value of e_0 can be adjusted in order to obtain results more similar to the experimental ones, if needed.

- $\boldsymbol{E_1[MPa] = 340.5, E_2[MPa] = 2.737, \eta\,[MPa\ s] = 1643}$. *The single bundle of collagen fibers is modeled by the use of a Standard Linear Solid (SLS) as in Figure 6.4.*

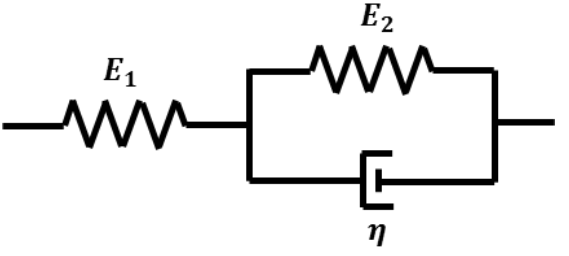

Figure 6.4: Standard Linear Solid model.

In the work of Wilson (Wilson, van Donkelaar, van Rietbergen, & Huiskes, 2005), the authors identify a set of parameters for a SLS configuration suitable for AC modeling. Rearranged them consistently with the model in Figure 6.4, the parameters used in the *UMAT* are: $\boldsymbol{E_1 = 340.5\ MPa, E_2 = 2.737\ MPa, \eta = 1643\ MPa\ s}$. If needed, since the time-dependent response of AC is due on the interaction between poroelastic and viscoelastic effects, values of E_1 and E_2 can be adjusted, keeping fixed the long term response of the SLS element, $E_\infty = \frac{E_1 E_2}{E_1+E_2}$ and its time constant, $\tau_t = \frac{E_2}{\eta}$.

6.1.2 Geometrical parameters

Let us consider the reference systems in Figure 6.5: Figure 6.5(a) shows a 3D Cartesian reference system whereas Figure 5(b) is the 2D reduction. In a 3D framework, the following fiber distribution is assumed

$$\rho(\theta,\varphi) = \frac{1}{V}\left[\left(\frac{sin(\theta)\,cos(\varphi)}{\tilde{a}}\right)^2 + \left(\frac{sin(\theta)\,sin(\varphi)}{\tilde{b}}\right)^2 + \left(\frac{cos(\theta)}{\tilde{c}}\right)^2\right]^{-\beta} \quad (6.7)$$

where $\tilde{a}$, $\tilde{b}$ and $\tilde{c}$ are the semi-axis of an ellipsoid and the variable β provides a generalization of the function proposed by Ateshian (Ateshian, Rajan, Chahine, Canal, & Hung, 2009). V is the total volume of the distribution. In a axisymmetric framework, Equation (6.7) can be reduced as follow

$$\rho(\theta) = \frac{1}{V}\left[\left(\frac{sin(\theta)}{\tilde{a}}\right)^2 + \left(\frac{cos(\theta)}{\tilde{c}}\right)^2\right]^{-\beta} \tag{6.8}$$

It is trivial to say that, if Equation (6.7) want to model axisymmetric distribution applied to a non - axisymmetric problem, the consequent distribution is equal to distribution in Equation (6.8) with $\tilde{a} = \tilde{b}$; this will be the case analyzed in this Chapter when a 3D model is used.
Set $[\tilde{\boldsymbol{a}}\ \tilde{\boldsymbol{c}}\ \boldsymbol{\beta}]$ defines the parameters to be varied in both the sensitivity analysis and the following identification process. Using this approach, $\rho(\theta)$ can be though as a measure of COL fibers density: Wilson (Wilson, van Donkelaar, van Rietbergen, Ito, & Huiskes, 2004), suggests a value for the superficial layer dependent by the condition in the deepest zone whereas Pierce (Pierce, et al., 2010) estimates values for COL fibers density by making use of multiphoton microscopy (Lilledahl, Pierce, Ricken, Holzapfel, & de Lange Davies, 2011).

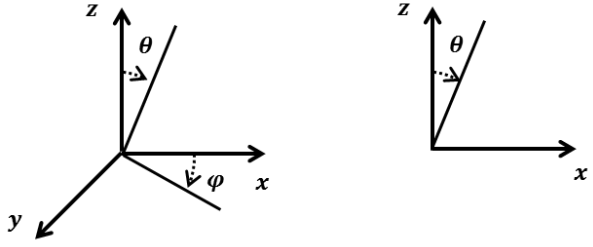

Figure 6.5: (a) 3D and (b) 2D Cartesian reference systems.

6.1.3 Stresses derivation

Let us consider COL, GAGs and MAT in their initial configurations, κ_0^{COL}, κ_0^{GAGs} and κ_0^{MAT} respectively; hence three deformation gradients that bring the components in reference configuration can be defined as $\boldsymbol{F_0^{COL}}$, $\boldsymbol{F_0^{GAGs}}$ and $\boldsymbol{F_0^{MAT}}$. If an initial equilibrium step (swelling step) is imposed to obtain a global stress free condition in which collagen fibers are in tension to balance the swelling pressure, it can be correctly assumed that the unique deformation gradient $\boldsymbol{F}$ provided by Abaqus takes into account the different initial configurations and can be used itself for the constitutive description of the three components separately: this explains why only one deformation gradient tensor is considered in the following Equation.
In reference configuration, the total 2nd Piola Kirchhoff stress $\boldsymbol{S^{TOT}}$ acting in a RVE can be computed as the sum of the contribution of the three components, $\boldsymbol{S^{TOT}} = \boldsymbol{S^{MAT}} + \boldsymbol{S^{COL}} + \boldsymbol{S^{GAGs}}$ where

$$\boldsymbol{S^{MAT}} = \mu(\boldsymbol{I} - \boldsymbol{C^{-1}}) \tag{6.9}$$

is the isotropic matrix contribution (Neo - Hookean material) and

$$\boldsymbol{S^{GAGs}} = -\frac{\widehat{\alpha_1}}{J^{(\alpha_2-1)}}\boldsymbol{C} \tag{6.10}$$

is the GAGs contribution. $\boldsymbol{C}$ is the right Cauchy Green tensor, J is the Jacobian of the transformation defined by $\boldsymbol{F}$ and $\boldsymbol{I}$ is the identity tensor.
Using a push forward operation, stresses in current configuration can be derived as, respectively,

$$\boldsymbol{\sigma^{MAT}} = \frac{\mu}{J}(\boldsymbol{b} - \boldsymbol{I}) \tag{6.11}$$

$$\boldsymbol{\sigma^{GAGs}} = -\frac{\widehat{\alpha_1}}{J^{\alpha_2}}\boldsymbol{I} \tag{6.12}$$

where $\boldsymbol{\sigma}^i$ indicates the Cauchy stress for the *i - th* component and $\boldsymbol{b}$ is the left Cauchy Green tensor.
$\boldsymbol{S^{COL}}$ is the portion of stress deputed to COL. Let us consider the reference system in Figure 6.5(a). A generic direction $\boldsymbol{n}$ in 3D space can be computed as follow

$$\boldsymbol{n} = \begin{bmatrix} sin(\theta)cos(\varphi) \\ cos(\theta) \\ sin(\theta)sin(\varphi) \end{bmatrix} = \begin{bmatrix} n_1 \\ n_2 \\ n_3 \end{bmatrix} \tag{6.13}$$

where n_1 is the contribution along x - direction, n_2 along z - direction and n_3 y - direction. The vector is defined in reference configuration so it does not change with the applied transformation.
The 2nd Piola Kirchhoff stress $\boldsymbol{S^{COL}}$ is built as summation of the contributions in all the directions $\boldsymbol{n}$, sweeping a sphere of total volume V; the angles θ and φ range, respectively, in $[0 - \pi]$ and $[0 - 2\pi]$. In Voigt notation, the generic component of stress becomes

$$S_{IJ}^{COL} = \int_{V_s} \bar{S}\widetilde{H}\rho(\theta,\varphi)n_I(\theta,\varphi)n_J(\theta,\varphi)dV \tag{6.14}$$

where V_s is the pyramidal volume reference.
$\widetilde{H}$ indicates a modified Heaviside function that describes the activation rule for the fibers and it will be presented in the next section; dV is the infinitesimal volume such that $dV = \frac{1}{3}sin(\theta)d\theta d\varphi$.
$\bar{S}$ is the stress along the selected direction and it is derived from the 1D differential constitutive equation for the SLS model presented in Figure 6.4:

$$\eta\dot{\bar{S}} + (E_1 + E_2)\bar{S} = \eta E_1\dot{\lambda} + E_1E_2\lambda \tag{6.15}$$

where λ is the stretch along the selected direction as $\lambda = \frac{1}{2}n_H(\theta,\varphi)n_K(\theta,\varphi)(C_{HK} - 1) = n_H(\theta,\varphi)n_K(\theta,\varphi)E_{HK}$. E_{HK} is the generic component of the Green Lagrange strain tensor.
Equation (6.15) is an implicit form: in the next Section a numerical discretization is presented. Inserting Equation (6.15) in (6.14), the generic component becomes

$$S_{IJ}^{COL} = \frac{1}{3}\int_0^{2\pi}\int_0^{\pi} \bar{S}\widetilde{H}\rho(\theta,\varphi)n_I(\theta,\varphi)n_J(\theta,\varphi)sin(\theta)d\theta d\varphi \tag{6.16}$$

In an axisymmetric framework, the behavior of the material is independent by

direction φ. This means that stretch λ can be computed using $\boldsymbol{n_{stretch}}$ (instead of $\boldsymbol{n}$):

$$\boldsymbol{n_{stretch}} = \begin{bmatrix} sin(\theta) \\ cos(\theta) \\ 0 \end{bmatrix} \tag{6.17}$$

and the fiber distribution depends only on the angle θ as shown in Equation (6.8). Then, Equation (6.16) is simplified by separating the dependence on the two angles as follow

$$S_{IJ}^{COL} = \frac{1}{3}\bar{S}H \int_0^{2\pi} \Gamma(\varphi)d\varphi \int_0^{\pi} \rho(\theta)\lambda\Psi(\theta)sin(\theta)d\theta \tag{6.18}$$

where $\Gamma(\varphi)$ and $\Psi(\theta)$ are particular functions depending on the direction chosen. Equation (6.18) is a simplification of Equation (6.16) since $\int_0^{2\pi} \Gamma(\varphi)d\varphi$ has an analytical solution for any $\bar{\varphi}$. In order to clarify these last two functions, an example is shown.

Let us consider the contribution to the component S_{12}^{COL} of the generic direction $(\bar{\theta}, \bar{\varphi})$. The product $n_1(\theta,\varphi)n_2(\theta,\varphi)$ becomes

$$n_1(\bar{\theta},\bar{\varphi})n_2(\bar{\theta},\bar{\varphi}) = sin(\bar{\theta})cos(\bar{\varphi})cos(\bar{\theta}) = \Gamma(\bar{\varphi})\Psi(\bar{\theta}) \tag{6.19}$$

where

$$\Gamma(\bar{\varphi}) = cos(\bar{\varphi}) \tag{6.20}$$

$$\Psi(\bar{\theta}) = sin(\bar{\theta})cos(\bar{\theta}) \tag{6.21}$$

In the numerical implementation, stresses are requested in current configuration: applying the push forward transformation to Equation (6.18) it can be obtained

$$\sigma_{ij}^{COL} = \frac{1}{J}F_{iI}S_{IJ}^{COL}{F_{jJ}}^T \tag{6.22}$$

The fiber activation function $\widetilde{H}$ is described by the following piecewise function:

$$\begin{matrix} \widetilde{H} = coem \\ d\widetilde{H} = 0 \end{matrix} \; if\ \lambda < lim \tag{6.23}$$

$$\begin{matrix} \widetilde{H} = (1 - coem)\left\{sin^2\left[\frac{\pi(\lambda - lim)}{2(\lambda_C - lim)}\right]\right\} + coem \\ d\widetilde{H} = \frac{\pi(1-coem)}{(\lambda_C - lim)} sin\left[\frac{\pi(\lambda - lim)}{2(\lambda_C - lim)}\right] cos\left[\frac{\pi(\lambda - lim)}{2(\lambda_C - lim)}\right] \end{matrix} \; if\ lim < \lambda < \lambda_C \tag{6.24}$$

$$\begin{matrix} \widetilde{H} = 1 \\ d\widetilde{H} = 0 \end{matrix} \; if\ \lambda < lim \tag{6.25}$$

The values used for the simulations showed in this Chapter are: $coem = 0$, $lim = 1$ and $\lambda_C = 1.01$. This regularization function is introduced to mitigate the strong non - linearities that could be due to the *on - off* Heaviside function.

6.2 NUMERICAL ISSUES

In this Section, issues related to the numerical implementation are presented, limiting to the most relevant aspects.

6.2.1 Discretization of angle coordinate Θ

Since this work is focused on the superficial layers of AC, the fibers distribution has to be markedly anisotropic, to obtain the direction parallel to the surface stiffer than the perpendicular one: that means $\rho\left(\theta=\frac{\pi}{2}\right) \gg \rho(\theta=0)$. For sake of computational effectiveness, the distribution function has been unevenly sampled: the sampling point distribution is denser in region with higher gradients, as shown in Figure 6.6(b).

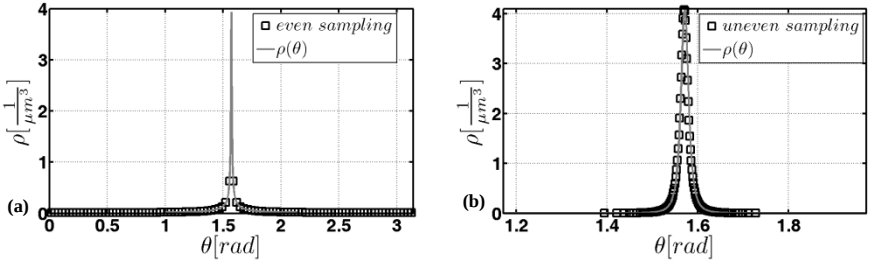

Figure 6.6: (a) even sampling and (b) uneven sampling for a generic anisotropic fibers distribution.

It is worth to be noted that, in the case of Figure 6.6(a), the peak is not caught.

3.4.1 Discretization of the collagen stress $\bar{S}$

The expression in Equation (6.15) can be discretized using a central difference scheme (no computations are shown):

$$\overline{S_{t_2}} = \left(1+\frac{E_1E_2}{\frac{E_1+E_2}{2}+\frac{\eta}{\Delta t}}\right)\overline{S_{t_1}} + \left(\frac{1}{\frac{E_1+E_2}{2}+\frac{\eta}{\Delta t}}\right)\left[E_1E_2\lambda_{t_1} + \left(\frac{\eta}{\Delta t}+\frac{E_1+E_2}{2}\right)\Delta\lambda\right] \tag{6.26}$$

where t_2 is the current time, t_1 the previous time, $\Delta t = t_2 - t_1$ the time step, λ_{t_1} the stretch at previous time and $\Delta\lambda = \lambda_{t_2} - \lambda_{t_1}$ with λ_{t_2} the stretch at the current time. $\overline{S_{t_2}}$ is the stress computed at current time and $\overline{S_{t_1}}$ the stress computed at previous time. Equation (6.26) holds for the generic angle $\bar{\theta}$.

The numerical derivative for the stress is used to compute the stiffness tangent matrix (as shown further on):

$$\frac{\Delta\bar{S}}{\Delta\lambda} = \left(\frac{1}{\frac{E_1+E_2}{2}+\frac{\eta}{\Delta t}}\right)\left(\frac{\eta}{\Delta t}+\frac{E_1+E_2}{2}\right) \tag{6.27}$$

6.2.3 Derivation of the stiffness tangent matrix

The implementation of this constitutive law into the commercial finite element code Abaqus requires the computation of the correct stiffness tangent matrix; in the case of constitutive laws in total form, the consistent tangent matrix $\mathbb{C}_{ijhk}$ is computed through the variation of the Kirchhoff stress $\boldsymbol{\tau}$. The whole derivation is not reported here.

The final expression of the stiffness tangent matrix is

$$\mathbb{C}_{ijhk} = \frac{1}{J}\left[\frac{1}{2}\left(\delta_{ki}\tau_{hj} + \delta_{hj}\tau_{ik} + \delta_{hi}\tau_{kj} + \delta_{kj}\tau_{ih}\right) + \mathbb{C}_{IJHK}\, F_{iI}F_{jJ}F_{hH}F_{kK}\right] \tag{6.28}$$

where $\mathbb{C}_{IJHK}$ is the 4th order stiffness tensor in reference configuration computed as $\mathbb{C}_{IJHK} = \frac{\partial S_{IJ}}{\partial C_{HK}}$. The first addendum in Equation (6.28) is the *corotational* part.

According to the proposed derivation, the stiffness tangent matrix is computed for this particular constitutive law.

The generic coefficient of the total Cauchy stress of the material, σ_{ij}^{TOT} is the summation of the three contributions

$$\sigma_{ij}^{TOT} = \sigma_{ij}^{COL} + \sigma_{ij}^{GAGs} + \sigma_{ij}^{MAT} \tag{6.29}$$

Then, in spatial configuration, the corotational part in Equation (6.28) becomes

$$\mathbb{C}_{ijhk}^{Co-TOT} = \frac{1}{2}(\delta_{ki}\sigma_{hj}^{TOT} + \delta_{hj}\sigma_{ik}^{TOT} + \delta_{hi}\sigma_{kj}^{TOT} + \delta_{kj}\sigma_{ih}^{TOT}) \tag{6.30}$$

The 4th order stiffness tensor in reference configuration is derived below for the three components

$$\mathbb{C}_{IJHK}^{MAT} = \frac{\mu}{2}\left(C_{IH}{}^{-1}C_{JK}{}^{-1} + C_{IK}{}^{-1}C_{JH}{}^{-1}\right) \tag{6.31}$$

$$\mathbb{C}_{IJHK}^{GAGs} = \frac{\widehat{\alpha_1}}{J^{(\alpha_2)}}[(\alpha_2 - 1)C_{KH}^{-1}C_{IJ}^{-1} + C_{IH}^{-1}C_{JK}^{-1} + C_{IK}^{-1}C_{JH}^{-1})] \tag{6.32}$$

$$\mathbb{C}_{IJHK}^{COL} = {}^{4}M_{IJHK} + DMg_{IJHK} \tag{6.33}$$

where ${}^{4}M_{IJHK}$ and DMg_{IJHK} are two generalized tensor defined as

$${}^{4}M_{IJHK} = \int_0^{2\pi}\int_0^{\pi} \rho(\theta) H \frac{\Delta\bar{S}}{\Delta\lambda} sin(\theta) n_I(\theta,\varphi) n_J(\theta,\varphi) n_H(\theta,\varphi) n_K(\theta,\varphi)\, d\theta d\varphi \tag{6.34}$$

$$DMg_{IJHK} = \int_0^{2\pi}\int_0^{\pi} \rho(\theta) dH\bar{S} sin(\theta) n_I(\theta,\varphi) n_J(\theta,\varphi) n_H(\theta,\varphi) n_K(\theta,\varphi)\, d\theta d\varphi \tag{6.35}$$

Then, the stiffness tangent matrix in spatial configuration becomes

$$\mathbb{C}_{ijhk} = \mathbb{C}_{ijhk}^{Co-TOT} + \left(\mathbb{C}_{IJHK}^{MAT} + \mathbb{C}_{IJHK}^{GAGs} + \mathbb{C}_{IJHK}^{COL}\right)F_{iI}F_{jJ}F_{hH}F_{kK} \tag{6.36}$$

$\frac{\Delta\bar{S}}{\Delta\lambda}$ is the numerical derivative of collagen stress as in Equation (6.27).

6.2.4 Permeability

The permeability is implemented through the built - in **Soils* solver directly in Abaqus.

6.3 SENSITIVITY ANALYSIS BASED ON CONFINED COMPRESSION TEST

6.3.1 Methods

A preliminary sensitivity analysis is carried out with the purpose to assess the role of parameters governing the fiber distribution on the material response under unconfined compression test.

For any of the fibers distribution analyzed, the test consists in two phases. First, a 3D torsion test on a purely elastic material is performed to set the value of matrix shear modulus μ. In Figure 6.7, initial geometry and boundary conditions are shown.

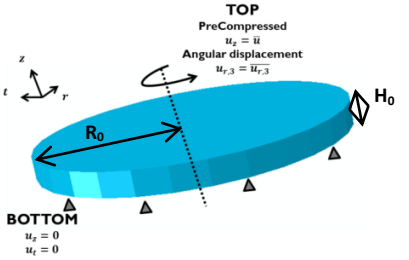

Figure 6.7: Geometry and boundary condition for the simulation of torsion test.

This simulation consists of two steps. First, the swelling is applied without external solicitations: the new sizes of the disk are $R = sw_r R_0$ and $H = sw_a H_0$; then, the disk is compressed of an amount $\overline{u_z} = 0.025H$ and torqued of the specific angular displacement $\overline{u_{r,3}} = 0.023\ rad$ (equivalent of a shear strain of 2.3%). sw_r and sw_a indicate the percentage of swelling in radial (plane xy) and axial (z) directions. As shown in Equation (6.4), μ is not constant for all the fiber distribution but it is varied to maintain a uniform $G_s$in the range $[0.20 - 0.25]\ MPa$.

Once, the matrix shear modulus is found, a stress relaxation unconfined compression test on a poroviscoelastic material is set. In the following Figure, a sketch of the geometry and boundary conditions is presented. *Radial* indicates the x - direction whereas *Axial* indicates the y - direction.

This simulation is organized as follow: 1. the swelling is applied followed by a relaxation step: since the material is poroviscoelastic, a dwell period is allowed to reach equilibrium condition after the swelling pressure is applied. At the end of this step, the new sample sizes are $R = sw_r R_0$ and $H = sw_a H_0$ as dimensions. 2. Six load increments each followed by a dwell period are performed sequentially. The displacements is applied on the upper surface with a constant strain rate $\dot{\varepsilon} = 0.25\ \frac{1}{s}$

for overall compression strains $\varepsilon_{compression,i}$ equal to $[2.5\%, 5\%, 10\%, 15\%, 30\%, 50\%]H$; the subscript $i \in [1,6]$ indicates the load levels. The dwell period to allow for stress relaxation lasts for 120 s.

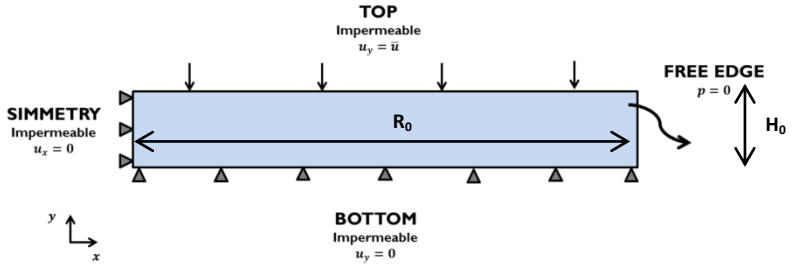

Figure 6.8: Geometry and boundary conditions for the simulation of unconfined compression stress relaxation.

All the constitutive parameters are chosen based on the considerations done in the previous Sections and summarized in Table 6.1.

Table 6.1: Constitutive parameters for articular cartilage.

PGs	$\hat{\alpha}_1 = 0.07\ MPa$
	$\alpha_2 = 3.22$
COL	$E_1 = 340.5\ MPa$
	$E_2 = 2.737\ MPa$
	$\eta = 1643\ MPa\ s$
MATRIX	μ (identified for any distributions)
PERMEABILITY	$k_0 = 10^{-16}\frac{\mu m}{s}$
	$k_1 = 3.06$
	e_0 (identified for any distributions)

The value of the initial void ratio e_0 is chosen in order to have a void ratio $e \sim 7$ at the end of the swelling relax phase.
According to the fibers distribution presented in Equation (6.8), the sensitivity analysis is performed varying the geometrical parameters in the ranges selected: $\tilde{a} \in [4,2,1]$; $\tilde{c} \in [0.1,0.05,0.01]$, with the constraint $\tilde{c} \leq \tilde{a}$; $\beta \in [0.5,1,1.5]$.
The simulations performed are summarized in Table 6.2.
In the subsequent Figures, all the distributions are plotted in function of angle θ. Figures are organized as follow: in Figure 6.9, all the subplots refer to the case $\tilde{c} = 0.1$; in Figure 6.10, all the subplots refer to the case $\tilde{c} = 0.05$; in Figure 6.11, all the subplots refer to the case $\tilde{c} = 0.01$. In each Figure, subplot 1 contains data with $\tilde{a} = 4$, subplot 2 contains data with $\tilde{a} = 2$ and subplot 3 contains data with $\tilde{a} = 1$. Black lines have $\beta = 0.5$, gray lines have $\beta = 1$ and light gray lines have $\beta = 1.5$.

To highlight the behavior in correspondence of $\theta = \frac{\pi}{2}$, direction parallel to the surface, only the interval $\theta \in [1.4 - 1.75]\, rad$ is presented; hence, the value of $\rho(\theta = 0) = \rho(\theta = \pi)$ is indicated in the legend boxes.

Table 6.2: Fibers distributions considered.

			$\boldsymbol{\beta}[-]$		
	$\tilde{\boldsymbol{\alpha}}[-]$	$\tilde{\boldsymbol{c}}[-]$	**0.5**	**1**	**1.5**
FIBERS DISTRIBUTIONS	**4**	**0.1**	I	II	III
	2	**0.1**	IV	V	VI
	1	**0.1**	VII	VIII	IX
	4	**0.05**	X	XI	XII
	2	**0.05**	XIII	XIV	XV
	1	**0.05**	XVI	XVII	XVIII
	4	**0.01**	XIX	XX	XXI
	2	**0.01**	XXII	XXIII	XXIV
	1	**0.01**	XXV	XXVI	XXVII

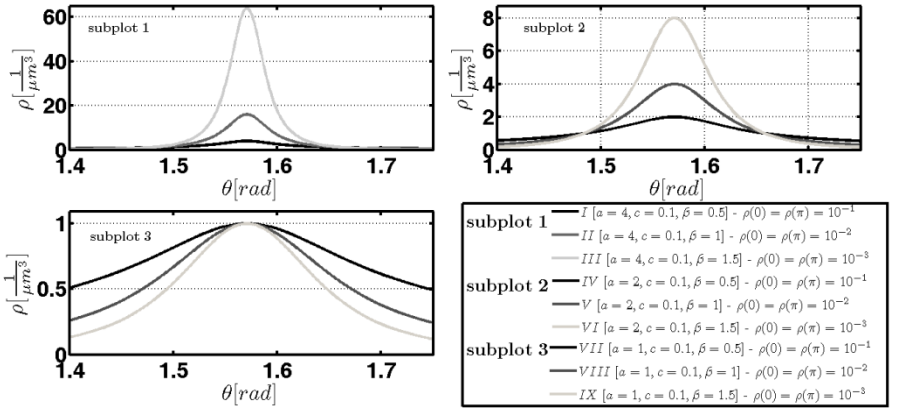

Figure 6.9: Fibers distributions in the case of $\tilde{c} = 0.1$.

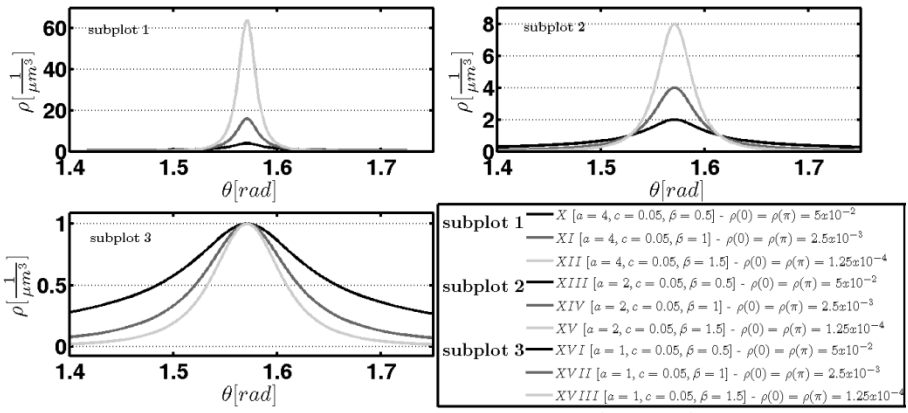

Figure 6.10: Fibers distributions in the case of $\tilde{c} = 0.05$.

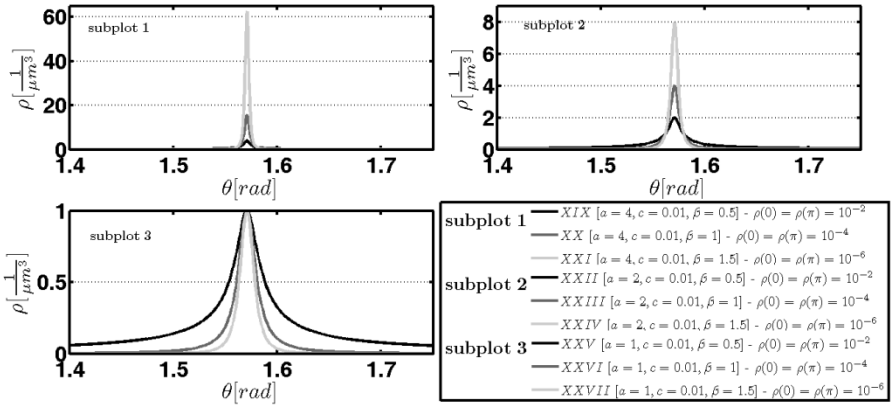

Figure 6.11: Fibers distributions in the case of $\tilde{c} = 0.01$.

To have a complete overview of the analysis a further information is required. In Figure 6.12, the values of the integrals, computed as $Q = 2\pi \int_0^{\pi} \rho(\theta) d\theta$, are shown for all the distributions; this means that the amount of collagen fibers is different among the distributions studied.

The role of the distributions are compared using these parameters.

- $F_{d,max}[kN]$. Reaction force measured at the end of the relaxation phase at the highest strain imposed.
- $\Delta F_{\max}[kN] = F_{u,max} - F_{d,max}$, where $F_{u,max}[kN]$ is the reaction force measured at the beginning of the relaxation phase at highest strain imposed.
- $sw_a[\%] = \frac{u_{s,a}}{H_0} x100$. swelling deformation in axial direction. $u_{s,a}$ is the vertical displacement of the upper layer after the swelling phase; $H_0 =$

1200 μm is the thickness of the sample.

- $sw_r[\%] = \frac{u_{s,r}}{R_0} x100$. swelling deformation in radial direction. $u_{s,r}$ is the in - plane displacement of the outer boundary of the surface after the swelling phase; $R_0 = 8000\ \mu m$ is the radius of the sample.

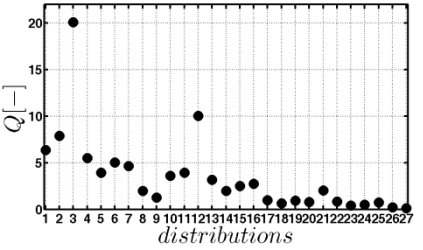

Figure 6.12: Fibers distribution density in all the cases studied.

6.3.2 Results

In the following Tables, the results for all the simulations are shown in terms of swelling: both axial and radial directions are considered. Tables are divided for different values of parameter $\tilde{c}$.

Table 6.3: Amount of swelling for the distributions with $\tilde{c} = 0.1$.

$\tilde{c} = 0.1$	$sw_a[\%]$ $\beta = 0.5$	$sw_a[\%]$ $\beta = 1$	$sw_a[\%]$ $\beta = 1.5$	$sw_r[\%]$ $\beta = 0.5$	$sw_r[\%]$ $\beta = 1$	$sw_r[\%]$ $\beta = 1.5$
$\tilde{a} = 4$	9.57	10.76	10.97	1.67	1.24	0.98
$\tilde{a} = 2$	8.92	10.54	10.63	2.05	2.20	1.80
$\tilde{a} = 1$	9.34	9.98	9.84	2.63	3.66	4.35

Table 6.4: Amount of swelling for the distributions with $\tilde{c} = 0.05$.

$\tilde{c} = 0.05$	$sw_a[\%]$ $\beta = 0.5$	$sw_a[\%]$ $\beta = 1$	$sw_a[\%]$ $\beta = 1.5$	$sw_r[\%]$ $\beta = 0.5$	$sw_r[\%]$ $\beta = 1$	$sw_r[\%]$ $\beta = 1.5$
$\tilde{a} = 4$	9.42	10.42	10.56	2.70	2.18	1.04
$\tilde{a} = 2$	9.36	10.10	10.14	3.05	3.46	2.94
$\tilde{a} = 1$	9.15	9.77	9.60	3.52	4.99	5.73

Table 6.5: Amount of swelling for the distributions with $\tilde{c} = 0.01$.

$\tilde{c} = 0.01$	$sw_a[\%]$ $\beta = 0.5$	$sw_a[\%]$ $\beta = 1$	$sw_a[\%]$ $\beta = 1.5$	$sw_r[\%]$ $\beta = 0.5$	$sw_r[\%]$ $\beta = 1$	$sw_r[\%]$ $\beta = 1.5$
$\tilde{a} = 4$	9.56	9.66	10.07	5.45	5.26	3.36
$\tilde{a} = 2$	9.45	9.48	9.53	5.71	6.57	6.12
$\tilde{a} = 1$	9.38	9.24	9.18	6.00	7.54	7.99

Figure 6.13 contains a visualization of all the data presented above. Figure 6.13(a) refers to the axial swelling, whereas Figure 6.13(b) to the radial swelling, in percentage with respect to the initial sizes.

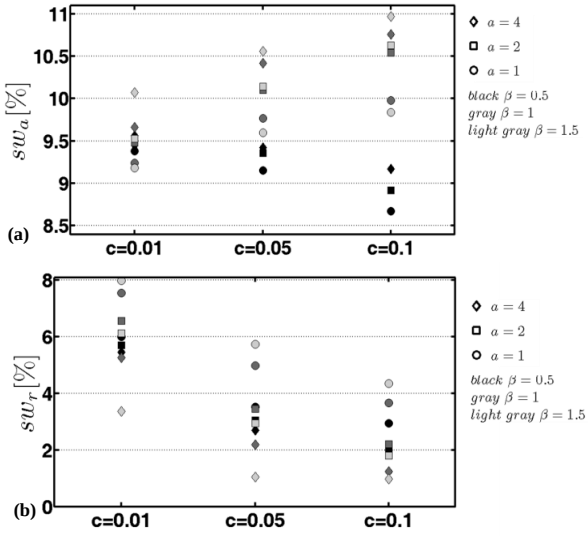

Figure 6.12: Swelling for all the simulation in percentage with respect to the initial lengths: (a) axial and (b) radial.

The drained behavior can be described by the use of the reaction force $F_{d,max}$ measured at the end of the whole simulation (higher strain applied). Figure 6.14 contains this information for all the simulations, organized as in Figure 6.13.

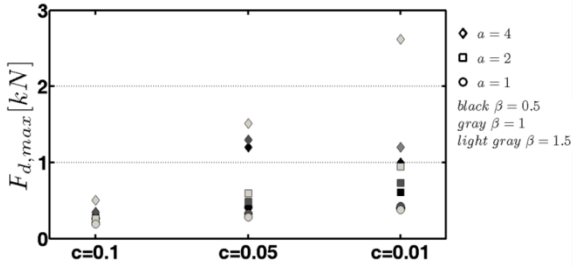

Figure 6.14: Reaction force in drained condition in correspondence of the highest strain applied for all the cases.

Time dependency results in different behaviors if the material is analyzed at the end of the loading phase or at the end of the relaxation phase. Only the higher strain condition is considered (ΔF_{max}), since it is representative of the whole behavior of the tissue, and the difference in terms of reaction force is plotted for all the

distribution analyzed. This information is presented in Figure 6.15.

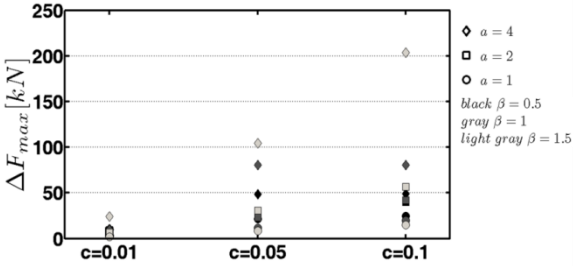

Figure 6.15: Difference between undrained and drained conditions in correspondence of the highest strain applied for all the cases.

6.3.3 Discussion

The sensitivity analysis proposed can help understanding model behavior.
Parameters $\tilde{a}$ and $\tilde{c}$, for a fixed exponent β, define the value of the distribution along $\theta = \frac{\pi}{2}$ and $\theta = 0$, respectively, independently each other. Besides, fixing exponent β and parameter $\tilde{a}$, if $\tilde{c}$ is decreasing, $\rho(\theta = 0)$ decreases and the distribution is narrower; fixing exponent β and parameter $\tilde{c}$, if $\tilde{a}$ is decreasing, $\rho(\theta = \frac{\pi}{2})$ decreases and the distribution is wider. Also the effect of the exponent β is not trivial: fixing parameters $\tilde{a}$ and $\tilde{c}$, if β increases, both $\rho(\theta = 0)$ and $\rho(\theta = \frac{\pi}{2})$ increase to have a wider distribution. Then, if one considers $\beta = \frac{1}{2}$ fixed as in the work of Ateshian (Ateshian, Rajan, Chahine, Canal, & Hung, 2009), it appears to lose a wide range of distributions analyzable.
The effect of GAGs in swelling properties is shown in Figure 6.13. Results are in agreement with literature, especially for the axial swelling around 10%; in both radial and axial directions, swelling appears strongly related to the ratio between fibers content in radial and axial directions. See, for example, the light gray diamond marker in Figure 6.13: it refers to the distribution with higher fibers density parallel to surface. The expected lowest radial swelling results in the largest axial one.
With a comparison purpose, drained properties itself and drained to undrained relation are proposed only at higher strain imposed. In his work, Ficklin (Ficklin, et al., 2007) states that the mechanical properties of articular cartilage are positively correlated with collagen content only at high compressive strain (larger than 40%): hence, only the results obtained at 50% of strain are shown here. With reference to Figures 6.14 and 6.15, even if all the samples considered has a shear modulus almost constant, higher is the content in fibers, higher is the drained modulus; moreover, a larger difference between drained and undrained responses is related to a more anisotropic distribution.
A peculiar aspect of an unconfined compression test on articular cartilage is the

radial contraction during the relaxation phase. This phenomenon has been investigated as in the work of Fortin (Fortin, Buschmann, Bertrand, Foster, & Ophir, 2003) and it has been evidenced in this sensitivity analysis: this consideration is a further good validation for the presented model.

6.4 CONFINED COMPRESSION TESTS AND NANOINDENTATION TESTS

At the end of any swelling relaxation phase, the coefficients of the stiffness tangent matrix can be extracted from the implemented UMAT. Equations (3.28) and (3.29) can be used to estimate drained indentation modulus and undrained indentation modulus, assuming the solid matrix as a transversely isotropic material: this assumption is reasonable due to the highly anisotropic distributions considered. These two moduli are plotted in Figure 6.16, for all the distributions.

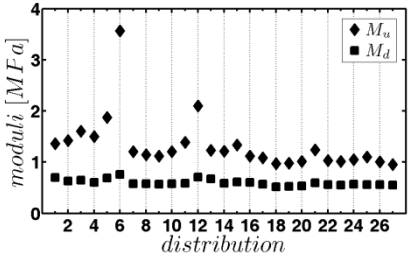

Figure 6.16: Drained indentation modulus (■) and undrained indentation modulus (◦) computed for all the distribution analysed, using the stiffness tensor at the end of swelling relaxation phase and assuming a transversely isotropic material.

Three selected fibers distributions $[II - XV - XXII]$, representative of three markedly different conditions, are chosen. Simulation of a multiload nanoindentation creep test is set in order to reproduce five load levels $[0.1 - 0.5\ mN]$, using a $400\ \mu m$ spherical tip R_{400} and implementing the same protocol used for the equivalent experimental tests explained in Section 4.2: load step of $0.1\ mN$, loading rate of $1\frac{mN}{s}$ and hold time of $120\ s$. The pairs $(F_L - h_d)$ and $(F_L - h_u)$ can be also extracted numerically, one for each load level; then, Equations (4.7) and (4.8) are used to compute numerical drained and undrained moduli. Figure 6.17 shows the comparison, in term of drained modulus M_d (Figure 6.17(a)) and undrained modulus M_u (Figure 6.17(b)), between the values estimated theoretically (from information on stiffness tensor, as in Figure 6.16) and the values computed as best fitting (from numerical load - displacement pairs). Numbers identify the distribution; *i* indicates multiload nanoindentation creep test whereas *c* unconfined compression stress relaxation test.

A good agreement can be found between the predicted drained indentation modulus

from the stiffness matrix and the computed one from multiload nanoindentation test: since the stiffness matrix can be extracted with a very simple simulation (in terms of time consumption), this approach appears interesting from the point of view of a parameter identification process for nanoindentation tests. In case of the undrained one, instead, the prediction fails: it is worth to be noted that the implemented constitutive relation accounts also for viscous aspects that are not considered in the analytical Equations (3.28) and (3.29), based on a purely poroelastic material. It seems, than, that viscoelasticity plays a role in the instantaneous response of AC, at least in the configurations studied.

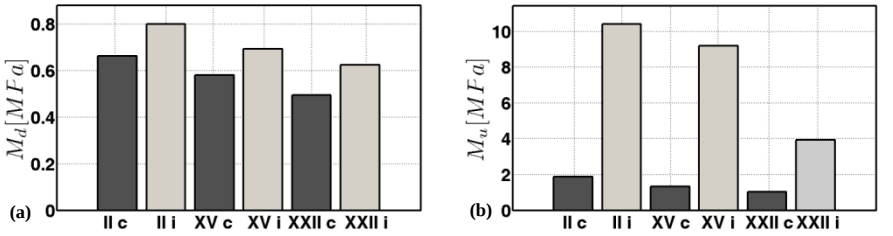

Figure 6.17: Comparison between stress relaxation unconfined compression and multiload creep indentation in terms of (a) drained properties and (b) drained to undrained properties for the three selected fibers distribution.

Experimental data on multiload nanoindentation creep tests have been shown in Chapter 4, Section 4.2. In Figure 6.18 the experimental results are shown again in terms of drained and undrained curves (Figure 6.18(a)) and creep curves (Figure 6.18(b)), considering only five levels of load (to be consistent to the chosen settings for the simulated tests); regarding the creep curves, only the mean value is shown since the variability is highlighted on the drained and undrained curves.

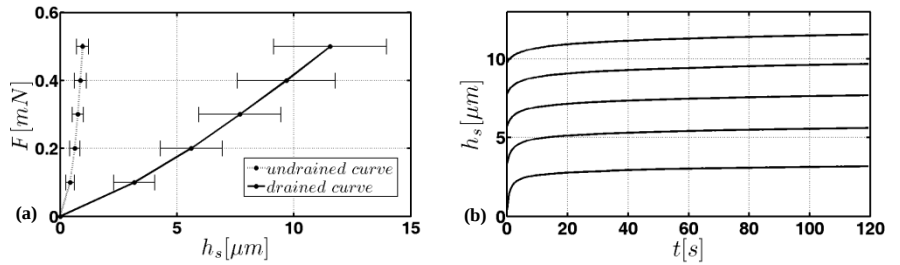

Figure 6.18: (a) Experimental drained and undrained curves obtained with R_{400} tip and (b) creep curves obtained with R_{400} tip, both based on five levels of load.

In Figure 6.19, the experimental data shown above are compared with results obtained by simulating the test using the three fibers distributions mentioned and maintaining the constitutive parameters used for the sensitivity analysis.

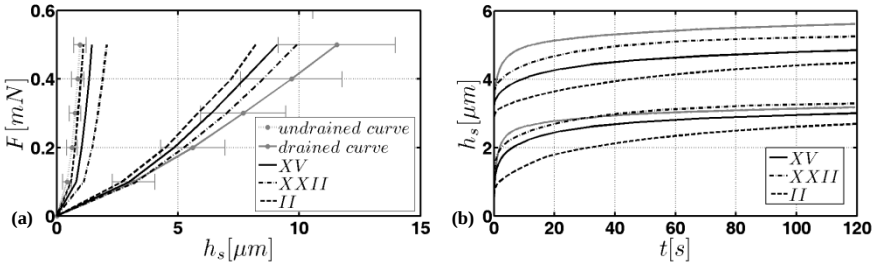

Figure 6.19: (a) Drained and undrained curves and (b) creep curves (zoom at low loads) obtained from simulation using three selected distribution with R_{400} tip and investigating five levels of load.

Curves in Figure 6.19 show that a proper parameter identification for the experimental data is still not achieved: thus, to find a suitable set of parameters defines a further development of this thesis. The configurations studied seem not to replicate the experiments: then, this analysis can be considered as a preparatory step. Therefore, small adjustments are required also on the constitutive parameters chosen: in the following Figures, hints for possible solutions are investigated.

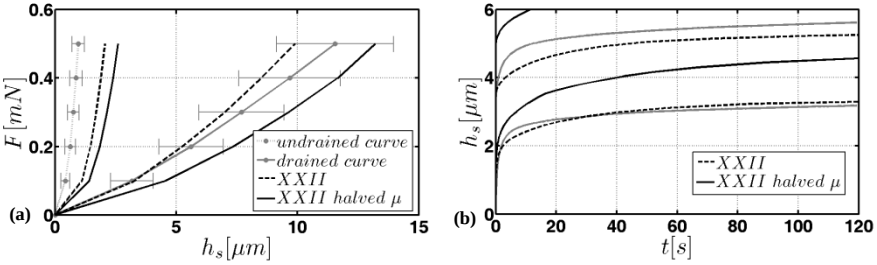

Figure 6.20: (a) Drained and undrained curves and (b) creep curves (zoom at low load) obtained from simulation using distribution *XXII* and halving the matrix shear modulus. Unmodified case *XXII* is reported as comparison.

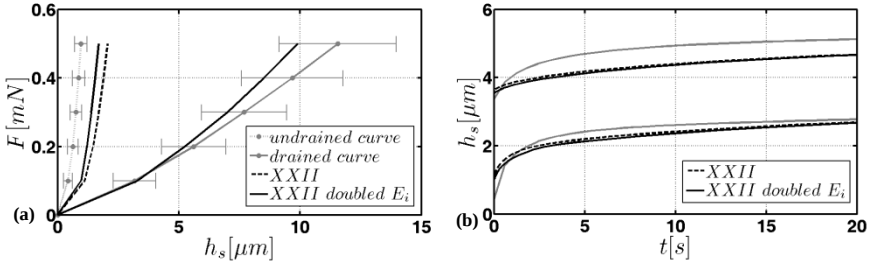

Figure 6.21: (a) Drained and undrained curves and (b) creep curves (zoom at the low loads and low time) obtained from simulation using distribution *XXII* and doubling the instantaneous response of SLS model. Unmodified case *XXII* is reported as comparison.

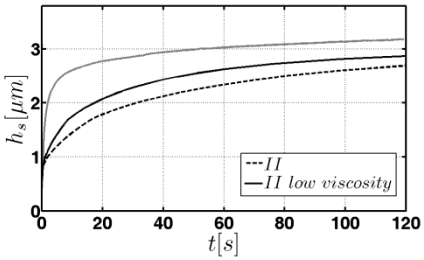

Figure 6.22: Creep curve obtained at $F = 0.1\ mN$ from simulation using distribution II and halving the characteristic relaxation time of SLS model. Unmodified case II is reported as comparison.

In Figure 6.20 the effects of an halved matrix shear modulus μ is shown using distribution $XXII$ as reference. The same distribution is used in the analysis of the effect of stiffer (doubled) instantaneous response for COL fibrils (maintaining the same long term response and the same characteristic relaxation time) presented in Figure 6.21. Besides, the effect of an halved characteristic relaxation time is inquired on distribution II and highlighted in Figure 6.22.

The above results can be summarized as follow. Fixing a fibers distribution and decreasing the matrix shear modulus, the material is softer in both drained and undrained conditions and the difference between these two limits increases, the drained to undrained ratio decreases (Figure 6.20): the weight of the anisotropic part of the tissue becomes more relevant than the isotropic one. Increasing in instantaneous response of collagen fibers, maintaining constant the drained properties of the fibrils, results in a stiffer undrained condition (Figure 6.21). Halving the viscosity, the characteristic relaxation time decreases and the drained condition is achieved faster (Figure 6.22).

REFERENCES

Ateshian, G., Rajan, V., Chahine, N., Canal, C., & Hung, C. (2009). Modeling the matrix of articular cartilage using a continuous fiber angular distribution predicts many observed phenomena. *Journal of Biomechanical Engineering, 131*, 061003-1:10.

Broom, N., & Flachsmann, R. (2003). Physical indicators of cartilage healrh: the relevance of compliance, thickness, swelling and fibrillar texture. *Journal of Anatomy, 202*, 481-494.

Buckley, M., Glghorn, J., Bonasser, L., & Cohen, I. (2008). Mapping the depth dependence of shear properties in articular cartilage. *Journal of Biomechanics, 41*, 2430-2437.

Buckwalter, J., Mankin, H., & Grodzinsky, A. (2005). Articular cartilage and osteoarthritis. *AAOS Instructional Course Lectures, 54*, 465-480.

Buschmann, M., & Grodzinsky, A. (1995). A molecular model of proteoglycan-associated electrostatic forces in cartilage mechanics. *Journal of Biomechanical Engineering, 117*, 179-192.

Chahine, N., Chen, F., Hung, C., & Ateshian, G. (2005). Direct measurement of osmotic pressure of glycosaminoglycan solutions by membrane osmometry at room temperature. *Biophysical Journal, 89*(3), 1543-1550.

Elmore, S., Skoloff, L., Norris, G., & Carmeci, P. (1963). Nature of "imperfect" elasticity of articular cartialge. *Journal of Applied Physiology, 18*(2), 393-396.

Ficklin, T., Thomas, G., Barthel, J., Thonar, E., Masuda, K., Asanbaeva, A., . . . Klish, S. (2007). Articular cartilage mechanical and biochemical property relations before and after in vitro growth. *Journal of Biomechanics*, 3607-3614.

Fortin, M., Buschmann, M., Bertrand, M., Foster, F., & Ophir, J. (2003). Dynamic measurement of internal solid displacement in arrticular cartilage using ustrasound backscatter. *Journal of Biomechanics, 36*(3), 443-447.

Han, E., Chen, S., Klisch, S., & Sah, R. (2011). Contribution of proteoglycan osmotic swelling pressure to the compressive properties of articular cartilage. *Biophysical Journal, 101*(4), 916-924.

Han, L., Frank, E., Greene, J., Lee, H., Hung, H., Grodzinsky, A., & Ortiz, C. (2011). Time-Dependent Nanomechanics of Cartilage. *Biophysical Journal, 100*, 1846-1854.

Hu, Y., Zhao, X., Vlassak, J., & Suo, Z. (2010). Using indentation to characterize the poroelasticity of gels. *Applied Physics and Letters, 96*, 121904-1:3.

Huang, C., Mow, V., & Ateshian, G. (2001). The role of flow independent viscoelasticity in the biphasic tensile and compressive responses of articula cartilage. *Journal of Biomechanical Engineering, 123*(5), 410-418.

Lilledahl, M., Pierce, D., Ricken, T., Holzapfel, G., & de Lange Davies, C. (2011). Structural analysis of articular cartilage using multiphoton microscopy: input for biomechanical modeling. *IEEE Transactions on Medical Imaging, 30*(9), 1635-1648.

Lu, X., & Mow, V. (2008). Biomechanics of articular cartilage and determination of material properties. *Medicine and Science in Sports and Exercises, 40*(2), 193-199.

Pierce, D., Trobin, W., Raya, J., Trattnig, S., Bischof, H., Glaser, C., & Holzapfel, G. (2010). DT-MRI based computation of collagen fiber deformation in human articular cartilage: a feasibility study. *Annals of Biomedical Engineering*, 2447-2463.

Shirazi, R., Vena, P., Sah, R., & Klisch, S. (2011). Modeling the collagen fibril network of biological tissues as a nonlinear elastic material using a continuous volume fraction distribution function. *Mathematics and Mechanics of Solids, 16*, 706-715.

van der Voet, A. (1997). A comparison of finite element codes for the solution of biphasic poroelastic problems. *Proceedings of the Institution of Mechanical Engineers H, 211*(2), 209-211.

Wang, Q., Zheng, Y., Leung, G., Lam, W., Guo, X., Lu, H., . . . Mak, A. (2008). Altered osmotic swelling brhavior of proteoglycan-depleted bovine articular cartilage using high frequency ultrasound. *Physics in Medicine and Biology, 53*, 2537-2552.

Wang, Q., Zheng, Y., Niu, H., & Mak, A. (2007). Extraction of mechanical properties of articular cartiilage from osmotic swelling behavior monitored using high freqeuncy ultrasound. *Journal of Biomechanical Engineering, 129*(3), 413-422.

Wilson, W. (2005). *An explanation for the onset of mechanically induced cartilage damage*. Eindhove, Technische Universiteit Eindhoven.

Wilson, W., van Donkelaar, C., van Rietbergen, B., & Huiskes, R. (2005). A fibril reinforced poroviscoelastic swelling model for articular cartilage. *Journal of Biomechanics, 1195-1204*, 38.

Wilson, W., van Donkelaar, C., van Rietbergen, B., Ito, K., & Huiskes, R. (2004). Stresses in the local collagen network of articular cartilage: a poroviscoelastic fibril reinforced finite element study. *Journal of Biomechanics, 37*, 357-366.

CHAPTER 7.
DISCUSSIONS AND CONCLUSIONS

Chapter 7 is dedicated to discuss results providing connections among the single aspects analyzed separately in the previous Chapters.
Section 7.1 shows a comparison between experimental data collected in frequency domain and the ones in time domain. The novel constitutive relation is used in Section 7.2, to improve the code that simulate harmonic tests. Section 7.3 compares the aims explained in the Introductory Chapter with the results achieved to highlight the scientific relevance of this work. Section 7.4 shows the guidelines for further developments and improvements.

Considering the three central Chapters (Chapter 4, Chapter 5, Chapter 6), each of them addresses a specific argument; a complete and dedicated discussion is performed separately for everyone; methodologies are highlighted with respect to their positive aspects and their limitations, data are explained providing comparisons with literature, results are critically analyzed. Nevertheless, these presented aspects belong to the unique idea of articular cartilage mechanical characterization: then, further discussions that try to connect the different areas is required. Experimental tests in frequency domain and time domain are here compared each other; the poroviscoelastic with fibers distribution constitutive relation is used for suggesting possible explanation of experimental evidences; the model for DMA test is improved based on a more complete solid skeleton modeling.

7.1 COMPARISONS AT DIFFERENT CHARACTERISTC LENGHTS

In Chapter 4, experiments carried out with an AFM in frequency domain (DMA) and experiments carried out with a NI in time domain (creep) are shown. Two main differences characterize the two sets of experiments: the nature of the solicitation, harmonic displacement controlled test versus constant load, and the characteristic length investigated, up to few microns versus up to hundreds of microns. In both cases, the AC samples are extracted from the posterior joints of adult bovine exemplaries, but two different animals are considered: hence, a certain amount of intraspecific variability has to be taken into account in analyzing the results.

In Figure 7.1 drained moduli M_d computed in the case of multiload nanoindentation spherical creep tests (samples C_{R_{400},ν_1} and C_{R_{25},ν_1}) and spherical dynamic tests (samples R_{7500} and R_{665}) are shown together. These values are plotted in function of the characteristic length l_c (Figure 7.1(a)) and the equivalent deformation ε_{eq} (Figure 7.1(b)), without forgetting that each tip investigates also different indentation depths (Figure 7.1(c)). As presented in Section 4.2, multiload tests allow to easily investigate multiple characteristic lengths that properly refer to a unique value of M_d: markers indicate the computed mean value whereas the lengths investigated are highlighted by dashed lines; in the case of dynamic tests, instead, a value of M_d is presented for any length investigated.

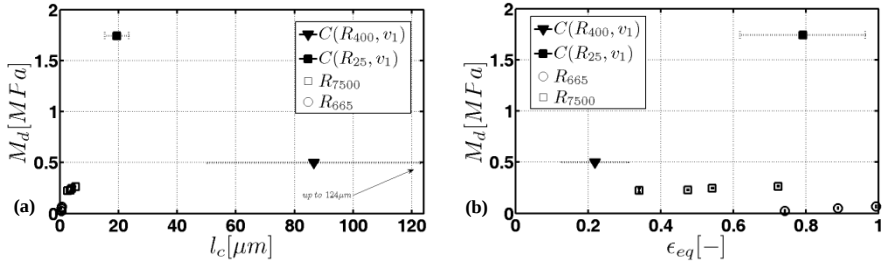

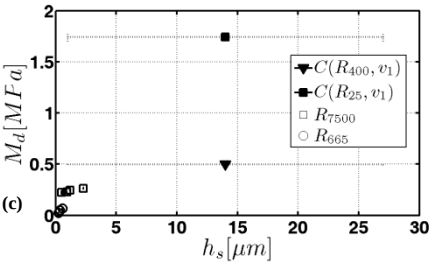

Figure 7.1: Comparison between time domain (creep) tests and frequency domain (DMA) tests analysed in this work in terms of (a) characteristic length, (b) equivalent deformation and (c) indentation depth.

Within the same typology of experiment, two different trends are present: in creep tests, larger tip results in lower modulus; in DMA, the viceversa occurs. In terms of drained modulus, three bandwidth are noticeable, related to tens of kPa, hundreds of kPa and around 1 MPa; at the same time, looking at Figure 7.1(c) the tests can be classified according to three ranges of depth investigated: hundreds of nanometers, few micrometers and tens of micrometers. Accounting for the size effect at larger lengths (explained in Section 4.2), three different zones have been investigated in the present work and the tissue results stiffer at larger ones. The same conclusion can be obtained if the characteristic contact length is considered: larger is this parameter, stiffer is the tissue. Therefore, the tissue shows not only its characteristic depth dependence but also the amount of volume recruited plays a major role in the measured elastic properties, suggesting that the interactions among the single structures (measured at micrometers) magnify their specific properties (that have been investigated at nanometers with the smaller tips). Moreover, from the works of Simha (Simha, Jin, Hall, Chiravarambath, & Lewis, 2007) and Korhonen (Korhonen, et al., 2002), an upper bound for the size effect peculiar of articular cartilage in indentation tests is proposed: if the tip is larger than few millimeters no difference in terms of drained modulus is found. In this work, this effect disappear if the superficial layer is investigated with spherical tip of radii 7.5 μm and 0.665 μm: than, a lower bound for this phenomenon can be suggested.

From both the tests typologies, a characteristic time of the experiment can be extracted and it is related to the predominant phenomenon investigated. In Section 4.1, suggestions about the position of the peak frequency are presented and a transition from poroelasticity to viscoelasticity is evidenced when the behavior is investigated moving from a larger to a smaller tip: the behavior investigated with the conical tip and the smaller spherical tip has been already explained. Then, the following comparison takes into account only the larger spherical tip used in harmonic tests, since poroelasticity is the predominant phenomenon.

Dynamic tests allow a fast estimation of the characteristic time since the position of the peak is easily identified as in Figure 4.2; on the contrary, an estimation of characteristic time in a creep test can be conducted applying a best fitting procedure

using a series of exponential functions or computing the numerical time derivative as shown in Figure 4.18. Dynamic tests conducted with the larger tip result in a characteristic frequency that decreases with the indentation depth from (mean values) $23.3\,Hz$ to $2.9\,Hz$ that corresponds to characteristic times increasing from $0.04\,s$ to $0.34\,s$; smaller tip in creep tests results in less than $5\,s$ wheras the larger tip in less than $1\,s$. These last estimation are based on the fact that the steady state condition is reached in $5-8\,s$ in the case of R_{25} and around $1\,s$ for R_{400}. Imaging to relate these values to the equivalent deformation, the following situation occurs. At equivalent deformation $\varepsilon_{eq}\sim 0.2$, the characteristic time is lower than $1\,s$; in between 0.3 and 0.7, time increases with ε_{eq} up to $0.34\,s$; around 0.7, it is greater than seconds. The larger time that the tissue requires to reach the equilibrium condition when higher deformations are applied is consistent with the concept of depth dependent permeability; independently by the lengths scales analyzed, this relation appears always verified.
Dynamic tests allow also the quantification of the dissipative effects through the magnitude of the peak in the tangent of phase shift graph: Figure 4.2(a) describes a peak decreasing from 0.38 to 0.30 moving from an indentation depth of $0.5\,\mu m$ to $2.3\,\mu m$. The peak of numerical derivative in Figure 4.18, instead, is higher in case of smaller tip than in case of larger one. Decreasing in the characteristic length (smaller indentation depth or smaller tip radius) increases the dissipative effect: if the characteristic size is large, in fact, the role of dishomogeneities (porosity, in this case) is averaged with the elastic properties of the solid matrix.
A separated analysis has to be conducted with the smaller spherical tip and the conical tip on DMA test. They both investigated indentation depth up to a max of $500\,nm$, but with different characteristic lengths (up to $700\,nm$ for the spherical and $200\,nm$ for the conical) and equivalent deformations. An high frequency viscoelastic behavior is found with the conical tip whereas the spherical tip has, probably, given the possibility to investigate a transitional zone.

7.2 POROVISCOELASTIC FIBERS REINFORCED MODEL AS STARTING CONFIGURATION FOR A DMA TEST

The poroviscoelastic with continuous fibers distribution constitutive relationship allows an improvement for the proposed numerical model (Chapter 5) that simulates DMA tests directly in frequency domain.
This model has shown its capability in terms of reducing the time consumption in the numerical simulation of this kind of tests; moreover, together with the intrinsic possibility of this methodology in investigating a wider range of parameters with respect to time domain tests, the proposed sensitivity analysis as well as the parameters identification have given interesting results in interpreting AC mechanical behavior. Its most important limitations are focused in three aspects, basically: the linearized framework; the solid matrix modelling; the homogeneous

and isotropic permeability. For the latter point, improvements and developments can define future objectives arising from this work of thesis; on the contrary, the constitutive relation proposed in Chapter 6 can help regarding the first two ones.
In the presented DMA model, the solid part of AC sample is modelled as a transversely isotropic material: in the numerical discretization, the material properties of the single elements do not change in dependence of its position, under the tip or far from the solicitation area. The model implemented is linearized: hence it can investigate the behavior of the tissue only around the deformed condition reached at the end of the initial step of the procedure.
The purely elastic version of the implemented constitutive relation can be used to simulate this first phase: a quasi - static indentation is performed and a more realistic deformed configuration is achieved. Moreover, the effect of the complex strain field resulting from the indentation test is caught exporting the specific stiffness matrix of each element of the mesh and introducing it into the DMA numerical model. This model still works in a linearized framework but investigates a condition (displacement field and material properties) obtained from a model that accounts for the non - linearities of the tissue.
The parameters obtained by best fitting procedure on the DMA model proposed in Chapter 5 have been already discussed and a marked difference is found between the R_{7500}, h_{2300} case and the other configurations considered. Then, the following two sets of parameters are identified using the improved procedure described above (Table 7.1).

Table 7.1: Geometrical and constitutive (elastic only) parameters used.

MODEL	$\widehat{\alpha_1}[MPa]$	$\alpha_2\,[-]$	$\mu[MPa]$	$\tilde{\alpha}[-]$	$\tilde{c}[-]$	$\beta[-]$
A_{DIN}	0.03	3.22	0.1	3.5	0.01	2
B_{DIN}	0.04	3.32	0.07	3.7	0.007	2.1

Figure 7.2 shows that model A_{DIN} reproduces configuration R_{7500}, h_{2300} in terms of storage modulus and tangent of phase shift, but it is unsuitable to reproduce configuration R_{7500}, h_{500} in terms of $E'^{*}(f)$.
Regarding the second set, instead, parameters are identified using configuration R_{7500}, h_{500}; its application to configurations R_{7500}, h_{920} and R_{7500}, h_{1200} results automatically in an acceptable good prediction for both $E'^{*}(f)$ and $\tan(\phi_f)$, as shown in Figure 7.3.
In both the cases, permeability is still adjusted manually to match the position of the peak and its contribution remains linear and homogeneous.
Results proposed here can improve the conclusions provided in Section 5.2. Consistently with them, this new identification procedure finds two different sets of parameters to describe the whole experiment: the behaviour measured at the largest mean indentation depth, indeed, is achieved using a denser fibers distribution and a slightly higher matrix shear modulus than in the case of the lower mean indentation

depths investigated, even if the parameters remain close each other.
Two interesting conclusions can be done. Focusing on model B_{DIN}, differences in the measure behaviors are given by different deformation condition of the same tissue structure. Model A_{DIN} can replicate the phase shift trend in all the cases (Figure 7.3(b)), suggesting that the anisotropy ratio λ between the radial and axial stiffness is one of the predominant reasons that regulate the balance between conservative and dissipative effects: in fact, both the models result in a similar $\lambda \sim 0.15$ as identified in Section 5.2.

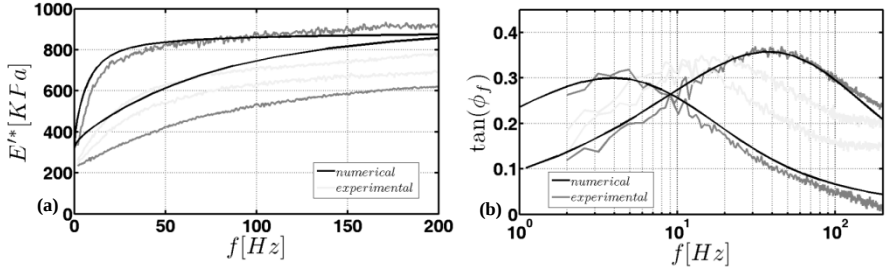

Figure 7.2: (a) Storage reduced modulus and (b) tangent of phase shift. Grey lines defines experimental tests whereas black lines indicate the numerical results using model A_{DIN}.

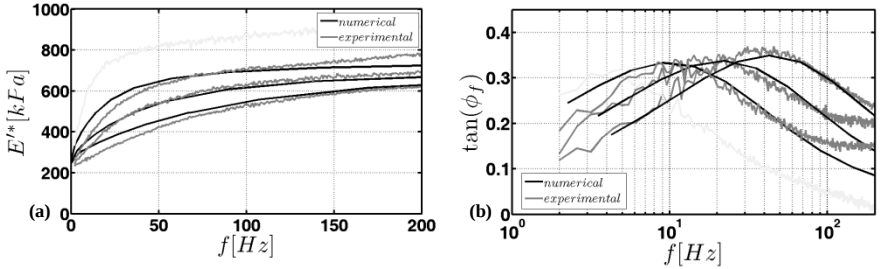

Figure 7.3: (a) Storage reduced modulus and (b) tangent of phase shift. Grey lines defines experimental tests whereas black lines indicate the numerical results for the model B_{DIN}.

7.3 AIMS AND RESULTS

In this work of thesis the mechanical characterization of the superficial layers of AC is performed by making use of experimental techniques in frequency domain (dynamic mechanical tests) and time domain (multiload nanoindentation creep tests). Numerical simulations of the experimental tests can help the explanation of experimental data: then, to achieve this goal, two numerical tools are developed and implemented. An homemade Matlab - based code that simulates DMA tests and a constitutive relationship that accounts for the single constituents (collagen, proteoglycans and matrix) including a continuous distribution for collagen bundles

have been presented. The three main aspects investigated, shown separately in the three central Chapters, belongs to the unique global purpose of a proper mechanical investigation of the tissue at micrometric lengths.
In the Introductory Chapter, the motivations that define the basis over which this thesis is developed and the questions that this thesis want to address are shown.
Chapter 1 to Chapter 3 are dedicated to the description of the background. The tissue under analysis is shown from a structural point of view: its components are presented with a specific focus on their typical length scales as well as the interconnections that occurs among them; the pathologic condition is also briefly presented with particular respect to the role of superficial layers, the importance of which justifies the interest on this mechanical investigation. The results, both experimental and by modeling, already present in literature are shown with the purpose to identify the state of art of the research about articular cartilage biomechanics and the well - established analytical models used to analyze indentation tests.

In Section 4.1, the dynamic mechanical tests conducted at characteristic lengths between hundreds of nanometers to tents of micrometers are presented: even if my role is related to data analysis (the experiments have not been directly conducted by myself), the strong interactions between my group in Politecnico di Milano and the group in University of Genova results in a continuous feedback loop: the data analysis allows to understand intermediate results in order to refine the setup parameters and to achieve the goal of the proper investigation of the tissue. *DMA tests have confirmed its advantages in probing mechanical properties of a material, even in the case of soft hydrated tissues.*

- This kind of test allows to sweep a wide range of frequency without changing the setup, permitting a fast and complete investigation from drained to undrained conditions; moreover, the procedure is almost insensitive and quite robust to tip change (i.e. the characteristic length analyzable).
- The poroviscoelastic behavior of articular cartilage is investigated by introducing the concepts of characteristic lengths and equivalent deformations: depending of these measures, the tissue shows a dominant poroelastic response at micrometer lengths that turns toward a dominant viscoelastic response at hundreds on nanometer sizes. Around $1-2\ \mu m$, a transition occurs in terms of elastic properties and balance between elastic and dissipative forces but not for the overall dissipative effects that decrease with depth. The measures are consistent with the tissue structure and, then, this study appears a quantitative justification of tissue behavior.
- The characteristic time of the phenomenon investigated is used discriminate poroelastic behavior from viscoelastic behavior, based on the spatial dependence typical of the former one.

Section 4.2 proposes a novel method that couples nanoindentation tests and creep tests. *Nanoindentation multiload creep test has shown to be a suitable technique in investigating local poroelastic properties at micrometric characteristic lengths.*

- At micrometric characteristic lengths, the superficial layers of articular cartilage show a predominant poroelastic behavior.
- The methodology proposed confirms a trend already shown in literature: larger is the tip, higher is the measured drained indentation modulus. In this study, by making use of the concept of characteristic lengths and equivalent deformation, an explanation is suggested: an higher magnitude of the solicitation (strain imposed) has a major role than a large volume solicited (that depends on contact radius), possibly related to the role of collagen fibrils activation state.
- The analytical function derived by the uniaxial consolidation problem of a poroelastic medium subjected to a confined compression test define a fast tool for the local estimation of permeability. The simplification in considering an uniaxial problem is balanced by the introduction of a corrective factor for the contact radius that takes into account for a more complex fluid path and that seems to be independent by the tip radius. Nevertheless, the strain dependency found for the permeability is consistent with results proposed in literature.

Chapter 5 is dedicated to the description of an homemade numerical code for the simulation of DMA tests. *The proposed numerical code allows to simulate the problem directly in frequency domain, saving computational time. Besides, it is a powerful tool for the identification of material properties from experimental data*.

- The model is implemented in a Matlab environment and simulate the problem under the assumptions of small strains (linearized framework), isotropic and homogenous permeability, incompressibility of solid and fluid parts.
- A wide sensitivity analysis is performed on both geometrical parameters of a DMA spherical nanoindentation and the constitutive parameters of the tissue. By considering an isotropic material, it has been shown that the indenter radius (for constant penetration depth) has a larger effect on the material response that the penetration depth (for constant deformation). By varying the constitutive parameters (anisotropy ratio and out - of - plane Poisson's ratio), the material shows an high variability in the response: the importance of a proper choice of material parameters has been highlighted as well as the capability of nanoindentation test to take into account for all of them, allowing their identification.
- An identification process has been performed using experimental data presented in Section 4.1 (data collected with the larger spherical tip shows a dominant poroelastic behavior) to infer about material properties:

throughout the thickness investigated, the material has a constancy in the anisotropy ratio and out - of - plain Poisson's ratio, maintaining the increasing depth dependency of elastic properties and the decreasing trend with deformation for the permeability.

In Chapter 6 a poroviscoelastic with continuous fiber distribution constitutive relationship, developed in collaboration with Professor Stephen Klisch in his laboratory at California Polytechnic State University, is presented. *In order to achieve a proper modeling of articular cartilage mechanical behavior, porous and viscous aspects have to be considered as well as the structural distribution of collagen fibrils.*

- The relation is implemented in a User MATerial subroutine for the commercial code Abaqus.
- The implemented relation takes into account the mechanical function of the three main components of the tissue, inserting in between the most complete numerical modeling available in literature. Swelling properties are deputed to proteoglycans, whereas viscoelasticity is considered in collagen fibers modeling.
- With reference of harmonic nanoindentation test, it has been proved that a single set of parameters (both constitutive and geometrical) define correctly the structural organization of a tissue thickness of a range $1\ \mu m$ $[0.5 - 1.5\ \mu m]$ in the superficial layers. In fact, the deformed configuration and material properties passed to the homemade code using that set, properly replicate and predict the consequent dynamic tissue behavior.

Nowadays, the pressing toward methodologies to test articular cartilage for the early detection of pathologies or to evaluate engineered tissue is high*: in Section 4.3 the procedure based on multiload nanoindentation creep test is applied on engineered porcine articular cartilage.*

- The methodology has shown its capability in discriminating the different materials (different grades of treatment) highlighting the peculiar properties of them. The results of the blind investigation is that the artificial tissue improves its biomechanical properties, moving from a self-healed sample to the most complete treatment that includes an artificial scaffold together with autologous stem cells.
- The most complete treatment seems to stimulate a proper cartilage growth since its properties are comparable to native one in terms of drained modulus whereas the permeability is just slightly lesser.
- The treatment based on the sole scaffold shows the size effect on drained modulus like the native condition, suggesting that the particular scaffold structure is a good starting point over which the chondrocytes can build the fibers organization.

7.4 FUTURE DEVELOPMENTS

The presented work analyzes the problem of mechanical characterization of the superficial layers of articular cartilage. This problem is investigated from multiple points of view, showing the complexity of reaching a complete understanding of the behavior of this tissue. Looking at the results proposed in this thesis, the major future approach is to improve the proper connections among the single aspects (experiments and simulations) and its extention to clinical applications and to study pathologies. In this sense, this last Chapter suggests some preliminary attempts, the results of which require further validations.

Dynamic tests and creep tests have shown to be consistent as far as the same phenomenon (poroelasticity) is investigated. Starting from the results of this work, interesting comparisons could be extracted if more focused tests are set up. A investigation conducted at the same characteristic lenghts on the same sample by using both time domain and frequency domain tests can conduct to a deeper structural explanations: creep tests allow to an easier study of the long term behavior (low frequencies) whereas DMA tests provied more robust information at higher frequency (with a proper experimental setup). The work of Chin (Chin, Khayat, & Quinn, 2011) shows an example about how to combine creep tests with stress - relaxation tests in extracting mechanical properties from AC sample: a similar approach can be applied also at micrometric length scale to achieve a deepest knowledge on articular cartilage structure.

The work of Miller (Miller & Morgan, 2010) proposes to compare results obtained at miscroscale with the ones obtained at macroscale. A sistematic approach in which the same sample is tested at different characteristic lenghts seems to be a natural consequence of the results shown in this thesis: starting from the lowest scale, possibly investigating the single constituents or a small base network (as show in this work applying DMA using a very small tip), it could be possible to reconstruct the interactions among the structures from which the macroscopic properties derive and are directly responsible for articular cartilage mechanical function.

The application of the methodology based on creep tests on engineered tissues has shown the possibility to discriminate mechanical properties in tissues with different structural arrangements. The step toward the application on the early detection of pathological conditions is the next one: *in vitro* enzimatic digestion is a methods that permits to recreate conditions similar to the different stages of osteoarthits allowing the possibility to have controlled tissues to test before an *in vivo* implant.

Nevertheless, an improved knowledge on a soft hydrated tissue like articular cartilage can give a definitely contribute in the field of material science, toward the design and the production of advanced, bio - inspired hierachical materials.

Numerical methods can have an important role as shown in the work of Wilson (Wilson, Huyghe, & van Donkelaar, 2006). Hence, both the DMA model and the constitutive relationship can be further refined and improved. The work of Ateshian (Ateshian & Weiss, 2010), for example, proposes an anisotropic formulation for the permeability tensor: permeability is a crucial properties in articular cartilage and its

proper modeling becomes a mandatory request. The homemade code that simulate harmonic tests can be improved accounting for a more realistic implementation of permeability but also introducing the compressibility for the solid part or inertial phenomenon. The poroviscoelastic with continuous fibers distribution is still not completely investigated; then, the first step is using its actual version to investigate the tissue, basing on available experimental data: Section 7.2 just define a promising hint that require a deeper analysis. Furthermore, more complex formulations for permeability and viscoelasticity (i.e. quasi - linear viscoelasticity) can be introduced: this work, indeed, has shown the importance that the balance between these two properties has in the biomechanics of this amazing tissue.

REFERENCES

Ateshian, G., & Weiss, J. (2010). Anisotropic hydraulic permeability under finite deformation. *Journal of Biomechanical Engineering, 132*.

Chin, H., Khayat, G., & Quinn, T. (2011). Improved characterization of cartilage mechanical properties using a combination of stress relaxation and creep. *Journal of Biomechanics, 44*(1), 198-201.

Chiravarambath, S., Simha, N., Namani, R., & Lewis, J. (2009). Poroviscoelastic cartilage properties in the mouse from indentation. *Journal of Biomechanical Engineering, 131*, 011004:1-9.

Korhonen, R., Laasanen, M., Toyras, J., Rieppo, J., Hirvonen, J., Helminen, H., & Jurvelin, J. (2002). Comparison of the equilibrium response of articular cartilage in unconfined compression, confined compression and indentation. *Journal of Biomechanics, 35*, 903-909.

Miller, G., & Morgan, E. (2010). Use of microindentation to characterize the mechanical properties of articular cartilage: comparison of biphasic material properties across length scales. *Osteoarthritis and Cartilage, 18*, 1051-1057.

Simha, N., Jin, H., Hall, M., Chiravarambath, S., & Lewis, J. (2007). Effect of indenter size on elastic modulus of cartilage measured by indentation. *Journal of Biomechanical Engineering, 129*, 767-775.

Wilson, W., Huyghe, J., & van Donkelaar, C. (2006). A composition-based cartilage model for the assessment of compositional changes during cartilage damage and adaptation. *Osteoarthirtis and Cartilage, 14*(6), 554-560.

Notes

Notes

Notes

Notes